

# Plot-Based Land-Cover and Soil-Moisture Mapping Using X-/L-Band SAR Data. Case Study Pirna-South, Saxony, Germany

Dissertation zur Erlangung des akademischen Grades  
Doctor rerum naturalium (Dr. rer. nat.)

vorgelegt von  
**M.Sc. Ali Gaber Mohamed Mahmoud**

Gutachter:

Herr Prof. Dr. phil.habil. Manfred F. Buchroithner  
Technische Universität Dresden

Herr Prof. Dr. Richard Gloaguen  
Technische Universität Bergakademie Freiberg

Dresden, 10. Januar 2012



Erklärung des Promovenden

Die Übereinstimmung dieses Exemplars mit dem Original der Dissertation zum Thema:

**„Plot-Based Land-Cover and Soil-Moisture Mapping Using X-/L-Band SAR Data. Case Study Pirna-South, Saxony, Germany“**

wird hiermit bestätigt.

.....  
Ort, Datum

.....  
Unterschrift (Vorname Name)



*To the soul of my Father*  
*To my beloved Mother*  
*To my Wife, and my daughters:*  
*Yomna and Salma*



## Acknowledgements

I sincerely thank my supervisor, Prof Dr. Manfred F. Buchroithner, for his invaluable guidance during the research period. Discussions and comments as well as advices have been very helpful for me. I am thankful to Dr. Nikolas Prechtel for his valuable advices and help in GIS modeling. My sincere gratitude is to Mrs. Sharma for her kind help. My sincere gratitude is extended to the all staff of the institute and my colleagues.

I am thankful to the “Staatsbetrieb Geobasisinformation und Vermessung Sachsen (GeoSN)” and the “Sächsisches Landesamt für Umwelt, Landwirtschaft und Geologie (LfULG)” for supporting and providing valuable part of the data used in this study. My sincere gratitude is to Thomas Hahmann from the Deutsches Luft- und Raumfahrtzentrum (DLR) for his assistant. Also, many thanks go to the “Agrargenossenschaft Niederseidewitz e.G.”, the “Agrargenossenschaft Börnersdorf” and “Gemeinde Dohma” for their valuable help in the field work.

I sincerely thank to the Institute of Hydrology and Meteorology, TU Dresden, for supporting with TDR. Also many thanks go to the Institute of Geography, TU Dresden, and the laboratory staff for their assistance to measure the soil moisture. My sincere gratitude is to the Institute of Photogrammetry and Remote Sensing, Chair of Remote Sensing, TU Dresden, for facilitating the use of ENVI software.

The appreciations are extended to the Egyptian Government for the financial support and I would like to extend my gratitude to all members of the Egyptian Cultural Office in Berlin for their interest and enormous help.

Finally, I acknowledge the strong support and love that I have received from all of my family during the preparation of this dissertation. I'm very grateful to my wife Walaa and my two daughters Yomna and Salma, who gave the incredible love and the endless support during all time.

## Abstract

Agricultural production is becoming increasingly important as the world demand increases. On the other hand, there are several factors threatening that production such as the climate change. Therefore, monitoring and management of different parameters affecting the production are important. The current study is dedicated to two key parameters, namely agricultural land cover and soil-moisture mapping using X- and L-Band Synthetic Aperture Radar (SAR) data.

Land-cover mapping plays an essential role in various applications like irrigation management, yield estimation and subsidy control. A model of multi-direction/multi-distance texture analysis on SAR data and its use for agricultural land cover classification was developed. The model is built and implemented in ESRI ArcGIS software and integrated with "R Environment". Sets of texture measures can be calculated on a plot basis and stored in an attribute table for further classification. The classification module provides various classification approaches such as support vector machine and artificial neural network, in addition to different feature-selection methods. The model has been tested for a typical Mid-European agricultural and horticultural land use pattern south to the town of Pirna (Saxony/Germany), where the high-resolution SAR data, TerraSAR-X and ALOS/PALSAR (HH/HV) imagery, were used for land-cover mapping. The results indicate that an integrated classification using textural information of SAR data has a high potential for land-cover mapping. Moreover, the multi-dimensional SAR data approach improved the overall accuracy.

Soil moisture (SM) is important for various applications such as crop-water management and hydrological modelling. The above-mentioned TerraSAR-X data were utilised for soil-moisture mapping verified by synchronous field measurements. Different speckle-reduction techniques were applied and the most representative filtered image was determined. Then the soil moisture was calculated for the mapped area using the obtained linear regression equations for each corresponding land-cover type. The results proved the efficiency of SAR data in soil-moisture mapping for bare soils and at the early growing stage of field-crops.

# Table of Contents

Acknowledgements .....	i
Abstract .....	ii
Table of Contents .....	iii
List of Figures .....	vii
List of Tables .....	x
Acronyms and Abbreviations .....	xii
Symbol/Parameter Definitions .....	xiii
1 Introduction .....	1
2 Theoretical Basics .....	4
2.1 Radar Remote Sensing .....	4
2.1.1 A Brief History of Radar .....	4
2.1.2 An Account of Radar Imaging .....	4
2.1.3 SAR Image Formation .....	6
2.1.3.1 SAR Geometric Configuration .....	8
2.1.3.2 Geometric Distortions of the Radar Image .....	9
2.1.3.3 Spatial SAR Resolution .....	10
2.1.3.4 Scattering From Earth Surface Features .....	11
2.1.3.5 Polarimetric Radars .....	12
2.1.3.6 Scattering Behaviour .....	13
2.1.4 Radar Image Speckle .....	15
2.1.5 Current Available Satellite SAR Data .....	16
2.1.6 TerraSAR-X .....	16
2.1.7 ALOS/PALSAR .....	17
2.2 Agricultural Applications with Radar .....	19
2.2.1 Microwave Interaction with Agricultural Targets .....	19
2.2.1.1 System Parameters .....	19
2.2.1.2 Target Parameters .....	21
2.2.2 Crop Type Identification .....	22
2.3 Soil Moisture Extraction from SAR Data .....	23
2.3.1 Importance of Microwaves in Soil Moisture Content .....	23
2.3.2 Dielectric Behaviour of Wet Soils .....	23
2.3.3 Soil Moisture Measurements .....	24
2.3.4 Roughness Estimation .....	24
2.3.5 Penetration Depth .....	25
2.3.6 Target Parameters Influencing Microwave Signatures .....	25
2.3.6.1 Effect of Soil Texture and Roughness .....	25
2.3.6.2 Bulk Density Effects .....	26
2.3.6.3 Effect of Vegetation .....	26
2.3.7 Volumetric Soil Moisture Using Backscattering Data .....	27

2.3.8	Time Domain Reflectometry (TDR).....	28
2.3.9	Radiometric Calibration .....	29
2.3.9.1	Sigma Naught $\sigma^0$ .....	29
2.3.9.2	Gamma $\gamma$ .....	29
2.3.9.3	Radar Brightness $\beta^0$ .....	29
3	Study Area and Data Preparation .....	30
3.1	Description of the Study Area .....	30
3.2	Data Sources .....	34
3.2.1	SAR Data.....	34
3.2.1.1	TerraSAR-X Data .....	34
3.2.1.2	ALOS PALSAR.....	34
3.2.2	Digital Ortho-Photos (DOP) .....	37
3.2.3	Digital Terrain Model (DTM) .....	37
3.2.4	Field-Map.....	37
3.3	Instrument and Software.....	37
3.3.1	Instruments .....	37
3.3.2	Software .....	37
3.4	Data Preparation and Processing.....	38
3.4.1	Radiometric Calibration of TerraSAR-X Data .....	38
3.4.2	Radiometric Calibration of ALOS PALSAR Data .....	40
3.4.3	Data Re-Scaling.....	41
3.4.4	Plot Mapping and Sampling .....	41
3.4.5	Speckle Reduction and Signal to Noise Ratio .....	41
4	Plot-Based Multi-Direction /-Distance Texture Analysis Model for Agricultural Land Cover Classification Using SAR Data.....	43
4.1	Introduction .....	43
4.2	Land Cover Classification Using SAR Data .....	43
4.2.1	General Objectives .....	43
4.2.2	Test Area and Imagery .....	44
4.3	Texture Analysis .....	45
4.3.1	Use of Texture .....	45
4.3.2	Systematisation of Textural Features .....	46
4.3.3	Texture and Scale.....	47
4.3.4	Texture in Radar Imagery .....	47
4.3.5	Spatial Reference for Textural Features .....	48
4.4	The Concept of the Model.....	48
4.4.1	Modules .....	48
4.4.2	GIS Integration.....	50
4.5	Selected Model Features in Detail .....	51
4.5.1	Grey-Level Co-Occurrence Matrix (GLCM) .....	51
4.5.2	Features Derived from GLCM.....	51
4.5.3	Calculation of Separability .....	54
4.6	Implementation .....	55

4.7	Results of the Model Application .....	60
4.7.1	Influence of Image Quantization .....	60
4.7.2	Feature Extraction .....	60
4.7.3	Influence of Direction .....	61
4.7.4	Influence of Distance .....	62
4.7.5	Influence of Speckle Filtering .....	65
4.8	Conclusion .....	69
5	Plot-Based Multi-Direction /-Distance Texture Analysis Model for Agricultural Land Cover Classification Using SAR Data .....	70
II	- Classification Module .....	70
5.1	Introduction .....	70
5.2	Feature Extraction and Selection .....	71
5.3	Feature Selection Methods .....	72
5.3.1	Attribute Selection Approach .....	72
5.3.1.1	Entropy-Based Filters .....	72
5.3.1.2	Random Forest Filter .....	73
5.3.1.3	Cut-offs Algorithms .....	73
5.3.2	Principle Component Analysis .....	73
5.4	Use of Multiple Features of Remotely Sensed Data .....	74
5.5	The R Environment .....	74
5.6	Classification Approaches .....	75
5.6.1	Artificial Neural Network .....	76
5.6.2	Support Vector Machine .....	79
5.6.3	Logistic Regression .....	82
5.6.4	Linear Discriminant Analysis .....	82
5.6.5	K-Nearest Neighbour .....	82
5.7	Combination of Multiple Classifiers .....	83
5.8	Selection of a Classification System and Training Samples .....	84
5.9	Classification Accuracy Assessment .....	84
5.10	Classification Model Description .....	85
5.10.1	Implementation .....	85
5.10.2	R Packages Used in the Model .....	89
5.11	Results of the Model Application .....	89
5.11.1	Classification and Feature Selection Methods .....	90
5.11.1.1	Separability Analysis Approach .....	91
5.11.1.2	Attribute Selection Methods .....	92
5.11.1.3	Principle Component Analysis .....	94
5.12	Conclusion .....	96
6	TerraSAR-X and ALOS PALSAR Data Application to Land Cover Classification .....	97
6.1	Introduction .....	97
6.2	Multi-Dimensional SAR Data .....	98
6.2.1	Multi-Frequency .....	98

6.2.2	Multi-Polarisation .....	99
6.2.3	Multi-Temporal.....	99
6.2.4	Multi-Features.....	100
6.3	TerraSAR-X and ALOS/PALSAR for Land Cover Classification .....	100
6.4	Methodology .....	100
6.4.1	Data Used.....	100
6.4.2	Feature Extraction and Classification .....	101
6.5	Results and Discussion.....	102
6.5.1	Comparison between Different Grey Scales.....	102
6.5.2	Comparison between DTM and GIM in Backscattering Calculation..	102
6.5.3	Separability Values .....	102
6.6	Classification Results.....	103
6.6.1	Multi-Date Example .....	103
6.6.2	Multi-Frequency Example .....	103
6.6.3	Multi-Polarisation Example .....	104
6.6.4	Multi-Frequency/Multi-Polarisation Example.....	104
6.7	Conclusions .....	108
7	Soil Moisture Mapping using TerraSAR-X Data .....	109
7.1	Introduction .....	109
7.2	Data Used and Methodology .....	111
7.2.1	Data Used.....	111
7.2.2	Field Work .....	111
7.2.3	Data Processing .....	112
7.2.3.1	Speckle Reduction.....	112
7.2.3.2	Comparison between DTM and GIM for Backscattering Calculation .....	112
7.2.3.3	Extracting the Backscattering Values .....	114
7.3	Results and Discussion.....	114
7.3.1	DTM and GIM for Backscattering Calculation.....	114
7.3.2	Effect of Speckle Reduction on Backscattering .....	114
7.3.3	Soil Moisture Extraction .....	115
7.4	Conclusion .....	119
8	Conclusions and Outlook .....	120
8.1	Conclusions .....	120
8.2	Outlook .....	121
9	References.....	123
10	Appendices .....	140

## List of Figures

Figure 2.1. The concept of using the platform motion to synthesise an effectively long antenna; for simplicity, the footprint of the real antenna on the ground is shown as rectangular (from Richards 2009). .....	6
Figure 2.2. SAR imaging geometry in strip-map mode (from Lee & Pottier 2009)...	8
Figure 2.3. Geometric distortions of radar image (from Wang 2008).....	10
Figure 2.4. Geometry for computing range resolutions (from Richards 2009).....	11
Figure 2.5. Common scattering mechanisms (from Richards 2009).....	12
Figure 2.6. Polarized microwaves (from Tso & Mather 2009).....	13
Figure 2.7. The predicted radar cross sections for a slightly rough surface assuming an exponential correlation function. The left figure shows the effect of changing surface roughness and constant dielectric constant; the right shows the effect of changing dielectric constant for constant roughness (Elachi & Van Zyl 2006). .....	14
Figure 2.8. Speckle formation in radar images (from Lillesand <i>et. al.</i> 2008).....	15
Figure 2.9. Imaging geometry in different acquisition modes (www1). .....	17
Figure 2.10. PALSAR acquisition modes (www2). .....	18
Figure 2.11. Sources of radar backscatter from cultivated crops (from Henderson <i>et al.</i> 1998). .....	20
Figure 2.12. Definition of surface and incident area (from Henderson 1998). .....	29
Figure 3.1. Location of the study area. ....	31
Figure 3.2. a) Hypsometric colouring of the DTM, and b) Slope map of the study area. ....	31
Figure 3.3. Land use map (2005) of the study area (source: GeoSN, Germany). .	32
Figure 3.4. Surface soil texture of the study area (source: www3). .....	33
Figure 3.5. a) TSX image acquired on 31/05/2010 and b) TSX image acquired on 17/06/2010. Redlines: parcel boundaries.....	35
Figure 3.6. a) TSX image of 18/04/2011 (RGB: HV, HH, HV) and b) ALOS PALSAR imagery (RGB: HV, HH, HV) acquired on 31/05/2010. ....	36
Figure 3.7. Status of the ordered PALSAR data.....	36
Figure 3.8. Selected AOIs (red polygons) for SNR and ENL calculations. ....	42
Figure 3.9. General scheme showing the applied approach. For details see Figures 4.2, 5.4, 6.1, 7.2. ....	42
Figure 4.1. (a) TSX image acquired 31 May 2010, (b) TSX image acquired 17 June 2010 and (d) ALOS/PALSAR image (RGB: HV, HH, HV) acquired 31 May 2010. Redlines: parcel boundaries.....	45
Figure 4.2. Methodological flowchart.....	50
Figure 4.3. (a) A 4 x 4 image with four grey levels. (b) General form of GLCM with grey levels 0–3. The value in cell (i, j) stands for the number of times grey levels i and j occur with a specific direction and distance d. (c)–(f) present the results with respect to the four principal directions 0°, 90°, 135°, and 45° degrees, and d = 1 (from Tso & Mather, 2009). ....	52

Figure 4.4. User interface for texture and separability calculation (top: one run, down: batch mode). .....	56
Figure 4.5. User interface showing the statistics and threshold output of one class-pair.....	57
Figure 4.6. User interface for separability output for one run.....	58
Figure 4.7. User interface for the output separability matrices of the batch process. Where the separability values are sorted in a descending order followed by the corresponding combination number in the batch file. ....	58
Figure 4.8. User interface for the final texture calculation step in case of a single run.....	59
Figure 4.9. User interface for the final texture calculation step in case of a batch mode.....	59
Figure 4.10: Effect of direction on separability values for TSX imagery (31/05/2010).....	63
Figure 4.11: Effect of direction on separability values for TSX imagery (17/06/2010).....	63
Figure 4.12: Effect of direction on separability values for ALOS imagery (31/05/2010); a, b) HH polarisation and c, d) HV polarisation. ....	64
Figure 4.13: Effect of distance on separability values for TSX imagery (a, b: 13/05/2010 and c, d: 17/06/2010). ....	64
Figure 4.14: Effect of distance on separability values for ALOS imagery (31/05/2010); a, b) HH polarisation and c, d) HV polarisation.....	65
Figure 4.15. Effect of filter type on separability values for TSX imagery of 31/05/2010. a) homogeneity, and b) angular 2 <sup>nd</sup> moment texture features. 67	
Figure 4.16. Effect of filter's kernel size on separability values for TSX imagery of 31/05/2010. a) homogeneity, and b) angular 2 <sup>nd</sup> moment texture features. ....	68
Figure 5.1. a) A typical three-layer multilayer perceptron neural network, and b) Example of forward propagation procedure on neurone <i>j</i> (Tso & Mather 2009).....	78
Figure 5.2. Hyper-plane <i>b</i> separates the two classes with the maximal margin. ..	80
Figure 5.3. An illustration of KNN. The open circles and the filled circles represent two classes of data while the triangle represents a query data point. The dashed circle indicates the volume centred by the query data point (Yang 2010) .....	83
Figure 5.4. Methodological flowchart.....	86
Figure 5.5. The user interface for data preparation. ....	87
Figure 5.6. The user interface supporting different classification methods. ....	87
Figure 5.7. The user interface to modify the features selected for classification using filtering (attribute selection) methods.....	88
Figure 5.8. The user interface to modify the features selected for classification using principle component analysis technique.....	88
Figure 5.9. The classification accuracy results can be presented as confusion matrix (left) and graphical presentation (right).....	89

Figure 5.10. a) TSX image acquired on 31/05/2010, b) TSX image acquired on 17/06/2010 and c) Mean-TSX image. Redlines: parcel boundaries.....	90
Figure 5.11. Performance of different classification methods using features selected according to their separability values.....	93
Figure 5.12. Performance of feature selection methods for different number of features and the classification accuracy using SVM. ....	94
Figure 5.13. Land cover map based on the classification of TSX imagery acquired on 31/05/2010 and 17/06/2010 using SVM method. ....	95
Figure 6.1. Methodological flowchart.....	101
Figure 6.2. Land cover map of the study area using a) TSX imagery of 31/05/2010 and 17/06/2010, b) TSX and PALSAR HH of 31/05/2010, c) TSX and PALSAR HV of 31/05/2010 and d) PLASAR HH/HV acquired on 31/05/2010.....	106
Figure 6.3. Land cover map of the study area using TSX and PLASAR HH/HV of 31/05/2010.....	107
Figure 7.1. TDR measurements collected during the field work. ....	113
Figure 7.2. Methodological flowchart.....	113
Figure 7.3. The extracted volumetric soil-moisture over the study area; a) on 31/05/2010 for early growing maize and grass, and b) on 17/06/2010 for early growing maize.....	117
Figure 7.4. a) Land-cover map, and b) Extracted volumetric soil-moisture using a subset of the TSX image acquired on 18/04/2011. ....	118
Figure 7.5. Average of volumetric soil-moisture at the plot level on 18/04/2011..	118

## List of Tables

Table 2.1. Pertinent microwave section of the electromagnetic spectrum. ....	7
Table 2.2. Radar wavebands and nomenclature (Mather, 2004).....	7
Table 2.3. Characteristics of Major Space-borne Radar Systems (after Lillesand <i>et. al.</i> 2008).....	16
Table 3.1. Monthly and annual mean air temperature (°C) in Saxony 1961–2000, as well as trends (°C per decade) (from Chmielewski <i>et al.</i> 2005). ....	34
Table 3.2. SAR images specification. ....	35
Table 3.3. Calibration factors for the used TerraSAR-X data.....	39
Table 4.1. Texture Features on the basis of a GLCM (after Haralick <i>et al.</i> 1973). ....	53
Table 4.2. Significant differences in the mean of separability values of image quantisation levels. ....	61
Table 4.3. Signal-To-Noise Ratio and ENL for different filters of TSX 31/05/2010.....	66
Table 5.1. Training and reference data used for land cover classification. ....	90
Table 5.2. Batch-code for image-direction combinations.....	91
Table 5.3. Classification performance using features selected by separability approach.....	92
Table 5.4. Overall classification accuracy statistics. ....	95
Table 6.1. Overall classification accuracy statistics using features of TSX imagery of 13/05/2010, 17/06/2010 and Mean-TSX. ....	104
Table 6.2. Overall classification accuracy statistics using features of TSX imagery of 13/05/2010 and ALOS PALSAR (HH) of 31/05/2010. ....	105
Table 6.3. Overall classification accuracy statistics of using features of TSX imagery of 31/05/2010 and ALOS PALSAR (HH/HV) of 31/05/2010. ....	105
Table 7.1. Measured soil moisture, extracted sigma naught and The $R^2$ values for TSX imagery acquired on 31/05/2010 and 17/06/2010.....	115
Table 7.2. Regression equations for TSX acquired on 31/05/2010 and 17/06/2010.....	115
Table 7.3. Measured soil moisture, extracted sigma naught and The $R^2$ values for TSX imagery acquired on 18/04/2011.....	116
Table 7.4. Regression equations for TSX acquired on 18/04/2011 and the corresponding filtered image.....	117
Table B.1. Separability values of class-pairs indicating the relevant batch-code (Bold figures indicate value > 1.75).....	141
Table B.2. Classification accuracy (%) and Kappa index (%) using the Information Gain method.....	142
Table B.3. Classification accuracy (%) and Kappa index (%) using the gain ratio method.....	142
Table B.4. Classification accuracy (%) and Kappa index (%) using the symmetrical uncertainty method. ....	143
Table B.5. Classification accuracy (%) and Kappa index (%) using the random forest importance methods.....	143
Table B.6. Classification accuracy (%) and Kappa index (%) using the principle component analysis method. ....	144
Table B.7. Selected 10 features using the four selection methods. ....	144
Table C.1. Separability values for TSX backscattering image rescaled to 5 bits using 2 and 3 standard deviations. ....	145

Table C.2. Separability values according to the backscattering calculation method.....	146
Table C.3. Separability values for TSX imagery from 31/05/2010 and 17/06/2010.....	147
Table C.4. Separability values for the PALSAR image from 31/05/2010.....	148
Table D.1. Coefficient of determination $R^2$ values between measured soil moisture and calculated backscatter coefficient using DTM and GIM (31/05/2010) (land cover: maize; used images: filter of sigma-naught). ...	149
Table D.2. SNR and ENL of TerraSAR-X imagery of 31/05/10. ....	150
Table D.3. Coefficient of determination $R^2$ values between measured soil moisture and calculated backscatter coefficient for TSX (17/06/2010) for early growing maize.....	151
Table D.4. SNR and ENL of TerraSAR-X imagery on 17/06/10. ....	152

## Acronyms and Abbreviations

ALOS	Advanced Land Observing Satellite
ALS	Airborne Laser Scanning
ANN	Artificial Neural Network
ANOVA	Analysis of Variance
AOI	Area-of-Interest
ASF	Alaska Satellite Facility
ATKIS	Authoritative Topographic-Cartographic Information System
AVNIR-2	Advanced Visible and Near Infrared Radiometer Type 2
DLR	Deutsches Zentrum für Luft- und Raumfahrt
DOP	Digital Ortho-Photo
DTM	Digital Terrain Model
EEC	Enhanced Ellipsoid Corrected
EM	Electromagnetic Energy
ENL	Equivalent Number of Looks
EOLi	Earth Observation Link
ESA	European Space Agency
ESRI	Environmental Systems Research Institute
FBD	Fine-Beam Double Polarisation
FDA	Fisher discriminant analysis
GeoSN	Staatsbetrieb Geobasisinformation und Vermessung Sachsen
GIM	Geocoded Incidence Angle Mask
GIS	Geographical Information System
GLCM	Grey-Level Co-occurrence Matrix
GPL	General Public License
JAROS	Japan Resources Observation System Organization
JAXA	Japan Exploration Space Agency
JERS-1	Japanese Earth Resources Satellite-1
KNN	K-Nearest Neighbour
LCC	land-cover classification
LDA	Linear discriminant analysis
LfULG	Sächsisches Landesamt für Umwelt, Landwirtschaft und Geologie
LR	Logistic regression
LTV	Landestalsperrenverwaltung des Freistaates Sachsen
LULC	Land use/land cover
MLC	Maximum likelihood classifier
MLP	Multi-Layer Perceptrons
PALSAR	Phased Array L-Band Synthetic Aperture Radar
PCA	Principle Component Analysis
PRISM	Panchromatic Remote-Sensing Instrument for Stereo Mapping
Radar	Radio Detection and Ranging
RLOS	Radar-Line-of-Sight
SAR	Synthetic Aperture Radar
SM	Soil Moisture
SRTM	Shuttle Radar Topography Mission
SVM	Support Vector Machine
TACL	Multi-Direction /-Distance Texture Analysis and Classification
TanDEM-X	TerraSAR-X Add-on for Digital Elevation Measurement
TDR	Time Domain Reflectometry
TSX	TerraSAR-X
UAV	Unmanned Aerial Vehicles
VB.NET	Visual Basic .NET

## Symbol/Parameter Definitions

dB	decibel
DN	digital numbers
$\epsilon'$	Dielectric constant
$f$	frequency
$h$	altitude of the satellite
$K_S$	calibration coefficient
$L$	antenna size
$la$	length of the antenna
$L_c$	attenuation caused by the vegetation canopy
$m_v$	volumetric moisture content
NEBN	Noise Equivalent Beta Naught
NESZ	Noise Equivalent Sigma Zero
$P_d$	penetration depth
$R^2$	coefficient of determination
$r_a$	The azimuth resolution
$r_g$	The ground range resolution
$r_r$	The slant range resolution
$R_s$	surface roughness
$V_{SAR}$	velocity of the SAR imaging system
$X_a$	azimuth resolution of real-aperture radar
$\beta^\circ$	radar brightness
$\theta_i$	incidence angle
$\theta_{loc}$	local incidence angle
$\lambda$	wavelength
$\sigma^\circ$	backscattering coefficient
$\sigma_s$	backscatter from soil
$\sigma_v$	backscatter from vegetation



## 1 Introduction

Agricultural production is becoming increasingly important as the world demand increases. On the other hand, there are several factors threatening that production such as climate change and land degradation. Therefore, monitoring and management of those parameters - or their indicators - related to the production are important. The current study is dedicated to two key parameters, namely agricultural land cover and soil-moisture mapping using X- and L-Band Synthetic Aperture Radar (SAR) data.

Land-cover mapping plays an essential role in various applications like irrigation management, yield estimation and subsidy control. Timely and accurate information on existing land cover is required by decision makers and scientists at all levels. Land cover mapping through traditional field survey is time-consuming and costly. Remote sensing observations are becoming a vital solution for such mapping, especially over large areas. Synthetic aperture radar (SAR) data are almost independent from weather conditions. Nearly every data take of a SAR sensor can theoretically find entrance into monitoring. A time filter can be adapted to the best-possible differentiation of agricultural plants within their phenological cycles. Moreover, multi-temporal monitoring can reveal seasonally changing conditions of annual crops (Waske & Braun 2009; Baghdadi *et al.* 2009; Mróz & Mleczko 2008; Borghys *et al.* 2006). Several SAR sensors providing different configurations have been applied to land cover mapping and proved to be efficient. High-resolution data like the 3-meter resolution TerraSAR-X data even allow a monitoring of highly diversified and fine-grained plot patterns. Land-cover mapping can be studied at various spatial and temporal scales; the current study presents a methodology at a large-scale.

SAR textural information has been shown to be useful for applications such as forest classification (Ulaby, Moore & Fung 1986), crop classification (Treitz *et al.* 1993) and ice mapping (Barber & Ledrew 1991). The current work demonstrates

how an integrated model can strongly facilitate a texture analysis of SAR data using different directions and distances and result in stable classifications of agricultural land cover.

A model of multi-direction/ multi-distance texture analysis on SAR data and its use for agricultural land-cover classification was developed. The model is implemented and available in ESRI ArcGIS software and integrated with “R Environment”. Sets of texture measures, calculated on a plot basis and stored in an attribute table, can be compiled and evaluated by separability values as a pre-condition for successful classification. The classification module provides various classification approaches such as support vector machine and artificial neural network, in addition to different feature-selection methods. A flexible feature-set manipulation interface enables a quick investigation of any feature-source combinations. The model has been tested for a typical Mid-European agricultural and horticultural land use pattern south of the town of Pirna (Saxony/Germany), where the high-resolution SAR data, TerraSAR-X and ALOS/PALSAR (HH/HV) imagery, were used for land-cover mapping. The results indicate that an integrated classification using textural information of SAR data has a high potential for land-cover mapping. Moreover, the multi-dimensional SAR data approach improved the overall accuracy.

Soil moisture (SM) is important for various applications such as crop-water management and hydrological modelling. The above-mentioned SAR data were utilised for soil-moisture mapping and verified by synchronous field measurements. Different speckle-reduction techniques were applied and the most representative filtered image was determined. Then the soil moisture was calculated for the mapped area using the obtained regression equations for each corresponding land-cover type. The results proved the efficiency of SAR data in soil-moisture mapping for bare soils and at the early growing stage of field-crops.

## **Objectives**

The main objectives of the current study are:

- To develop a plot-based texture analysis and classification model supporting the combination of different directions and distances for texture analysis, in addition to various classification methods.
- To investigate the effect of different directions and distances on separation between land-cover types using TerraSAR-X and ALOS PALSAR data, the performance of different classifiers, and the capability of the model for feature selection and multi-feature combinations for further classification.
- To investigate the effect of quantisation level and the speckle filtering parameters on the separation between different land-cover types.
- To investigate the application of TerraSAR-X to soil-moisture mapping and the effect of speckle-filtering parameters on the predicted soil moisture values.

## 2 Theoretical Basics

In addition to the applications of SAR data to vegetation and soil moisture mapping, this section gives an overview of radar remote sensing history, basics, formation and the major available space-borne SAR data.

### 2.1 Radar Remote Sensing

#### 2.1.1 A Brief History of Radar

The word *radar* is an acronym for Radio Detection and Ranging (Lillesand, Kiefer & Chipman 2008). Historically, The distinction of “first electromagnetic echo-location device” is generally awarded to a ship anti-collision system developed by Christian Hülsmeyer in 1904 (Cheney *et al.* 2009). In 1935, Watson-Watt succeeded to locate an aircraft using the BBC radio transmitter near Daventry in the English Midlands. The Americans had the same idea and could detect an aircraft using radar a month before Watson-Watt’s success. Early radars such as those used in the ‘Battle of Britain’ in August/September 1940 operated at long wavelengths (13 m). The British developed the H2S radar, which operated at a 10 cm wavelength and which was fitted to bombers. This targeting radar was the first terrain-scanning radar in the world. Radar research and development proceeded rapidly during World War II for detection of enemy vessels and surfaced submarines, and for gunnery control, also radars were carried by aircraft (Mather 2004). In the late 1970s and early 1980s, space-borne imaging radars, scatterometers and altimeters were developed. Advanced radar implementations, such as polarimetric and interferometric systems, were developed in the 1980s, and were flown in space in the mid to late 1990s (Elachi & Van Zyl 2006).

#### 2.1.2 An Account of Radar Imaging

At the end of the 1940s, the available radar imaging methods were Detection and Ranging, High-Range-Resolution Imaging and Real-Aperture Imaging. The Real-Aperture Imaging system uses an antenna that forms a narrow beam to scan over

the region to be imaged. At each beam location and pulse delay, the system plots the received intensity. The antenna is a physical (real) aperture and the spot on the ground is referred to as the antenna footprint (Cheney *et al.* 2009). The azimuth resolution ( $X_a$ ) of real-aperture radar is given by Equation 2.1:

$$X_a = \frac{\lambda h}{L \cos \theta} \quad (2.1)$$

Where  $\lambda$  is the operating wavelength,  $h$  is the altitude of the satellite,  $L$  is the antenna size, and  $\theta$  is the angle at which the radar wave is incident on the surface. For space-borne radar,  $X_a$  is typically many hundreds of meters to many kilometres, even if  $L$  is large. To illustrate, if  $\lambda = 3$  cm,  $h = 800$  km,  $L = 10$  m, and  $\theta = 20^\circ$ , then  $X_a = 2.5$  km (Richards 2009).

Accordingly, to improve the resolution, the antenna has to be lengthened. Since this cannot be physically done, a simulated solution was developed to achieve this goal. The American Carl Wiley first had the idea in 1951 of using platform movement and signal coherence to reconstruct a large antenna by calculation. As the radar moves between two pulse transmissions (Figure 2.1), it is indeed possible to combine in phases all of the echoes and synthesize a very large antenna array (Maître 2008). This method is called „Synthetic Aperture Radar” (SAR) and more effective to form images (Cheney *et al.* 2009). In this case, the azimuth resolution is given by Equation 2.2:

$$r_a = \frac{l_a}{2} \quad \text{m} \quad (2.2)$$

Where  $l_a$  is the length of the antenna carried on the spacecraft, measured in the along-track direction. It is obvious that the azimuth resolution is independent of slant range, and thus platform altitude, and independent of operating wavelength. Also, ground range resolution is height-independent. Accordingly, a SAR can operate at any altitude with no variations in resolution. Therefore, space-borne operation is feasible (Richards 2009).

SAR systems use an antenna mounted on a satellite or airplane, which is referred to as the platform (Cheney *et al.* 2009). Systems that use the same antenna for both transmitting and receiving electromagnetic (EM) energy are called monostatic, in which the transmitting and receiving locations are the same. When these two locations are different, the radar is called bistatic. Moreover, the multistatic radars involve transmission from one or more locations and reception at one or more locations (Sullivan 2004).

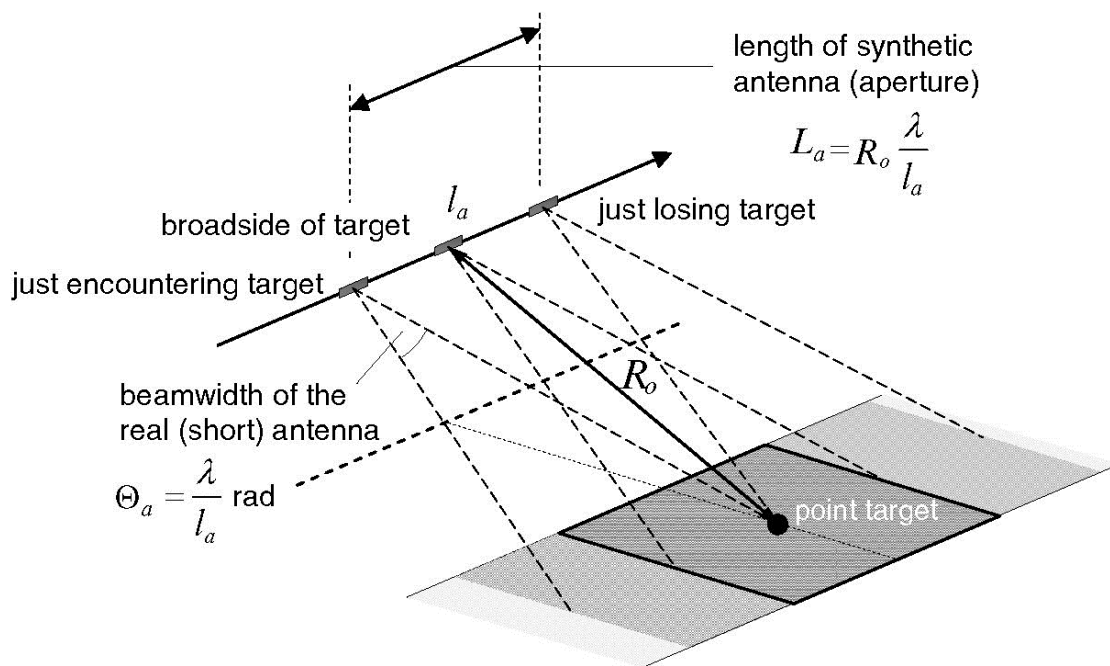


Figure 2.1. The concept of using the platform motion to synthesise an effectively long antenna; for simplicity, the footprint of the real antenna on the ground is shown as rectangular (from Richards 2009).

### 2.1.3 SAR Image Formation

Nowadays, SAR imaging is a well-developed coherent microwave remote sensing technique for providing large-scaled two-dimensional (2-D) high-resolution images of the Earth's surface reflectivity. SAR is an active system (provide their own illumination) operating in the microwave region of the EM spectrum (Table 2.1), usually between P-band and Ka-band (Lee & Pottier 2009). Thus, it is working independently of the solar illumination. These codes (i.e. P-band) came into use during World War II for security purposes. The commonly accepted delimitation of radar wavelengths are shown in Table 2.2 (Mather 2004).

Furthermore, it is capable of penetrating the atmosphere under almost all conditions. Depending on the wave lengths involved, microwave energy can 'see through' haze, light rain, snow, clouds, and smoke (Reddy 2008).

SAR operates in a side-looking geometry which is required in image formation, so that the ground distance of a point from the nadir of the radar can be sorted as a function of its range from the radar (Massonnet & Souyris 2008). Indeed, if the ground is illuminated vertically, there would be always two points located at the same distance, one on each side of the track. As a result, the image would fold onto itself, with points located right and left of the track mixing together (Maître 2008).

Table 2.1. Pertinent microwave section of the electromagnetic spectrum.

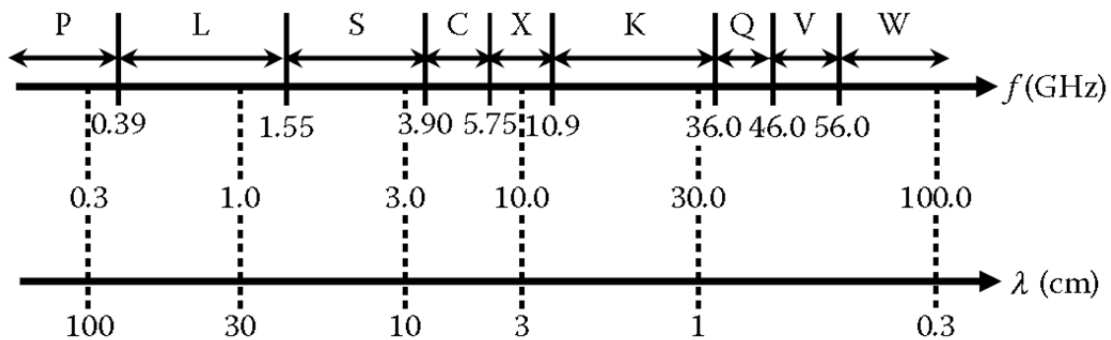


Table 2.2. Radar wavebands and nomenclature (Mather, 2004).

Band designation	Frequency (MHz)	Wavelength (cm)
P	300 - 1000	30 - 100
L	1000 - 2000	15 - 30
S	2000 - 4000	7.5 - 15
C	4000 - 8000	3.75 - 7.5
X	8000 - 12000	2.5 - 3.75
K <sub>u</sub>	12000 - 18000	1.667 - 2.5
K	18000 - 27000	1.111 - 1.667
K <sub>a</sub>	27000 - 40000	0.75 - 1.111

Two types of image properties are important for information extraction. The more important one is where properties of the scene (e.g., its dielectric constant, its geometry, its motion, etc.) produce effects in the image. Thus, measurements or examination of the image can then provide information about the scene. The second one is generated purely by the system and the signal processing (Oliver & Quegan 2004).

### 2.1.3.1 SAR Geometric Configuration

In the case of monostatic radar system, SARs are mounted on a moving platform operating in a side-looking geometry (Figure 2.2). The SAR imaging system is situated at a height  $H$  and moves with a velocity  $V_{\text{SAR}}$ . The antenna aims perpendicular to the flight direction, referred to as “azimuth” ( $y$ ). The antenna beam is then directed slant-wise toward the ground with an incidence angle  $\theta_0$ . The radial axis or radar-line-of-sight (RLOS) is referred to as “slant-range” ( $r$ ). The area covered by the antenna beam in the “ground range” ( $x$ ) and azimuth ( $y$ ) directions is the “antenna footprint”. The platform motion along the flight direction provides the basis for the scanning (Lee & Pottier 2009).

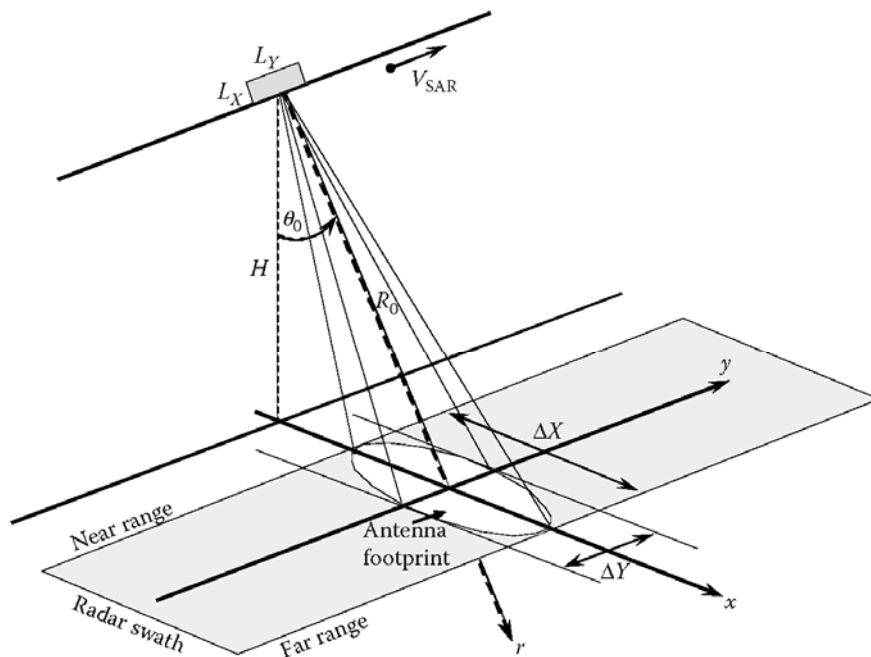


Figure 2.2. SAR imaging geometry in strip-map mode (from Lee & Pottier 2009).

The area scanned by the antenna beam is the “radar swath.” The antenna footprint is defined by the antenna apertures ( $\theta_X$ ,  $\theta_Y$ ) given by Equation 2.3:

$$\theta_X \approx \frac{\lambda}{L_X} \quad \text{and} \quad \theta_Y \approx \frac{\lambda}{L_Y} \quad (2.3)$$

Where  $L_X$  and  $L_Y$  correspond to the physical dimensions of the antenna,  $\lambda$  is the wavelength corresponding to the carrier frequency of the transmitted signal (Lee & Pottier 2009).

### 2.1.3.2 Geometric Distortions of the Radar Image

Since the radar is side-looking, terrain elevation will result in geometric distortions in the SAR image. In fact, even the variation in the projection of the reference surface (ellipsoid) in range direction causes geometric distortions, due to the varying incidence angle (Hanssen 2002). Moreover, the SAR measures the distance to features in the slant range rather than the true horizontal distance along the ground, which results in a varying image scale (Wang 2008). The main geometric distortions of radar image are layover, foreshortening and shadow (Figure 2.3).

Layover occurs when the radar beam reaches the top of a tall feature (point  $b$  in Figure 2.3) before it reaches the base (point  $a$  in Figure 2.3). Consequently, the return signal from the top of the feature will be received before the signal from the bottom will. As a result, the top of the feature is displaced toward the radar from its true position on the ground, and “lays over” the base of the feature ( $b'$  to  $a'$ ) (Wang 2008). This effect can reveal the direction from which the radar is illuminating the target (Massonnet & Souyris 2008).

Foreshortening occurs when the radar beam reaches the base of a tall feature tilted toward the radar (e.g., a mountain) before it reaches the top. As a result, the slope ( $d$  to  $e$ ) will appear compressed and the length of the slope will be represented incorrectly ( $d'$  to  $e'$ ). On the other hand, the shadowing effect occurs when the radar beam cannot reach part of a tall feature ( $h$  to  $i$ ). In the image plane,  $h$  to  $i$  will appear as dark. In addition, any target between  $i$  and  $j$  will also be shown as dark (Wang 2008).

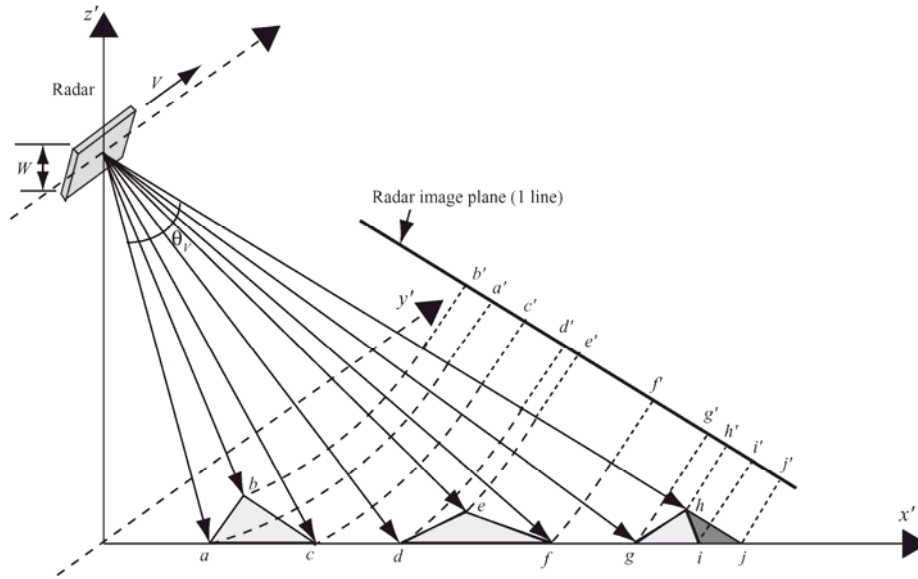


Figure 2.3. Geometric distortions of radar image (from Wang 2008).

### 2.1.3.3 Spatial SAR Resolution

A processed radar image usually is characterised by an azimuth resolution, a ground-range resolution, and the associated number of independent samples (or number of looks) (Ulaby, Moore & Fung 1986). Spatial resolution is one of the most important quality criteria of a SAR imaging system. It describes the ability of the imaging radar to separate two adjacent scatterers. To achieve high resolution in range, very short pulse durations are necessary (Lee & Pottier 2009). The spatial resolution achieved by a SLAR is proportional to the length of the antenna (Mather 2004). If the targets are  $\Delta r$  apart in slant range (as illustrated in Figure 2.4), then the difference in time between their echoes on reception will be  $\Delta t = 2\Delta r c^{-1}$ . Whereas the lower limit on  $\Delta t$  is  $\tau$ , which is the width ( $\tau$ ) of the pulses, the corresponding limit of spatial resolution  $\Delta r$  in the slant range direction is

$$r_r = \frac{c\tau}{2} \quad \text{m} \quad (2.5)$$

which is called slant range resolution.

On the other hand, the spatial resolution in the (ground) range direction is

$$r_g = \frac{c\tau}{2\sin\theta} \quad \text{m} \quad (2.6)$$

This is termed ground range resolution (Richards 2009).

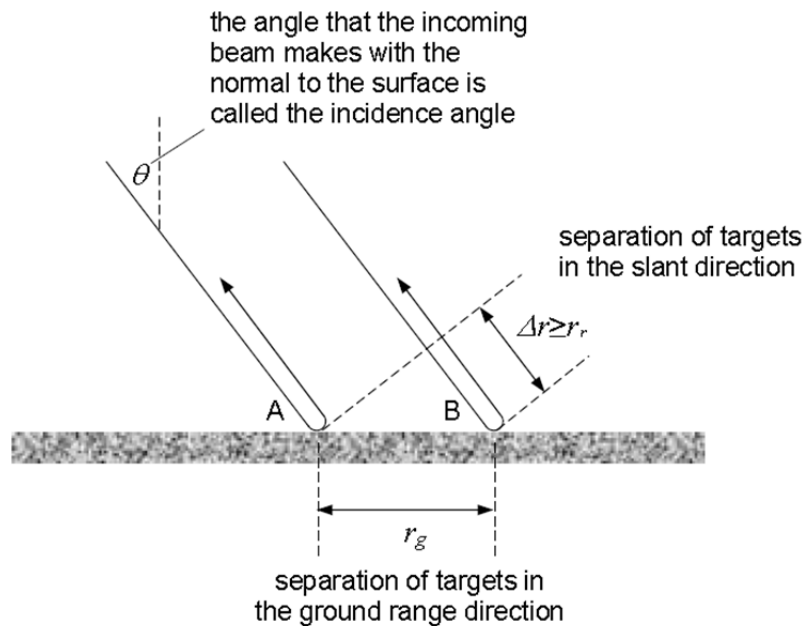


Figure 2.4. Geometry for computing range resolutions (from Richards 2009).

#### 2.1.3.4 Scattering From Earth Surface Features

It is essential to note that radar systems do not directly measure the reflectance of the surface. Instead, they record the intensity of the radiation that is *backscattered* by the surface - that is, the fraction of the incident energy that is directly reflected backwards toward the sensor (Lillesand, Kiefer & Chipman 2008). Moreover, the microwave energy can often penetrate the earth surface materials, so that scattering can occur from within the medium itself as well as from the surface. Understanding the mechanisms by which the energy can scatter to the sensor is necessary to investigate the underlying biophysical characteristics of the medium (Clark & Rilee 2010). Figure 2.5 shows the three most common scattering mechanisms that occur in radar remote sensing of the land surface. The first one is surface scattering in which the energy can be seen to scatter or reflect from a well-defined interface (Richards 2009). If the surface is not smooth on the scale of the wavelength, a portion of the energy will be scattered in all directions (diffuse scatter) (Clark & Rilee 2010). The second one is volume scattering, as the electromagnetic wave interacts with a cloud of scattering particles (Massonnet & Souyris 2008). The third is called strong or hard-target scattering which occurs in a variety of forms. Figure 2.5 illustrates two forms: corner reflector behaviour and facet scattering, both of which give particularly strong responses in radar imagery.

Moreover, If a surface is very dry the incident energy can penetrate, refract and scatter from sub-surface features as depicted (Richards 2009).

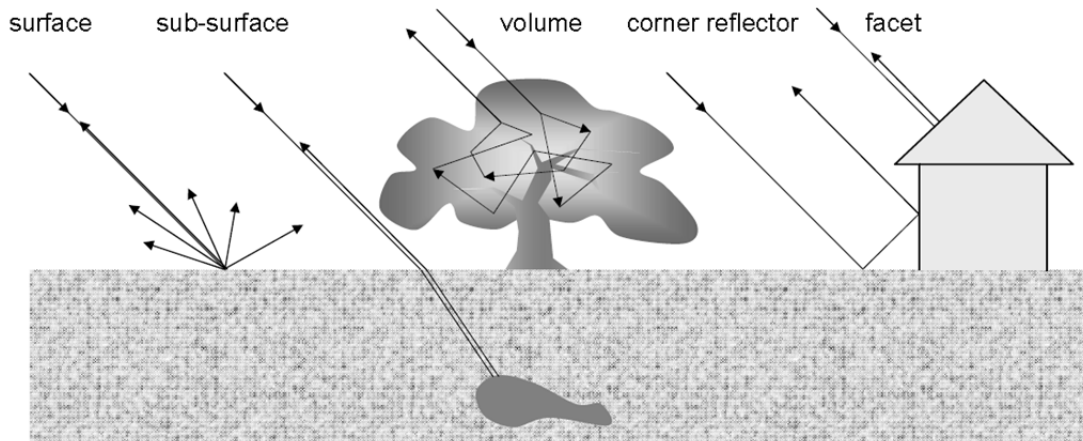


Figure 2.5. Common scattering mechanisms (from Richards 2009).

### 2.1.3.5 Polarimetric Radars

Many radar systems both transmit and receive signals in single polarization. So, they receive only a projection of the electrical-field backscattered by the targets. On the other hand, polarimetric radars measure the orientation of the electrical-field vector and thus capture more information about target characteristics (Lacomme 2001). However, most radar systems restrict the polarized microwaves in such a way that the transmitted and received waves are to a single plane perpendicular to the direction of wave propagation (Figure 2.6). Therefore, the polarized wave is transmitted and received in either the horizontal (H) or the vertical (V) plane. Accordingly, four combinations of transmission and reception for the polarized waves are possible, namely HV, HH, VV, and VH, where HV denotes a wave transmitted in V direction and received in H direction. Radar imagery acquired in terms of HH or VV is called co- or like-polarized imagery, while imagery resulting from HV or VH polarization is called cross-polarized imagery. Cross-polarization perceives multiple-scattering from the target and thus generally results in weaker backscatter than that measured by a co-polarization configuration (Tso & Mather 2009).

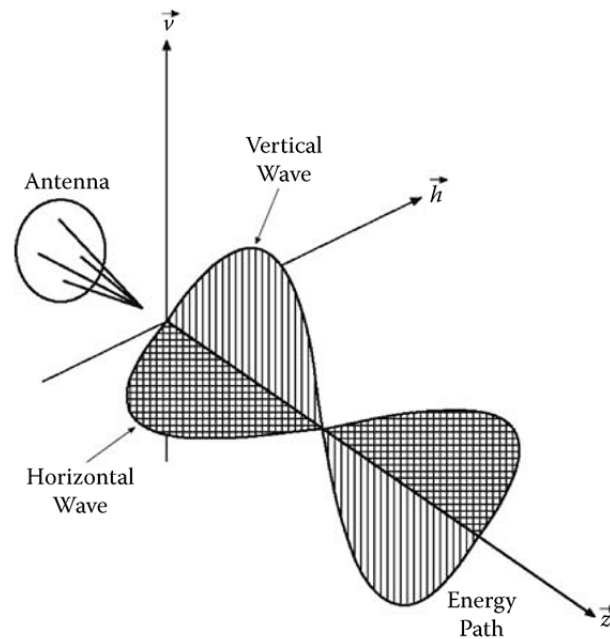


Figure 2.6. Polarized microwaves (from Tso & Mather 2009).

### 2.1.3.6 Scattering Behaviour

#### Role of Incidence Angle

The predicted backscatter cross-section as a function of incidence angle for different surface roughness values and different dielectric constants is shown in Figure 2.7. As shown in the left plot, increasing the surface roughness, generally, causes an increase in the radar cross-sections for all polarisation combinations. As the surface gets rougher, the difference between the HH and VV cross-sections becomes smaller. The plot on the right shows that an increasing dielectric constant (or soil moisture) also increases the radar cross-sections for all polarisations. In this case, however, increasing the dielectric constant also increases the difference between the HH and VV cross-sections (Elachi & Van Zyl 2006).

#### Role of Wavelength

The degree of penetration of the surface material that is achieved by the microwave pulses is dependent on the wavelength. At L-band wavelengths (around 23 cm), microwave radiation can penetrate the foliage of trees and, depending on the height of the tree, may reach the ground. Backscatter occurs

from the leaves, branches, trunks, and the ground surface. In areas of dry alluvial or sandy soils, L-band radar can penetrate the ground for several meters. The same is true for dry glacier ice. Shorter-wavelength C-band radiation can penetrate the canopies of trees, and the upper layers of soil and ice. Even shorter wavelength X-band SAR mainly ‘sees’ the top of the vegetation canopy and the soil and ice surface (Mather 2004). For X-band any surface will be rough, if its variations exceed, about 0.5 cm. Therefore, in reality most natural surfaces will appear rough at X-band. While for L-band a surface will be rough if its vertical variations exceed about 3 cm. Otherwise, It will behave as a specular surface. On the other hand, the sensitivity to the changes in soil moisture is higher at longer radar wavelengths than at shorter wave lengths (Richards 2009).

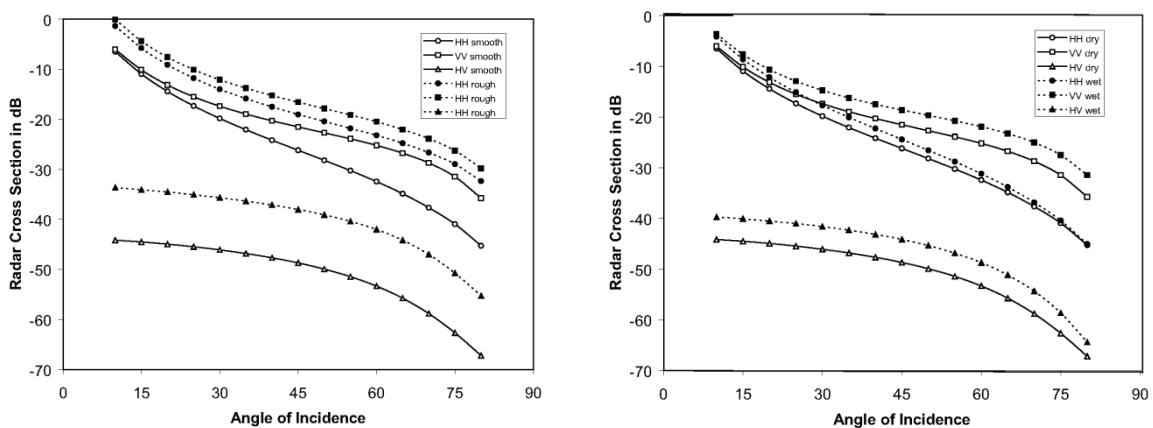


Figure 2.7. The predicted radar cross sections for a slightly rough surface assuming an exponential correlation function. The left figure shows the effect of changing surface roughness and constant dielectric constant; the right shows the effect of changing dielectric constant for constant roughness (Elachi & Van Zyl 2006).

### Role of Polarisation

Permittivity (electrical properties) and other physical properties (inhomogeneities, discontinuities, etc.) of any medium affect the polarization state of an EM wave; therefore, a physical model of a medium is important. For instance, due to the electric properties of the sea surface, horizontally polarized waves are better reflected than vertically polarized ones (Kozlov, Ligthart & Logvin 2004).

### 2.1.4 Radar Image Speckle

Speckle appears as a grainy “salt and pepper” texture in an image (Wang 2008). This is caused by random constructive and destructive interference from the multiple scattering returns that will occur within each pixel (Gomasasca 2009). As shown in Figure 2.8, the waves backscattered from within a single ground resolution cell on the earth’s surface travel slightly different distance from the antenna to the surface and back. This difference in distance means that the returning waves from within a single pixel may be in phase with one another, the intensity of the resulting combined signal will be amplified by constructive interference. At the opposite extreme, destructive interference occurs when waves returning from within a single pixel are at completely opposite phase. Thus, they tend to cancel each other, consequently, reducing the intensity of the combined signal (Lillesand, Kiefer & Chipman 2008). Speckle can be reduced through the application of image processing techniques, such as averaging neighbouring pixel values, or by special filtering and averaging techniques but cannot be completely eliminated (Buchroithner 1993; Lillesand, Kiefer & Chipman 2008).

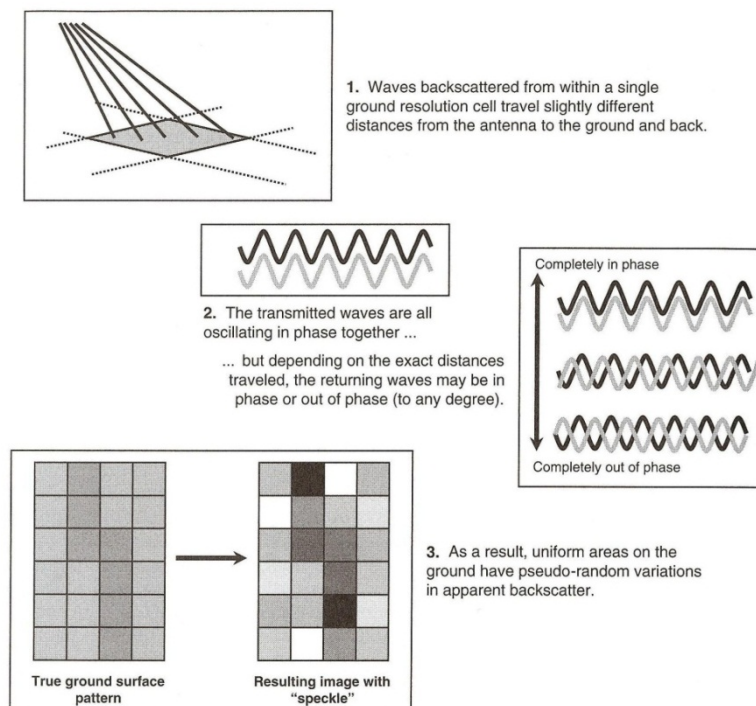


Figure 2.8. Speckle formation in radar images (from Lillesand *et. al.* 2008).

### 2.1.5 Current Available Satellite SAR Data

In the past, currently and in the near future there have been several space-borne SAR instruments available from different space agencies all over the world. The major sensor parameters are summarised in Table 2.3.

Table 2.3. Characteristics of Major Space-borne Radar Systems (after Lillesand *et. al.* 2008).

<b>Characteristics</b>	<b>ERS-2 (ESA)</b>	<b>Radarsat-1 (Canada)</b>	<b>Envisat (ESA)</b>	<b>ALOS (Japan)</b>
Launch date	21April 1995	28November 1995	1March 2002	24January 2006
Altitude, km	785	798	785	692
Wavelength band	C band	C band	C band	L band
Polarisation modes	Single	Single	Single, dual	Single, dual, quad
Polarisation(s)	VV	HH	HH, VV, HV, VH	HH, VV, HV, VH
Look angle	23°	10-60°	14-45°	10-51°
Swath width, km	100	45-500	58-405	20-350
Resolution, m	30	8-100	30-1000	10-100

<b>Characteristics</b>	<b>Radarsat-2 (Canada)</b>	<b>TerraSAR-X (Germany)</b>	<b>COSMO-SkvMed-1 (Italy)</b>
Launch date	2007	2007	2007
Altitude, km	798	514	620
Wavelength band	C band	X band	X band
Polarisation modes	Single, dual, quad	Single, dual, quad	Single, dual, quad
Polarisation(s)	HH, VV, HV, VH	HH, VV, HV, VH	HH, VV, HV, VH
Look angle	10-60°	15-60°	20-60°
Swath width, km	20-500	10-100	10-200
Resolution, m	3-100	1-16	1-100

### 2.1.6 TerraSAR-X

The TerraSAR-X Mission has been realized in a public–private partnership (PPP) between the German Ministry of Education and Research (BMBF), the German Aerospace Centre (DLR), and the EADS Astrium GmbH. The satellite design is based on technology and knowledge achieved from the successful SAR missions X-SAR, SIR-C and SRTM. The SAR sensor at X-band operates in different operation modes (resolutions) as illustrated in Figure 2.9:

- “Spotlight” mode with 10-10 km scenes at a resolution of 1–2 m

- “Stripmap” mode with 30 km wide strips at a resolution of 3–6 m
- “ScanSAR” mode with 100 km wide strips at a resolution of 16 m
- Additionally, TerraSAR-X supports the reception of interferometric radar data for the generation of digital elevation models

In operation modes, TerraSAR-X provides single or dual polarised data. On an experimental basis, additionally quad-polarisation and along-track interferometry are possible. TerraSAR-X is the next PolSAR satellite after ALOS. The mission’s objectives are the provision of high-quality, multimode X-band SAR-data for scientific research and applications as well as the establishment of a commercial EO market and to develop a sustainable EO-service business, based on TerraSAR-X-derived information products (Lee & Pottier 2009; Liang 2008).

In June 2010, TSX-1 was supplemented in orbit by its twin, the TanDEM-X instrument (TDX-1). In a close formation flight, they will separately acquire data for the TerraSAR-X mission and jointly execute the TanDEM-X mission data collection.

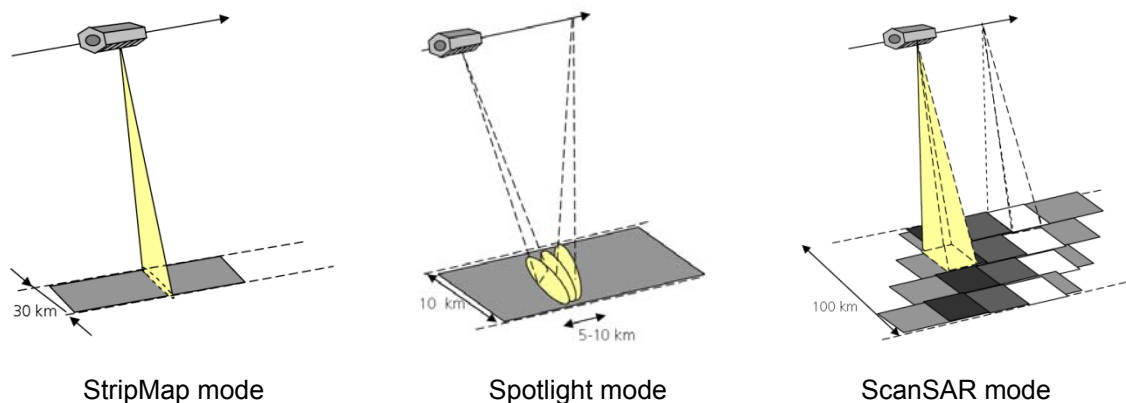


Figure 2.9. Imaging geometry in different acquisition modes (www1).

### 2.1.7 ALOS/PALSAR

The Japanese Earth-observing satellite program consists of two series: those satellites mainly used for atmospheric and marine observation and those mainly used for land observation. ALOS has been developed to contribute to the fields of

mapping, precise regional land coverage observation, disaster monitoring, and resource surveying. The development of PALSAR was a joint project between JAXA and JAROS. It has been successfully launched on 24 January 2006, and JAXA has started providing “ALOS data” to the public on 24 October 2006. The ALOS has three remote-sensing instruments: the panchromatic remote-sensing instrument for stereo mapping (PRISM) for digital elevation mapping, the advanced visible and near infrared radiometer type 2 (AVNIR-2) for precise land coverage observation, and the phased-array L-band SAR (PALSAR) for day-and-night and all-weather land observation. PALSAR is an active microwave sensor using L-band frequency to achieve cloud-free and day-and-night land observation and is considered to be the first fully PolSAR satellite. In its experimental polarimetric mode, it images a swath 20–65 km wide in full (quad) polarisation, with a resolution of 24–89 m. In the fine resolution mode, PALSAR can acquire partially polarimetric data at a resolution down to 14 m. The acquisition modes of PALSAR are shown in Figure 2.10 (Lee & Pottier 2009).

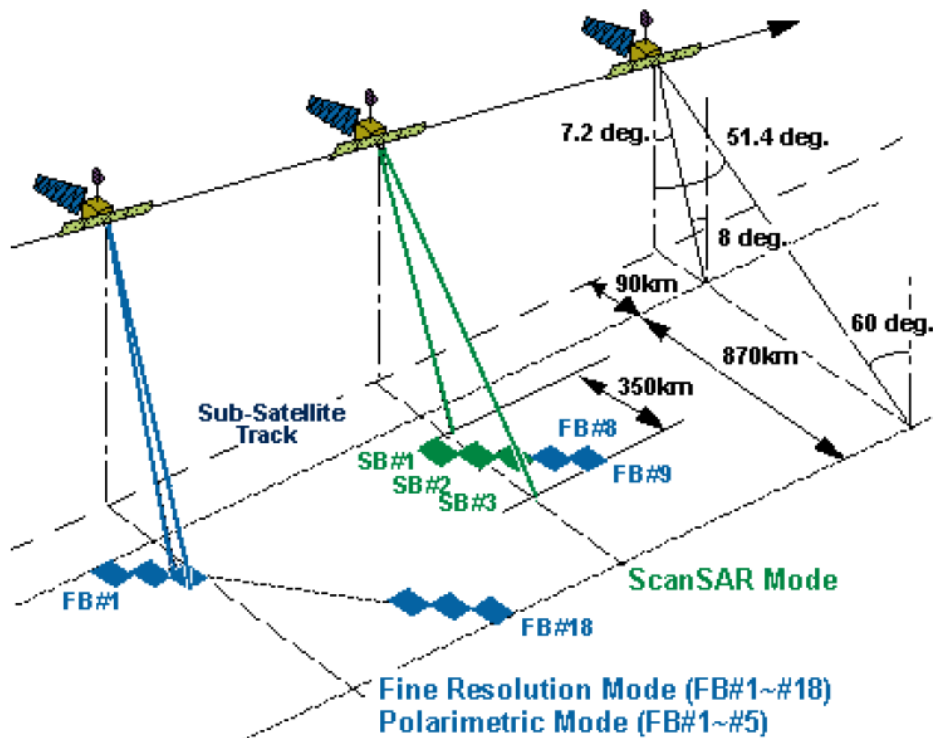


Figure 2.10. PALSAR acquisition modes (www2).

## **2.2 Agricultural Applications with Radar**

Remote sensing observations have been used for identification and monitoring of agricultural targets since the late 19th century. Over the last three decades, the use of radar sensors for various agricultural applications has been intensively studied. The all-weather, day or night data acquisition capability of radar systems provides a more reliable data source than the optical sensors which are limited by solar illumination, cloud cover and haze (Henderson *et al.* 1998).

### **2.2.1 Microwave Interaction with Agricultural Targets**

Basically, system parameters affecting radar backscatter, namely frequency, polarisation and incident angle, and target parameters influence the scattering process.

#### **2.2.1.1 System Parameters**

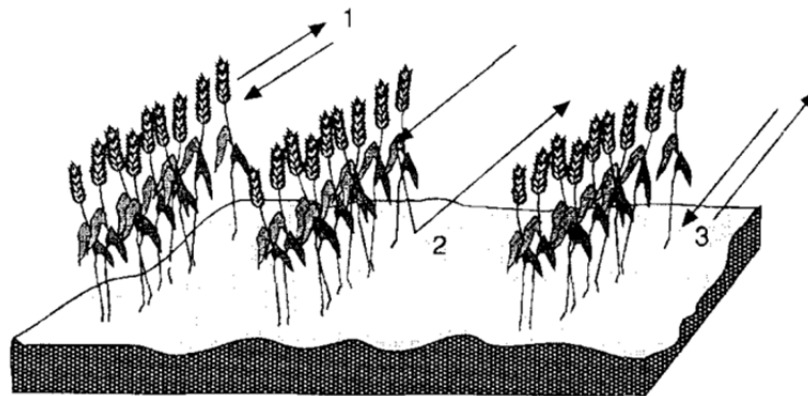
Frequency (or wavelength), incident angle, and polarisation are the primary system parameters used to define a radar sensor.

##### **Effect of Frequency**

Vegetation is a multi-component structure consisting of free water and the actual vegetation itself, which is a mixture of bounded water and air (Kozlov, Ligthart & Logvin 2004). Therefore, the frequency dependence of the dielectric constant is very important in the interaction process. In addition, the magnitude of radar backscatter from agricultural targets is dependent upon the relationship between wavelength and plant (part) size and/or penetration depth (Henderson *et al.* 1998). The radar signal penetration depth increases as the wavelength increases and is a function of the characteristics of the detected surface (Gomarasca 2009). Thus, the backscattered energy is the vector sum of EM fields scattered from the elements of the vegetation canopy (Figure 2.11) and those scattered from the soil beneath (Henderson *et al.* 1998).

Accordingly, L-band operation is used if some penetration into the ground or foliage is required, while X-band operation is used for studies related to short

vegetation, crops, leaves, and twigs (Fourikis 2000). In addition, roughness plays a role, as every crop will be rough above a certain frequency. The dependence of radar backscatter will decrease with increasing incidence angle (Buiten & Clevers 1993).



- 1 Direct Canopy (including multiple scattering)
- 2 Soil/Canopy Interaction
- 3 Direct Soil (including multiple scattering)

Figure 2.11. Sources of radar backscatter from cultivated crops (from Henderson *et al.* 1998).

### Effect of Polarisation

The radar backscatter of vegetation depends on polarisation (Buiten & Clevers 1993). Beyond a critical volume of vegetation canopy, the multi-scattering mechanisms arise and resulted in a depolarization effect. Therefore, cross-polarization (i.e. HV) is generated significantly by vegetation while the ground contribution produces practically no cross-polarization (Massonnet & Souyris 2008). Accordingly, the vegetation canopies influence, in different behaviour, the reflected wave polarization, which then provides information about their identity. Moreover the type of polarization influences also the radar signal penetration into canopies with vertical structures and those planted in strips (Gomasasca 2009; Thomas 2008).

### Effect of Incident Angle

It is obviously a function of the wavelength as well as the crop type and its development stage. Shorter wavelengths will penetrate less plant material; while

higher biomass crops will stronger attenuate the microwave signal. Conversely, the path length through the vegetation increases as the incident angle increases (i.e.,  $> 40^\circ$ ), thus maximising the crop response. As the radar signal propagates through the canopy, its mean (statistical) strength decreases exponentially with increasing canopy height as a result of microwave absorption and the scattering out of the propagation direction (Henderson *et al.* 1998).

### **2.2.1.2 Target Parameters**

The radar backscattered energy is influenced by geometrical and dielectric characteristics of crops and soils. Hence, vegetation canopies may be divided into several groups, depending on the complexity of the canopy architecture and the sizes of the scattering elements relative to the wavelength (Henderson *et al.* 1998).

#### **Crop Type**

Crop phenology governs the plant water-content and thus the crop's dielectric properties. When crops mature, the water content decreases which generally reduces the contribution to  $\sigma^\circ$  from the plants and increases the penetration of the transmitted microwave energy into the vegetation which can then increase the soil contribution to the total backscatter (Wilson & Ulaby 1984). Furthermore, some crops require particular cultivation practices (i.e. small soil-ridges) which may influence the radar backscatter according to the looking direction (Brisco *et al.* 1991).

#### **Plant Parameters**

Several parameters consistently show significant correlations including plant height, leaf area index (LAI), plant biomass, and plant water content (Bouman 1991; Daughtry, Ranson & Biehl 1991; Henderson *et al.* 1998; Major, Brisco & Brown 1991).

#### **Soil Parameters**

For all bare-soil surfaces, most residue-covered surfaces, and some vegetated fields, soil surface roughness and moisture content are important factors

governing  $\sigma^\circ$  (Ulaby, Moore & Fung 1986). Soil-type effects the radar backscatter through the soil water holding characteristics and the relative amounts of bound and free water-contents (Dobson, Kouyate & Ulaby 1984). Other soil parameters such as organic matter, salinity, etc. have been shown to have some effect, although to a lesser degree than roughness and water content (Henderson *et al.* 1998).

### 2.2.2 Crop Type Identification

A single channel and date of SAR data contains useful information for crop classification, however, low accuracies are typically obtained unless the region in question is characterised by a few crop types which are significantly different with respect to their microwave signatures. Thus, the classification results can be improved using the multi-dimensional SAR data, as the multi-sensor data utilise the synergism between SAR and optical data. The repetitive observations from the same platform in a multi-date approach could be The easiest way to generate multi-dimensional data (Henderson *et al.* 1998). Due to crop development and soil moisture changes, the multi-temporal behaviour of the backscattering coefficient in different fields during the year changes. Therefore, the crop definition in the images becomes better (Oliver & Quegan 2004).

Multi-frequency approach affords more information of a SAR data-set for crop-identification purposes. Since the relationship between crop geometry and wavelength ensures that different information is obtained from the same crop as a function of frequency (Henderson *et al.* 1998). Recently, Multi-polarisation technique is increasingly important as the fully polarimetric SAR data are now being available (Evans *et al.* 1988; Ulaby *et al.* 1987). Likewise, combining polarisations from different sensors revealed significant classification improvement (Ulaby, Batlivala & Bare 1980). Multi-sensor approaches are also very useful for crop identification as most studies report a synergism between optical and microwave sensors (Ulaby, Li & Shanmugan 1982). On the other hand, the combination between the tone and texture extracted from a single image is considered as a multi- feature approach for crop classification (Treitz *et al.* 1993) and forest classification (Ulaby, Moore & Fung 1986).

### 2.3 Soil Moisture Extraction from SAR Data

Soil moisture information is an important input to crop development models to set the initial conditions in the spring. The radar backscatter is related to soil moisture at the surface and, subsequently, this information is related to the lower layers of the soil. Also, soil moisture data is important for the hydrological models, as it is a critical state variable of the watershed in assessing flood hazards (Henderson *et al.* 1998). Microwave remote sensing can provide a direct measurement of the surface soil moisture (Liang 2004). Basically, two properties govern the backscatter response observed by the SAR system: the permittivity of the medium and the roughness characteristics of the surface. Both parameters are, in turn, related to different geophysical parameters of the soil. With the advent of the polarimetric SAR, radar remote sensing of soil moisture has attained significant prominence in the past two decades (Liang 2008; Zhongxin *et al.* 2008).

#### 2.3.1 Importance of Microwaves in Soil Moisture Content

Soil-moisture studies are not suitable for non-microwave regions due to the following:

- (a) The reflection coefficient is not so sensitive to soil moisture variations in the visible region compared to its equivalent parameters like reflectivity and emissivity in other regions of the EM spectrum.
- (b) Scattering and attenuation due to atmosphere are high.
- (c) The reflection coefficient is highly sensitive to soil surface roughness and vegetation cover variation.

Microwave sensors offer the potential for remote sensing of soil moisture because of the big change due to the addition of water makes to the dielectric constant of dry soil (Alharthi & Lange 1987).

#### 2.3.2 Dielectric Behaviour of Wet Soils

The dielectric constant ( $\epsilon'$ ) of dry soil is essentially independent of temperature and frequency. The imaginary part  $\epsilon''$  is  $< 0.05$ . Wet-soil behaviour is, however, very complex. The dielectric behaviour of soil-water mixtures has been studied over the past two decades (Alex & Behari 1996; Ghosh, Pyne & Behari 1998; Roth *et al.* 1990; Scott & Smith 1992). A wet-soil medium is a mixture of soil particles,

air pockets and liquid water. This water is usually divided into two fractions; namely bound water and free water. The relative fractions of bound and free water are related to the particle size distribution (soil texture). These, in turn, are dependent upon the bulk soil density and the shape of the water inclusions (Behari 2005).

### 2.3.3 Soil Moisture Measurements

In the microwave region, the dielectric constant of soil is very sensitive to the soil-volumetric moisture content  $m_v$  (Buchroithner & Granica 1997; Henderson *et al.* 1998). Thus, microwave sensors are well-suited for soil remote-sensing due to the sensitivity to soil-moisture variation together with their relative transparency of the atmosphere (> 90%) (Behari 2005). Owing to the large disparity between the dielectric constant of dry soil surfaces (3-5) and of water (approximately 80) at microwave frequencies, therefore, adding a relatively small amount of water to the soil drastically changes the value of the dielectric constant (Van Zyl 2011).

For example, at L-band the real part of the dielectric constant ranges from 3 for dry soil to about 25 for saturated soil. This variation can result in a change in the order of 10 dB in the magnitude of the radar-backscatter coefficient (Oh, Sarabandi & Ulaby 1992). Also, with a proper choice of frequency, look angle and polarisation, the effect of surface roughness can be minimised (Behari 2005).

### 2.3.4 Roughness Estimation

Several investigators (Boisvert *et al.* 1997; Zribi *et al.* 2003) have pointed out that the difference  $\Delta\sigma^0$  between signal measurements (in dB) taken at two different incidence angles is essentially linked to soil roughness and depends only weakly on soil moisture. Therefore:

$$\sigma^0(\theta_1) - \sigma^0(\theta_2) \approx h(\text{roughness}) \quad (2.7)$$

The soil roughness can be estimated by fitting the  $\sigma^0$  angular differences to the IEM predictions.

### 2.3.5 Penetration Depth

The penetration depth is often referred to as the skin depth. It is one of the basic concepts in electromagnetic remote sensing. An expression for the penetration depth  $P_d$  can be obtained by considering a wave incident from air upon a soil surface in the z-direction. In general, a part is scattered back into the air and the remaining is penetrated into the medium. Knowing the dielectric properties of the materials involved, penetration depth  $P_d$  can be calculated by the following relation (Behari 2005):

$$P_d = \lambda (\epsilon')^{0.5} / 2 \pi \epsilon'' \quad (2.8)$$

The effect of frequency must be considered when interpreting multi-frequency radar imagery. The multi-frequency data may allow the distinction between roughness types, as the different wavelengths are to a varying extent sensitive to varying roughness of the investigated surface (Elachi 1988). Also the attenuation and scattering by the vegetation canopy increases with increasing frequency. Therefore, for soil moisture sensing, lower frequencies are preferable to higher frequencies. In addition to their advantages like a higher penetration capability into the soil (Schmullius & Furrer 1992).

### 2.3.6 Target Parameters Influencing Microwave Signatures

#### 2.3.6.1 Effect of Soil Texture and Roughness

In general the influence of the soil type onto the complex dielectric constant is weak and the influence of soil moisture is dominant (Buiten & Clevers 1993). At any given moisture content and at all given frequencies,  $\epsilon'$  is found to be roughly proportional to the sand content. And the effect of soil texture decreases with the frequency. Alex and Behari (1996) concluded that in the case of dry soils the dielectric parameters are not sensitive to the soil texture. However, for wet soils ( $m_v > 0.2$ ) the dielectric parameters are significantly dependent upon soil texture (Alex & Behari 1996). On the other hand, it was observed that the use of lower frequencies can minimise the variation of the scattering coefficient  $\sigma^0$  related to surface roughness (Ulaby, Li & Shanmugan 1982). Following Jackson and O'Neill (1985) it can be summarised as follows:

- (a)  $\sigma^0$  increases with increasing soil moisture, incidence angle  $\theta$  and frequency.
- (b) Maximum correlation between  $\sigma^0$  and soil moisture occurs at frequencies near 4.5 GHz and incidence angle near  $10^\circ$ , with preference for like polarisation (Jackson & Oneill 1985).

### 2.3.6.2 Bulk Density Effects

It has been demonstrated that for a given soil at a given gravimetric moisture-content  $mg$  the measured dielectric constant  $\mathcal{E}$  is proportional to the soil bulk density  $\rho$  (Hallikainen *et al.* 1985). The effect of soil bulk density on the dielectric constant of the soil can be reduced significantly using the volumetric soil moisture content instead of the gravimetric one. Electromagnetically, the volumetric measure is preferred because the dielectric constant of the soil-water mixture is a function of the water volume fraction in the mixture (Chukhlantsev 2006). Assuming the soil to be homogeneous, the randomly dispersed mixture of solids, liquids and air along with all inclusions, is much smaller than the wavelength (Dobson *et al.* 1985).

### 2.3.6.3 Effect of Vegetation

The sensitivity of  $\sigma^0$  to soil moisture is in general decreased by the presence of a vegetation cover. This is due to increased scattering and attenuation of the electromagnetic signal (Tansly & Millington 2001). When a soil is covered by vegetation the backscattering power from soil suffers a two-way attenuation due to its propagation through the vegetation layer. In general, the attenuation is a function of the vegetation parameters such as plant height, density, water content and shape of the plant. In addition, the vegetation layer contributes a backscatter component of its own due to volume scattering (Demirican, Ramach & Mauser 1992). The sensitivity also decreases with the increase of incidence angle and frequency. Moreover, like-polarisation has a better correlation with  $\sigma^0$  than cross polarisation. In conclusion, the preferred approach is to have a single algorithm relating the backscattering coefficient  $\sigma^0$  with the soil moisture for bare and vegetation-covered soil (Mehta *et al.* 1995).

### 2.3.7 Volumetric Soil Moisture Using Backscattering Data

For bare soil the backscattering coefficient  $\sigma^\circ$  is related to soil moisture by the expression:

$$\sigma^\circ = A \exp(BM) \quad (2.9)$$

where  $A$  and  $B$  are constants and  $M$  is the soil moisture content. Eq. (2.9) can be rewritten as:

$$\sigma^\circ \text{ (dB)} = 10 \log \sigma^\circ = 10 \log A + 4.34 BM = A_1 + SM \quad (2.10)$$

where  $A_1 = 10 \log A$  and  $S = 4.34 B$ . The radar sensitivity to soil moisture  $S$  is given as:

$$S = \frac{\delta \sigma^\circ}{\delta M} \quad (2.11)$$

The radar response to soil moisture is determined using linear regression analysis in accordance with the above equations (Behari 2005; Schmugge 1983a; Ulaby, Razani & Dobson 1983). Zribi *et al.* (2003) stated that the volumetric soil moisture  $m_v$  up to value around 35-40% is linearly related to the backscattering coefficient  $\sigma^\circ$  by the relation:

$$m_v = A + B \cdot \sigma^\circ \text{ (dB)} \quad (2.12)$$

where  $A$  and  $B$  are constants to be obtained from  $m_v$  vs  $\sigma^\circ$  curve. These can be applied to the SAR images, whereby classification can be done by moisture range. The slope of regression curve is almost the same for all test fields and soil moisture change show linearity of a similar type. In general:

$$\Delta m_v = m_{v,2} - m_{v,1} \quad (2.13)$$

The change in volumetric soil-moisture is given in terms of change in the backscattering coefficient:

$$\Delta m_v = A' \Delta \sigma^\circ \text{ (dB)} \quad (2.14)$$

Where  $\Delta \sigma^\circ$  is the backscatter change, i.e.  $\Delta \sigma^\circ = \sigma^\circ \text{ (dB)} - \sigma^\circ_1 \text{ (dB)}$  and  $A'$  is a constant pertinent to the given set of measurements (Zribi *et al.* 2003). The advantages of this method are: (i) the errors due to the unknown roughness remain relatively small, and the exact slope of regression is approximated within a

soil-moisture change estimation-error of 10%; (ii) calibration error (e.g. local topography etc.) does not affect the quality of the result, as long as the calibration is uniformly maintained for both the measurements and (iii) influences of the incidence angle may also be neglected. Therefore it is a useful method for measuring the soil moisture with a certain degree of accuracy. However, using this method only permits the estimation of the moisture change and not the absolute soil moisture (Behari 2005).

With no a priori information about surface roughness, several approaches may be considered. The simplest approach is to select the proper radar parameters (i.e., polarisation configuration), so that  $\sigma^\circ$  is almost independent of surface roughness (over reasonably wide range), while retaining a strong sensitivity to moisture content. The next approach is using dual-frequency radar system to separate the effect of roughness and moisture on  $\sigma^\circ$ . Another possible approach is to use change detection, whereby two images of the same scene, recorded on two different (but closely spaced) dates, are co-registered, and the difference in grey level is used to estimate the change in moisture content over the time period between the two observations (Ulaby, Moore & Fung 1986).

### 2.3.8 Time Domain Reflectometry (TDR)

TDR operates in the frequency range of 1 MHz to 1 GHz, well below the relaxation frequency of water. Only a little frequency dependence of  $\mathcal{E}'$  across this range has been reported, although the electrical conductivity contributes to dielectric loss if the solution contains ions.  $\mathcal{E}''$  is generally small and insignificant in non-saline homogenous soils (Behari 2005).

The use of remote shorting diodes and calibrated reference airlines can, in many cases, considerably improve the accuracy of TDR measurements (Topp, Zegelin & White 1994). The signal-to-noise ratio of the reflected signals can be increased by using remotely switched diodes. This combined with a waveform subtraction procedure provides a reliable identification of the two reflections that define  $\mathcal{E}_{air}$ . The high resolution TDR system offers many advantages of detecting very small changes in soil water content (Pepin, Livingston & Hook 1995).

## 2.3.9 Radiometric Calibration

### 2.3.9.1 Sigma Naught $\sigma^0$

Sigma naught represents the average reflectivity of a horizontal material sample, normalised with respect to a unit area  $A_L$  on the horizontal ground plane (Figure 2.12), also called the *scattering coefficient* (Ulaby, Moore & Fung 1981). Sigma naught is a dimensionless parameter, as it represents the ratio of the statistically averaged scattered power density to the average incident power density over the surface. It depends on the given frequency, the polarizations of the incident and scattered waves, and the incident and scattering directions (Lee & Pottier 2009).

### 2.3.9.2 Gamma $\gamma$

Gamma is defined with respect to the incident area  $A_i$  orthogonal to the incident ray of the radar (Figure 2.12). Also, it is called normalised backscatter coefficient, as it results from dividing  $\sigma^0$  by  $\cos \theta$ . Therefore, plots of  $\gamma$  as a function of incident angle are more constant than comparable plots using  $\sigma^0$  (Henderson *et al.* 1998; Stimson 1998).

### 2.3.9.3 Radar Brightness $\beta^0$

Radar brightness is the default radiometric observable of a radar. By means of  $\beta^0$ , the system radiometric response can be separated from the reflectivity dependence on terrain properties; accordingly, it does not require knowledge of the local incidence angle. If the slant range/azimuth area increment is set by the pixel spacing  $\Delta_R$  and  $\Delta_A$  respectively, then the quantity  $\beta^0 \Delta_R \Delta_A$  is the observed radar reflectivity per (two-dimensional) slant range pixel (Henderson *et al.* 1998).

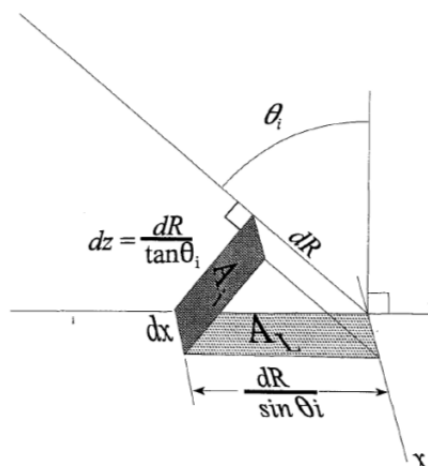


Figure 2.12. Definition of surface and incident area (from Henderson 1998).

### 3 Study Area and Data Preparation

In this section, the study area is described. The characteristics of the used SAR data (TerraSAR-X and ALOS PALSAR) are discussed in quite details. Moreover, the general data-processing techniques applied to the data are explained.

#### 3.1 Description of the Study Area

The study area is located in the free state of Saxony, Germany. It extends from Pirna town in the north, to the border between Germany and Czech Republic in the south, and covers the Gottleuba Catchment. The study area lies between latitude  $50^{\circ} 46' 13''$  N to  $50^{\circ} 58' 02''$  N, and longitude  $13^{\circ} 48' 38''$  E to  $14^{\circ} 02' 19''$  E, with an area of about  $350 \text{ km}^2$  (Figure 3.1). The elevation of study area varies from about 110 m ASL in the north (around Elbe River) to about 655 m ASL in the southern part (Figure 3.2a). The relief in the northern part is rather plain, while in the middle is more undulated. The southern part is a mountainous area and characterized by the hills of the Erzgebirge mountain range (Figure 3.2b).

The study area is characterised by different land-use types (Figure 3.3). From which the agricultural area, in addition to the grass area (for grazing animals) were selected in the current study. The main cultivated crops in the study area are cereal, maize and rape.

The study area covers three types of the soil regions in Saxony. The northern part of the study area is characterised by the loess and sandy loess landscapes, the eastern part is dominated by soils of the mountain and hill regions with a high proportion of sandstone, and the western part covers the soils of the mountain and hill regions with a high proportion of magmatic and metamorphic (Figure 3.4). Furthermore, the surface soil texture of the study area is illustrated in Figure 3.4.



Figure 3.1. Location of the study area.

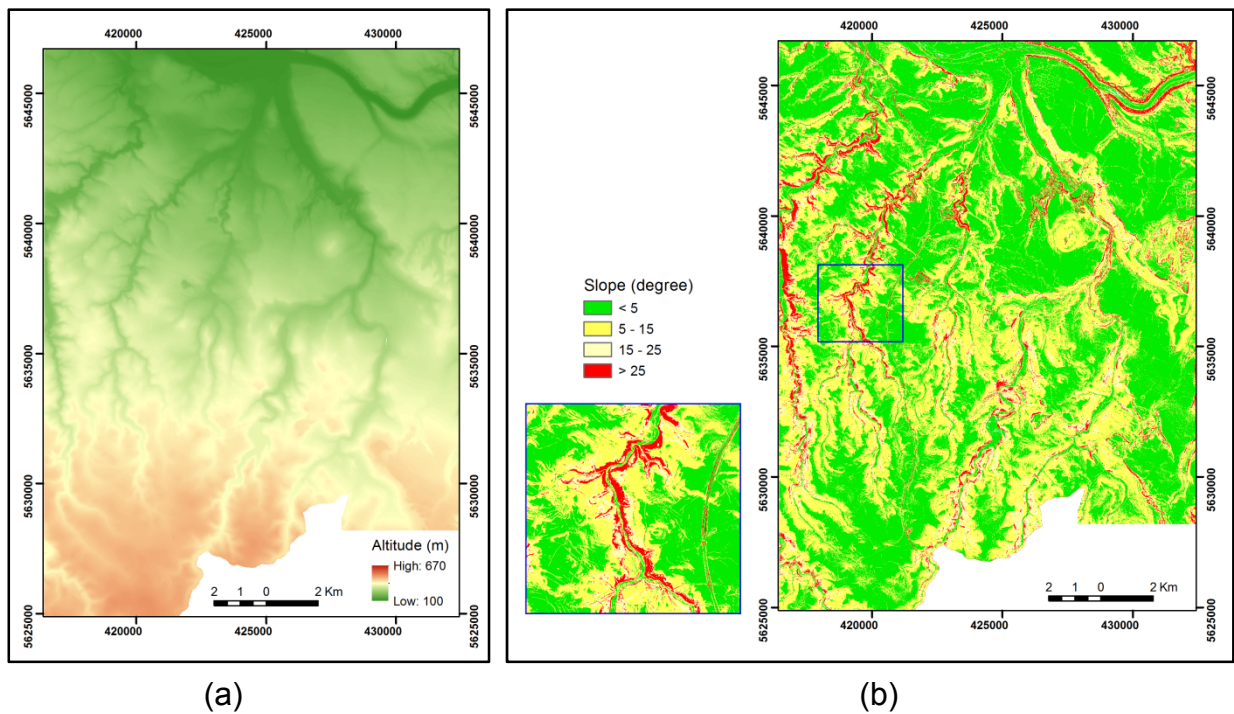


Figure 3.2. a) Hypsometric colouring of the DTM, and b) Slope map of the study area.

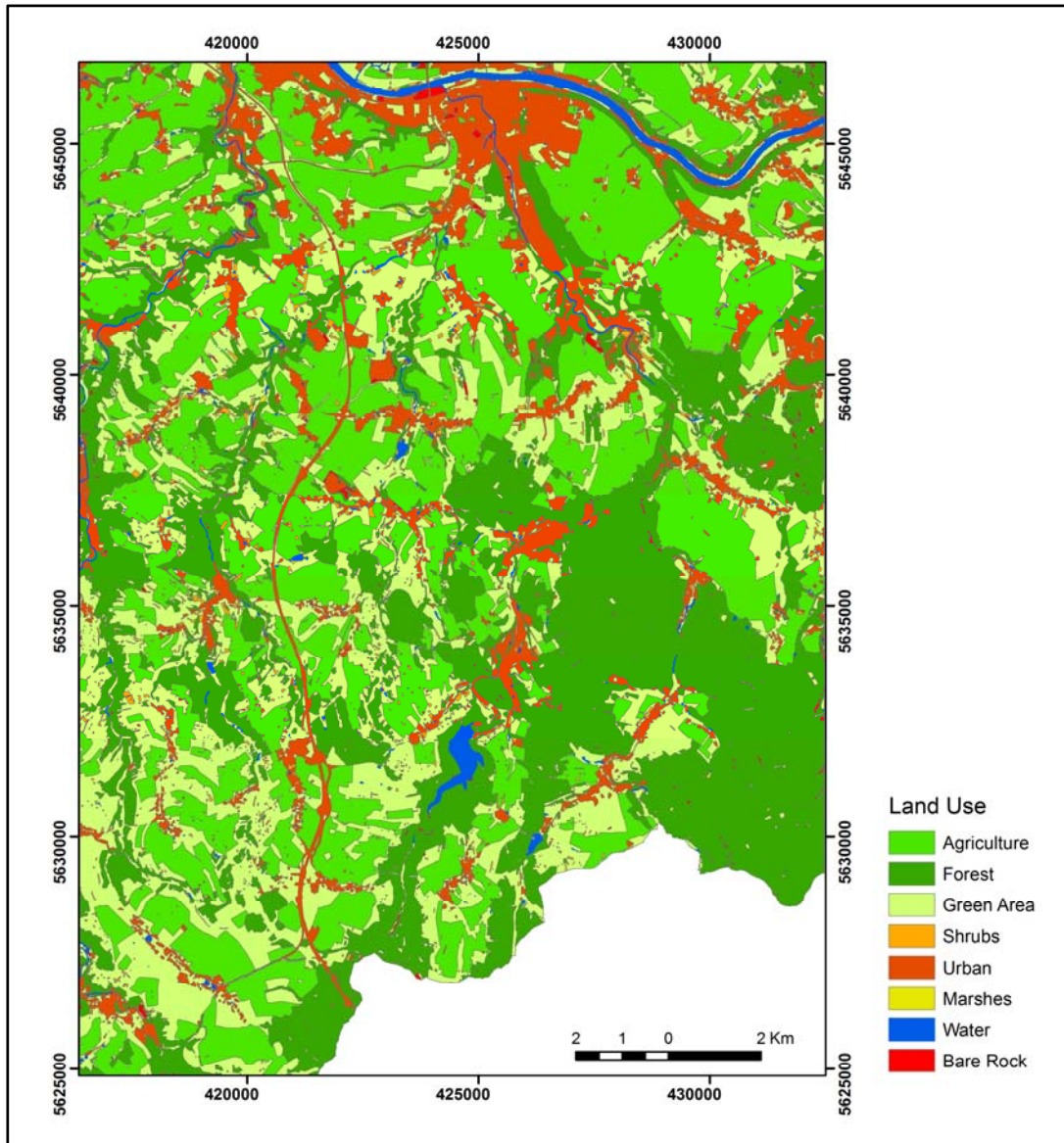


Figure 3.3. Land use map (2005) of the study area (source: GeoSN, Germany).

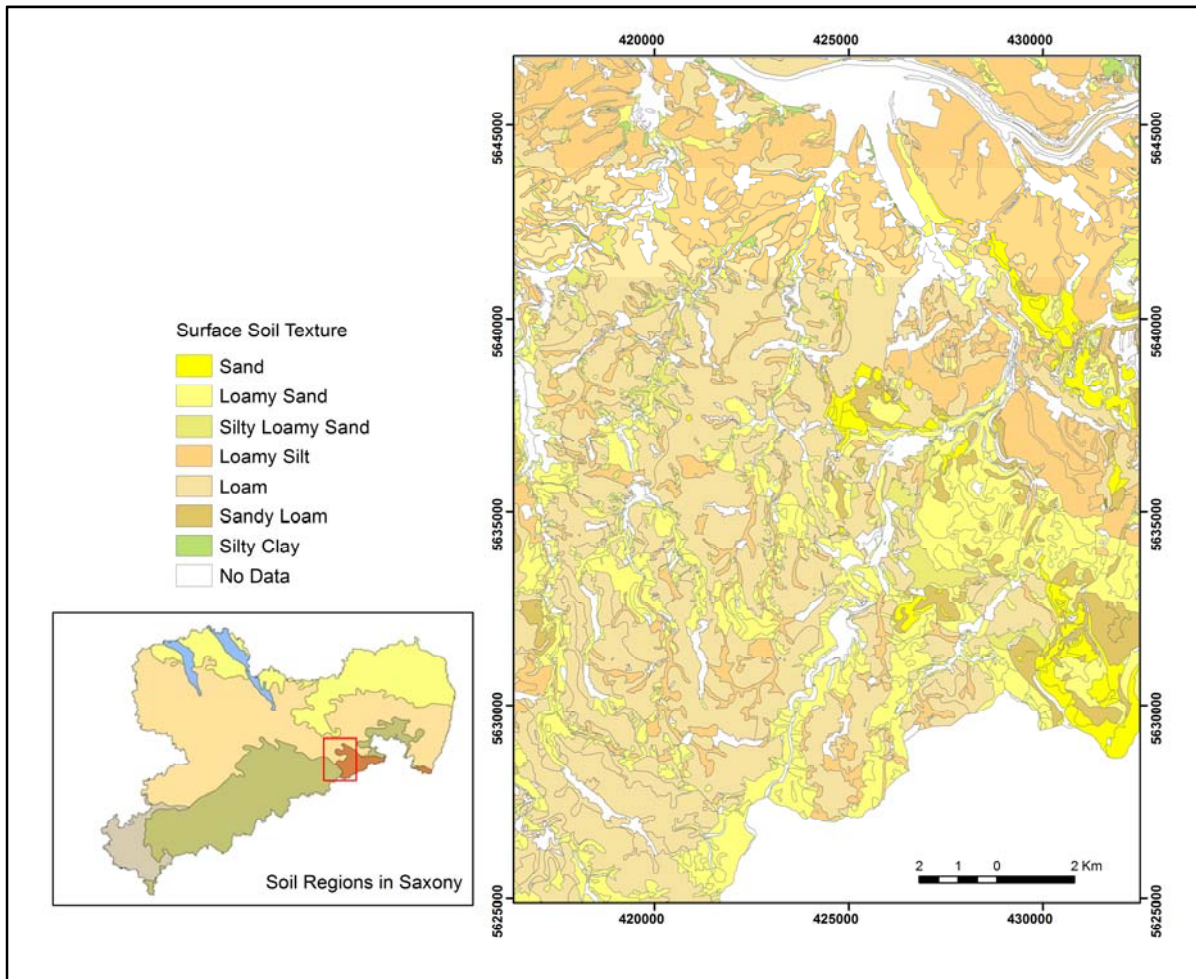


Figure 3.4. Surface soil texture of the study area (source: www3).

The climate can be described as that of Saxony as the study area is a part thereof. The mean annual air temperature in Saxony is 7.6 °C (Table 3.1). Monthly mean temperatures below zero are only observed in January and February. The warmest month is July with a mean air temperature of 16.1 °C. The increase in annual air temperature in Saxony is 0.3 °C/decade ( $P < 0.01$ ). This means that in the last 40 years the temperature rose by 1.2 °C. Spatial differences of air temperature in Saxony are mainly determined by topography. The warmest areas are located in the northern lowlands and along the river Elbe. In the low mountains the temperature is reduced. The coldest regions can be found on the peaks of the Erzgebirge mountain range in southern Saxony (Chmielewski, Muller & Kuchler 2005). The precipitation average is ca. 800 mm a<sup>-1</sup> with a relatively even distribution throughout the year.

Table 3.1. Monthly and annual mean air temperature (°C) in Saxony 1961–2000, as well as trends (°C per decade) (from Chmielewski *et al.* 2005).

	January	February	March	April	May	June	July	August	September	October	November	December	Year
Mean	-1.2	-0.4	2.9	7.0	11.6	14.5	16.1	15.8	12.9	8.4	3.3	0.0	7.6
SD	3.0	3.0	2.3	1.4	1.5	1.1	1.6	1.2	1.5	1.5	1.7	2.4	0.8
Trend	+0.7	+0.4	+0.5	+0.2	+0.5	+0.0	+0.3	+0.5	+0.0	+0.0	-0.1	+0.6	+0.3
<i>P</i>	<0.10	-	<0.10	-	<0.01	-	-	<0.01	-	-	-	<0.10	<0.01

## 3.2 Data Sources

### 3.2.1 SAR Data

In the current study, it was planned to investigate both TerraSAR-X (TSX) and ALOS PALSAR data for land cover and soil moisture mapping. Out of the proposed data sets, 4 TSX images and one PALSAR image have been acquired. These data sets have been applied to achieve plot-based land-cover and soil-moisture maps (cf. Figure 3.9).

#### 3.2.1.1 TerraSAR-X Data

Two TSX (HH) images acquired in the StripMap mode on 31/05/2010 and 17/06/2010 (Figures 3.5), and one TSX (HH/HV) images acquired on 18/04/2011 (Figure 3.6a). The look direction for all images is right. Table 3.2 illustrates the main characteristics of the TSX data. Figure 3.5 shows the TSX data of 31/05/2010 and 17/06/2010 of the study area with the plot boundaries in red colour.

#### 3.2.1.2 ALOS PALSAR

The succeeded acquisition covering the study area was on 31/05/2010. Figure 3.7 shows the status of the ordered PALSAR data. Data management and ordering was going through the EOLi-sa tool which allows users to access the catalogues of ESA's Earth Observation data products. The main characteristics are illustrated in Table 3.2. The PALSAR data of the study area is shown in Figure 3.6b.

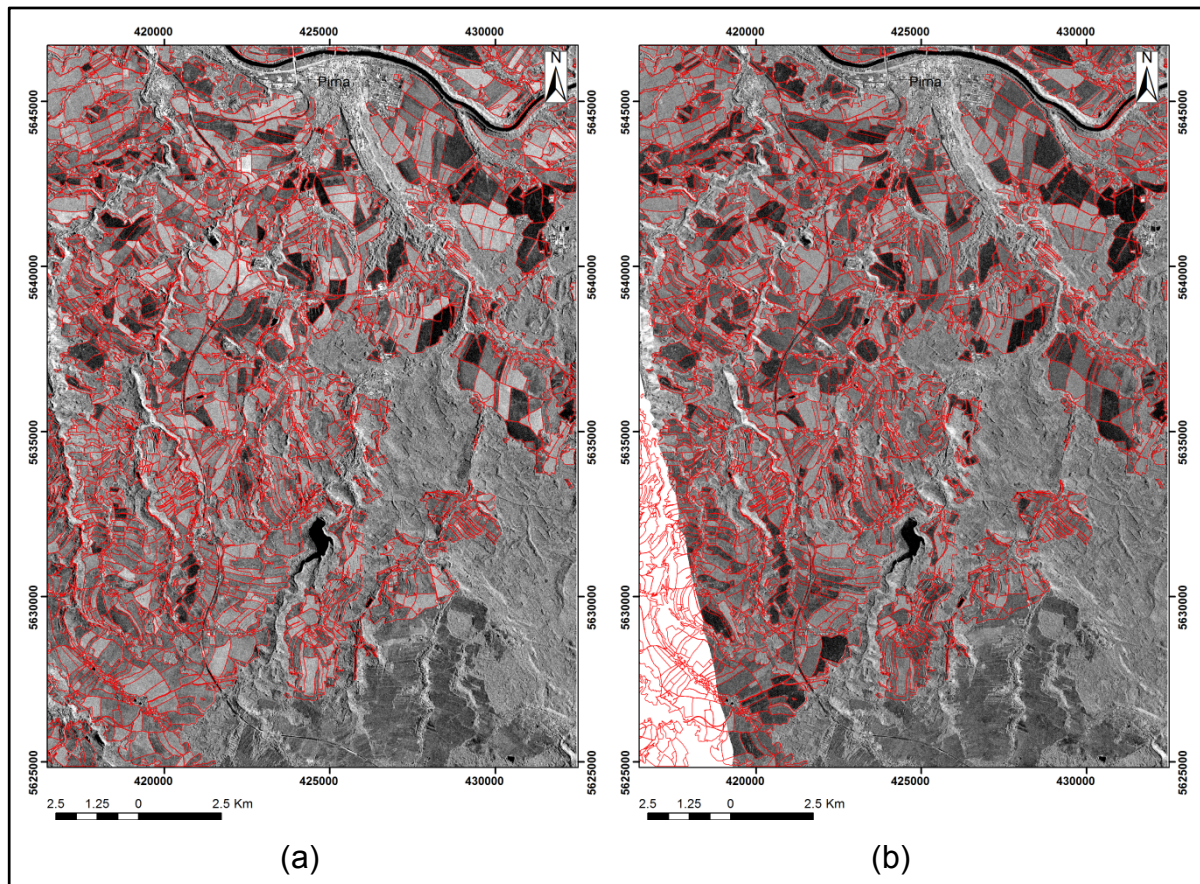


Figure 3.5. a) TSX image acquired on 31/05/2010 and b) TSX image acquired on 17/06/2010. Redlines: parcel boundaries.

Table 3.2. SAR images specification.

Sensor	Date	Overpass	Mode	Polarisation	Incidence angle range	Resolution
TerraSAR-X	31/05/2010	ascending	SM	HH	41.76° – 43.89°	3 m
	17/06/2010	ascending	SM	HH	29.66° – 32.42°	3 m
	18/04/2011	descending	SM	HH+HV	40.98 – 42.08	3.75 m
ALOS/PALSAR	31/05/2010	ascending	FBD	HH+HV	34°	12.5 m

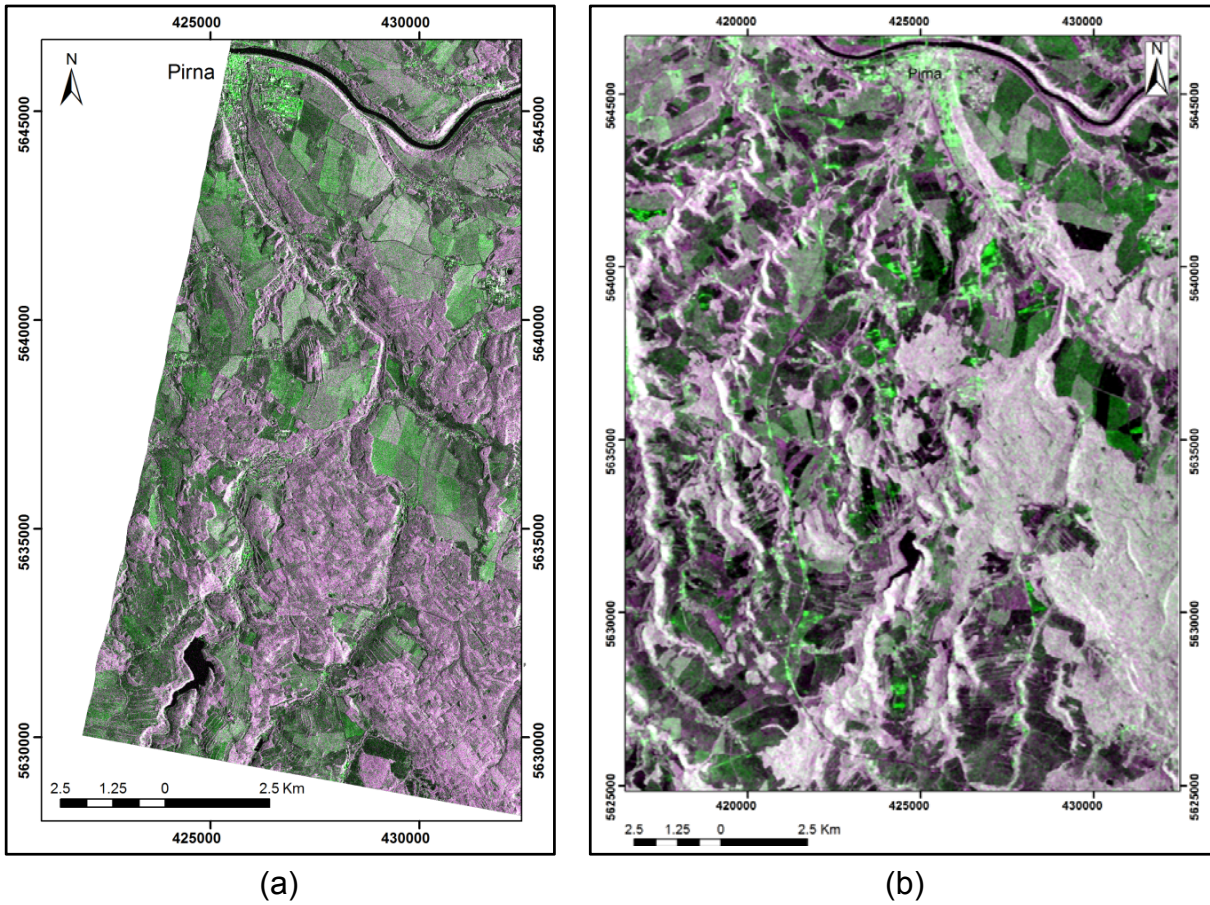


Figure 3.6. a) TSX image of 18/04/2011 (RGB: HV, HH, HV) and b) ALOS PALSAR imagery (RGB: HV, HH, HV) acquired on 31/05/2010.

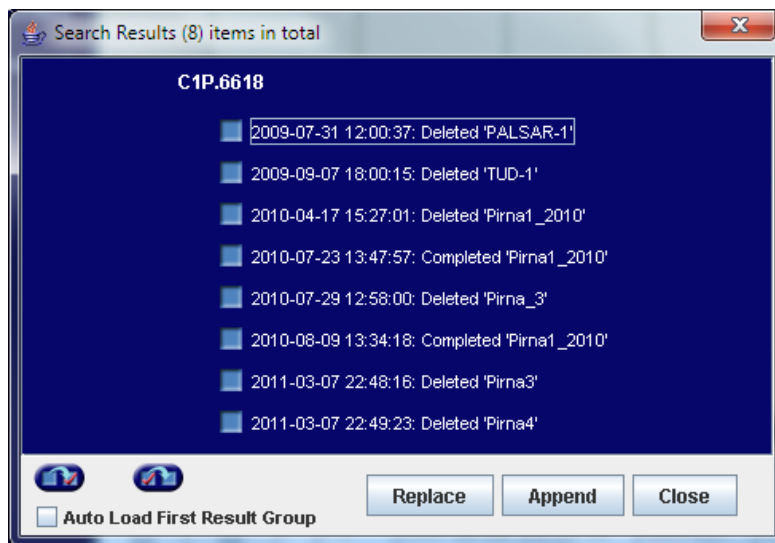


Figure 3.7. Status of the ordered PALSAR data.

### **3.2.2 Digital Ortho-Photos (DOP)**

The digital ortho-photos for the study area were obtained from the *Staatsbetrieb Geobasisinformation und Vermessung Sachsen* (GeoSN), Germany. The DOP was provided in colour (red-green-blue) with spatial resolution of 20 cm.

### **3.2.3 Digital Terrain Model (DTM)**

The DTM (Figure 3.2 a) was obtained from the *Staatsbetrieb Geobasisinformation und Vermessung Sachsen* (GeoSN), Germany. For this DTM data (ATKIS-DGM2) the laser scanner measuring absorption as the primary data collection method is applied. The data is provided with a grid spacing of 2 meters. The height accuracy of the grid points is  $\pm 0.2$  m (www4).

### **3.2.4 Field-Map**

The field-map showing the field boundaries was obtained from the webpage of the “Landwirtschaft in Sachsen” (www5), where number of sheets were downloaded to cover the study area (Figure 3.2).

## **3.3 Instrument and Software**

### **3.3.1 Instruments**

**TDR:** Volumetric soil moisture was measured in-situ using the Time Domain Reflectometry (TDR - HH2 Moisture Meter). The WET sensor detects the dielectric properties of the soil and sends that to the HH2 which calculate the soil moisture using its calibration tables (Delta-T 2005).

### **3.3.2 Software**

The current study has been utilised the following software:

- a. ERDAS IMAGINE 9.2
- b. ARCGIS 10
- c. ENVI
- d. ASF MapReady 2.3.6
- e. VISUAL BASIC .NET 2008
- f. “R” Programming Language

### 3.4 Data Preparation and Processing

#### 3.4.1 Radiometric Calibration of TerraSAR-X Data

TSX images were imported into ERDAS Imagine, and then backscattering coefficient ( $\sigma^\circ$ ) was calculated. According to Fritz and Eineder (2008), it can be derived either from the radar brightness ( $\beta^\circ$ ), or from the image pixel values (Digital Number (DN)) as the following (Fritz & Eineder 2008).

#### Radar Brightness ( $\beta^\circ$ )

$$\beta^\circ = k_s \cdot |DN|^2 \quad (3.1)$$

where

- DN is the pixel intensity values,
- $k_s$  is the calibration factor (also called calFactor), is given in the TerraSAR-X data delivery package annotation file “calibration” section. It is processor and product type dependent and might even change between the different beams of a same product type. Table (3.3) illustrates the calibration factor values for the used TSX data.

Equation (3.2) converts  $\beta^\circ$  to dB,

$$\beta^\circ_{dB} = 10 \cdot \log_{10} (\beta^\circ) \quad (3.2)$$

#### Sigma Naught (Radiometric Calibration)

$$\sigma^\circ = (k_s \cdot |DN|^2 - NEBN) \cdot \sin\theta_{loc} \quad (3.3)$$

where:

- NEBN is the Noise Equivalent Beta Naught. It represents the influence of different noise contributions to the signal.
- $\theta_{loc}$  is the local incidence angle. It is derived from the Geocoded Incidence Angle Mask (GIM) that is optional for the L1B Enhanced Ellipsoid Corrected (EEC) product ordering.

Table 3.3. Calibration factors for the used TerraSAR-X data.

Date	Polarisation	calFactor
31/05/2010	HH	9.08104534113524660E-06
17/06/2010	HH	1.19752740163255090E-05
18/04/2011	HH	9.52783674347650056E-06
	HV	1.90556734869530070E-06

### Geocoded Incidence Angle Mask (GIM)

The local incidence angle is the angle between the radar beam and the normal to the illuminated surface. The GIM provides information about the local incidence angle for each pixel of the geocoded SAR scene and about the presence of layover and shadow areas. The GIM product shows the same cartographic properties as the geocoded output image with regard to output projection and cartographic framing. The content of the GIM product is basically the local terrain incidence angle and additional flags indicating whether a pixel is affected by shadow and/or layover or not.

### Extraction of the Local Incidence Angle

$$\theta_{loc} = \frac{(GIM - (GIM \bmod 10))}{100} \quad (3.4)$$

- The resulting incidence angle is in degree (float value).
- "GIM modulo 10" represents the remainder of the division of GIM by 10.

The equation (3.3) can also be expressed in terms of Beta Naught, as:

$$\sigma^{\circ} = \beta^{\circ} \cdot \sin \theta_{loc} - NESZ \quad (3.5)$$

- NESZ is the Noise Equivalent Sigma Zero, i.e. the system noise expressed in Sigma Naught. It is specified in (Fritz & Eineder 2008) between -19dB and -26dB. For this reason the noise influence can often be neglected, depending on the considered application.

In the case NEBN is ignored equation (3.5) reduces to the equations (3.6) and (3.7),

$$\sigma^{\circ} = \beta^{\circ} \cdot \sin\theta_{loc} \quad (3.6)$$

$$\sigma^{\circ}_{dB} = \beta^{\circ}_{dB} + 10 \cdot \log_{10}(\sin\theta_{loc}) \quad (3.7)$$

Finally, the  $\sigma^{\circ}$  can be directly derived using the image pixel value (DN) and GIM file as expressed in equation (3.8)

$$\sigma^{\circ}_{dB} = 20 \cdot \log_{10} DN_i + 10 \cdot \log_{10}(\text{calFact}) + 10 \cdot \log_{10}(\sin\theta_i) \quad (3.8)$$

### Using DTM (2m) for Radiometric Calibration of TSX Data

In addition to the radiometric calibration using GIM file, the TSX image acquired on 31/05/2010 was utilized with the DTM (2m) to calculate sigma naught. The radiometric correction model available in ERDAS Imagine was applied to generate the incident file using the orbital information of the TSX on 31/05/2010 (the required model inputs were obtained from the corresponding XML file). Then, the generated incident file was used for calculating sigma naught.

### 3.4.2 Radiometric Calibration of ALOS PALSAR Data

ALOS PALSAR image were imported using the ASF Map Ready (V. 2.3.6; free software) which enables to apply ortho-rectification and radiometric correction to the original PALSAR image using the digital elevation model (DEM 2m). Appendix 1 shows the list of Software that supports PALSAR Products. Then the backscattering coefficient was calculated using Equation 3.9 (ALOS products 2007). The sigma-naught image was filtered using different filters with kernel size (3x3).

$$\sigma_i^{\circ}(dB) = 20 \log_{10} DN_i + Kdb \quad (3.9)$$

This equation transforms the digital number of each pixel  $DN_i$  (amplitude of the backscattered signal for pixel  $i$ ) into a backscattering coefficient ( $\sigma_i^{\circ}$ ), in decibels. The calibration constant for PALSAR L1.5 products is  $Kdb = -83$  dB.

### 3.4.3 Data Re-Scaling

One object of the current study is to test different quantisation levels in land cover classification. Therefore, a model in ERDAS Imagine was built to rescale the backscattering image into 32, 64, 128 and 256 grey-levels. Moreover, 2 standard-deviation and 3 standard- deviation of the input image were used to test the effect of such value on the classification process.

### 3.4.4 Plot Mapping and Sampling

The plot map of the study area has been revised using the TerraSAR-X images, in addition to the DOP for more details if required. Sample and reference plots were chosen after completion of ground truth, and the information added to the attribute table of the plot map.

### 3.4.5 Speckle Reduction and Signal to Noise Ratio

Various filter types with different kernel sizes were applied in order to reduce the effect of the speckles. In the same time, the effect of these filters was examined for the classification and soil moisture mapping performance. Moreover, some measures for filter evaluation (SNR, ENL) were calculated to compare those filters (Gupta & Gupta 2007). Such measures (i.e. ENL) require to be applied over a uniform area. Therefore, five area of interest (AOI) were defined to be – as much as possible - a uniform area, also to represent different land cover types (Figure 3.8).

#### Signal-to-Noise Ratio (SNR)

Signal-to-Noise Ratio (SNR) is used for quantitative comparison.

$$SNR = 10\log_{10} \left( \frac{\sum_{i=0}^{N-1} u_i^2}{\sum_{i=0}^{N-1} (u_i - v_i)^2} \right) \quad (3.10)$$

where  $N$  is the total number of pixels,  $u_i$  is the de-noised image, and  $v_i$  is the original image (Gupta & Gupta 2007).

### Equivalent Number of Looks (ENL)

The ENL measures the speckle level in a SAR image over a uniform image region. A large value of ENL reflects better quantitative performance of the filter. The value of ENL depends on the size of the tested region (Gupta & Gupta 2007).

$$ENL = \frac{\mu^2}{\sigma^2} \tag{3.11}$$

where  $\mu$  and  $\sigma$  are mean value and variance, respectively.

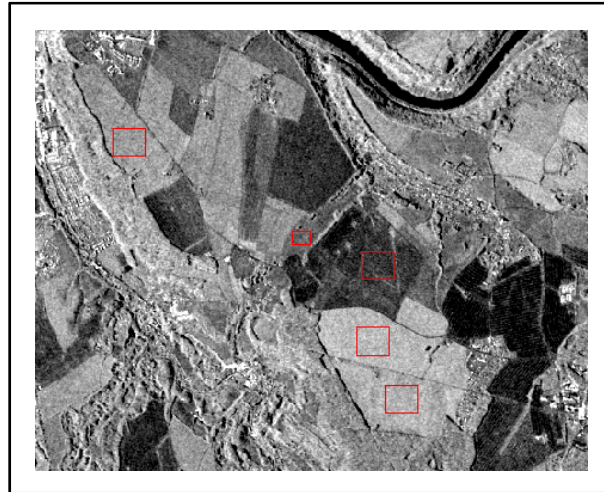


Figure 3.8. Selected AOIs (red polygons) for SNR and ENL calculations.

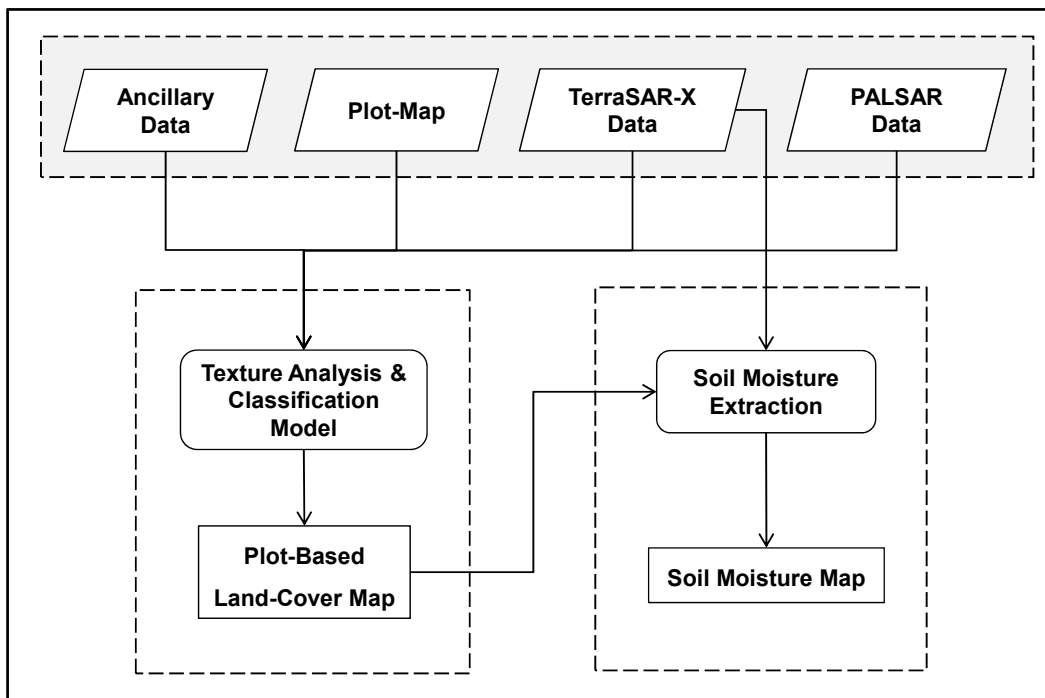


Figure 3.9. General scheme showing the applied approach. For details see Figures 4.2, 5.4, 6.1, 7.2.

## **4 Plot-Based Multi-Direction /-Distance Texture Analysis Model for Agricultural Land Cover Classification Using SAR Data**

### **I. Texture Analysis Module**

#### **4.1 Introduction**

This Section reports on a model of multi-distance and multi-direction texture analysis on SAR data and its use for agricultural land cover classification. The model developed by the author has been built using VB.NET in ESRI ArcGIS software as an embedded software extension. Sets of texture measures, calculated on a plot basis and stored in an attribute table, can be compiled and evaluated by separability values. A sufficient separability as a pre-condition for successful classification has been tested for a typical Mid-European agricultural and horticultural land use pattern around the town of Pirna (Saxony/Germany) which had been mapped in the field before. An optimised subset of indicative textural features could be identified. It forms the basis for an efficient and fast classification. The classification steps, methods and parameters are user-controlled selection.

High-resolution SAR data, TerraSAR-X (TSX) strip mode images from 31 May and 17 June of 2010 and an ALOS/PALSAR (dual polarisation) scene from 31 May of 2010 were used for the development and following performance tests of the model. This Section will concentrate only on the texture analysis model. Calculation starts with texture features which are assigned to pre-existing agricultural plot polygons, followed by a performance assessment of all features. The strongest performers are isolated using training data and then calculated for all parcels.

#### **4.2 Land Cover Classification Using SAR Data**

##### **4.2.1 General Objectives**

Land cover change can be studied at various spatial and temporal scales. In the following a methodology of topic large-scale land use monitoring is presented. Detailed knowledge on land use is demanded by numerous disciplines: spatial

planning is concerned about high “losses” of land for technical and residential developments, ecology about implications on habitats and genetic diversity, meteorology and hydrology about boundary layer effects of changing land cover such as evaporation, ground-water formation or surface run-off. National geo-database specifications have only recently reacted by providing contiguous land use information as an integral part, as e.g. mirrored by the “Real Land Use” category of the German reference geo-data basis (Schauer 2010). Due to a universal demand of such data, their class schemes remain coarse and show no or little differentiation within farm land. In this respect the widely-used European land cover database CORINE performs more specific. A standardised large-area data set, however, cannot carry information on a plot basis. CORINE concentrates on generalised land use patterns with update cycles of 6 years and more (Keil *et al.* 2010).

Mapping and identifying land cover and its change is perhaps the most important as well as the best investigated topic in remote sensing (Liang 2008; Soergel 2010). SAR data are almost independent from weather conditions. Nearly every data take of a SAR sensor can theoretically find entrance into monitoring. A time filter can be adapted to the best-possible differentiation of agricultural plants within their phenological cycles. Moreover, multi-temporal monitoring can reveal seasonally changing conditions of annual crops (Baghdadi *et al.* 2009; Borghys *et al.* 2006; Mróz & Mleczko 2008; Waske & Braun 2009). The 3-meter resolution of TerraSAR-X data even allows a monitoring of highly diversified and fine-grained plot patterns.

It will be shown, how an integrated model can strongly facilitate a texture analysis of SAR data using different directions and distances and result in stable classifications of agricultural land cover.

#### **4.2.2 Test Area and Imagery**

In order to get a suitable and representative study area for land cover and crop mapping, a subset of the study area was chosen (Figure 4.1, demarcating the parcels in red). The parcels in this area were divided into smaller areas according to the digital ortho-photos of the study area to increase their total number. The all parcels (with a number of 183) were used in this section for testing the model. Simultaneous to the acquisition of the SAR data the following land cover classes were mapped in the field: cereals, rape, maize, grass and orchards.

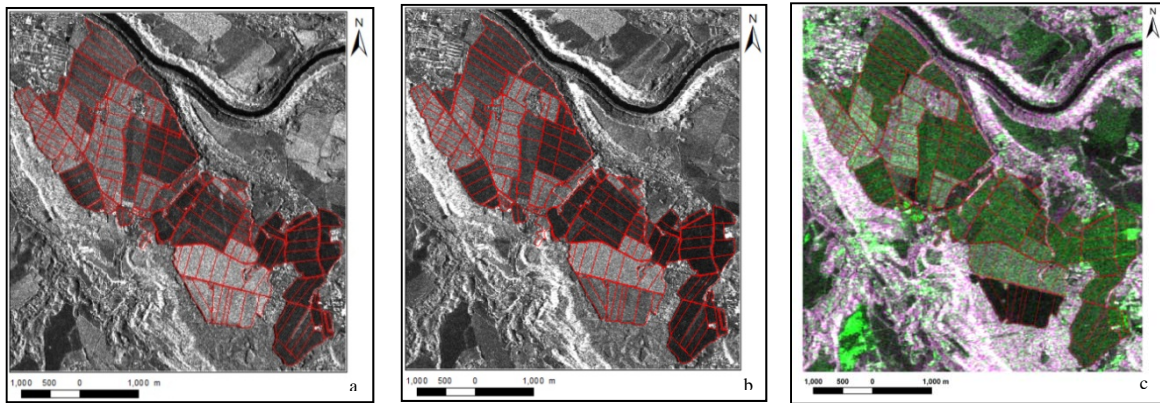


Figure 4.1. (a) TSX image acquired 31 May 2010, (b) TSX image acquired 17 June 2010 and (c) ALOS/PALSAR image (RGB: HV, HH, HV) acquired 31 May 2010. Redlines: parcel boundaries.

### 4.3 Texture Analysis

#### 4.3.1 Use of Texture

Human beings use both spectral and spatial features to decode visual signals. Spectral features describe tonal variations as such, while spatial features reflect a spatial distribution of intensities of grey-values or colours. Two kinds of spatial relationships can be defined: texture and context. Texture is seen as a specific tonal variation within a small area (Tso & Mather 2009). It refers to a spatial frequency of change and the arrangement of shades (tones) (Weng 2010). Context may be briefly described as the topology between different image objects, no matter if already semantically tagged or just appearing as a delimited pixel cluster of specific tonal or textural properties. Contextual information assists object identification by its specific setting within a neighbourhood. In many cases texture proves to be more informative than tonal information. This has encouraged the development of numeric texture measures for use in remote sensing and other image detection techniques (Tso & Mather 2009).

Texture is used in low-level image analysis (Gupta, Mangai & Das 2008) for the identification of objects or regions of interest (Haralick, Shanmuga & Dinstein 1973; Liang 2008; Tso & Mather 2009). Combinations of texture and spectral features are a key to improvements in classification accuracy. As the spatial resolution of remotely sensed data is steadily increasing, the importance of image texture does the same

(Coburn & Roberts 2004). Objects of interest mostly form pixel clusters within images of a ground resolutions of one meter and better, while at the same time spectral properties of individual pixels become less predictable and indicative (Coburn & Roberts 2004; Ouma, Ngigi & Tateishi 2006). Consequently, texture information is often inevitable for a successful classification (Blaschke, Lang & Hay 2008; Buchroithner 1993; Coburn & Roberts 2004; Kayitakire, Hamel & Defourny 2006). This has been demonstrated with image data of various sensors like IKONOS (Kayitakire, Hamel & Defourny 2006), SPOT (Lewinski & Bochenek 2009), SAR (Kuplich 2006; Zhang, Wu & Wei 2009) and InSAR data for mountainous areas mapping (Damoiseaux 2003). The value of textural information depends on the spatial resolution of the image in relation to the coarseness of the land cover (Coburn & Roberts 2004; Ouma, Ngigi & Tateishi 2006). Where the image resolution is fine relative to the frequency of real-world surface variation, texture forms a valuable classification source. Conversely, where homogeneous regions are small in the image and do not portray object changes due to severe under-sampling, texture will not be indicative (Tso & Mather 2009).

#### **4.3.2 Systematisation of Textural Features**

An operational definition of texture features is difficult. Texture recognition approaches have been grouped as a result of different underlying theories. The concept defines features of the Fourier power spectrum by frequency domain filtering. The second one is based on neighbourhood (focal) statistics which are thought to be related to texture, for example a standard deviation. A third approach uses the joint grey-level probability density (Haralick, Shanmuga & Dinstein 1973). Another one makes use of an image model on the basis of structural assumptions such as the existence of fractal properties or compliance to the random-field model such as the multiplicative autoregressive random field (Tso & Mather 2009).

Alternately, all textural measures can be characterised depending on whether they stem from the original image, or from transformations of the original (like a grey-level co-occurrence matrix or a wavelet-decomposed image). The first group is termed first-order; the latter one is second-order textural measures. Whatever the approach might be, textural measures should be applicable to both classified and unclassified images (Liang 2008).

The present work concentrates on statistical operators for texture description. Within the group of first-order statistics we find simple measures like average, standard deviation, mode or variance. More sophisticated calculations reveal properties of secondary image features and include, for instance, the texture spectrum and frequency-based contextual classifiers. Other second-order statistics seek to characterise the distribution of pixel values over a fixed space by describing grey value dependencies of pixel subsets. Here, the most popular method starts from a grey-level co-occurrence matrix (GLCM) and calculates a number of properties relating to pair-wise defined relationships of pixels (Coburn & Roberts 2004). This solution has been chosen in the project.

#### **4.3.3 Texture and Scale**

Scale and scale-related uncertainty is a difficult problem and increasingly also a topic of research. Strategies have to be developed to account for scale effects. Two principal approaches have been suggested (Lam *et al.* 2004): The first one tries to define indicative scale ranges for an observation of specific phenomena. A second approach aims at multi-scale assessment, meaning to perform the same analysis over multiple scales, in order to compare the results and to estimate uncertainty. Still a thorough benchmark study is much needed in order to examine how, within the objective of land cover classification and change detection, texture detection performs at different spatial scales and resolutions (Liang 2008). In the present study the problem has been tackled by flexible sizing of the displacement vector in the co-occurrence matrices.

#### **4.3.4 Texture in Radar Imagery**

The concept of texture is essential in the exploitation of radar images: Texture is an image equivalent of surface macro-roughness. It is directly related to the dimension and average spatial organization of the elementary cells as smallest homogeneous elements. Three theoretical levels of texture analysis exist: micro, meso and macro scale. Besides well-known advantages, radar images are subject to distortion, both geometric and radiometric (speckle). Speckle, inherent to all radar images, is a micro-scale grain effect (salt-and-pepper effect), a statistical fluctuation associated with individual pixels. In fact, within a zone of many scatterers, constructive and

destructive interferences occur and shine up as light or dark tones in the image. It is mainly this phenomenon which inhibits recognition or classification on a pixel-by-pixel basis. For visualisation, speckle is a source of disturbance and should be minimised by applying digital filters. Within other applications like SAR interferometry, speckle is rather useful and must be treated differently (Gomasca 2009).

#### **4.3.5 Spatial Reference for Textural Features**

Until the mid-1990s information extraction from remotely sensed imagery was mainly using statistical techniques applied to features of individual pixels. The ability of these traditional methods for resolving interclass confusion is limited. As a result, alternatives have been proposed. They proposed new classifiers as well as alternative sets of input data, such as texture data (cf. above) and/or a-priori spatial knowledge like a spatial segmentation of the study area. Such an additional layer defines spatial reference objects as recipients of any later calculated image properties. The object extent is known, but its state is unknown prior to classification. Such a strategy is in particular suitable for areas with sharp boundaries (e.g. an agricultural plot mosaic). It will perform robust in terms of an adverse influence of boundary pixels, which normally degrades a classification. When combined to an image, each spatial object (e.g. plot) can then be characterised by zonal statistics (be it a mean spectral signature or a textural measure), and will thus be represented by one unique vector in the feature space (Tso & Olsen 2005; Wang & Wang 2004). Moreover, per-plot classification provides an elegant solution for eliminating internal spectral variability and mixed pixel effects (De Wit & Clevers 2004).

### **4.4 The Concept of the Model**

#### **4.4.1 Modules**

The developed software solution offers several functionalities for a complex processing task. From the user's point of view it comprises the following sequence of analytical steps:

- Data import
- Calculation of textural features for all training areas
- Definition of a best-performing feature subset as derived from the reference plots by separability matrices

- Global calculation of the best texture features and storage in the feature attribute table
- Per-plot classification of land cover by means of the feature space as defined in the previous step
- Data visualisation.

Both, all built-in functions and the associated user interfaces have to be well structured in order to arrive at a software product which can be handled, maintained, and updated in a convenient way.

Processing starts at data import, and applies to the geo-referenced imagery and ancillary vector data. The vector input is plot polygons and land-use training data, the first ones defining spatial units for the feature calculation, the latter ones for an optimised feature selection and for the training of the classifier (in the classification module; Section 5).

A first central task-specific module is dedicated to texture calculation. Every run generates series of grey-level co-occurrence matrices from an (optionally) re-scaled image. Re-scaling compresses the grey value range. The matrix size automatically adjusts to the quantisation level, and the number of matrices to the number of parcels. In addition to mean and standard deviation, ten parameters are extracted from the GLCM and stored in the attribute tables of the parcels. Various distances and orientations for the GLCM can be invoked and can thus optionally greatly enlarge the available feature space.

The calculation of separability forms the subsequent step. For the determination of separability the Jeffries-Matusita Distance has been implemented. The separability values are based on the computed features of the training areas, in our case plots with a known land use. On the basis of the separability matrix a selection of potentially best-performing features can be carried out. All these steps can be run in a batch mode for different directions and distances combinations, resulted in a collective representation of the output separability matrices. The separability values are sorted in a descending way with relative batch number. Subsequently the texture feature calculation is invoked for all image cells corresponding to the plots of the study area. Technically this implies another run of the feature extraction module with an adjusted reduced parameter set.

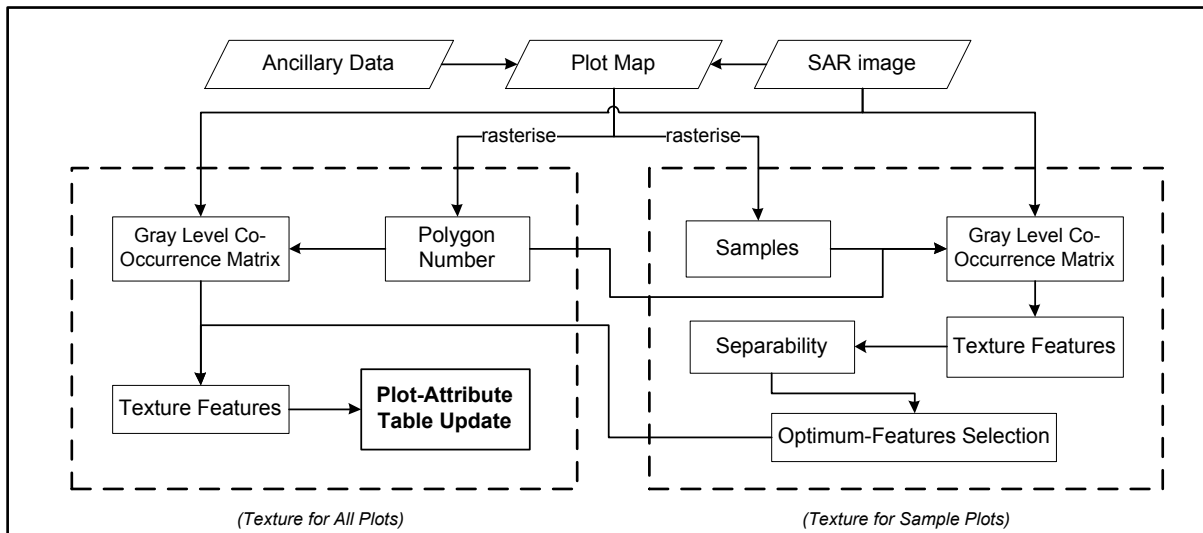


Figure 4.2. Methodological flowchart.

Finally, the classification module comes into the game. It exploits the entries of the feature attribute tables and assigns a code of class membership to each plot polygon. Graphically the classification result can quickly be assessed since the class code is visualised in the graphic data window in associative colour codes. Figure 4.2 shows the methodological flow chart applied in this study.

#### 4.4.2 GIS Integration

The strength of GIS lies in its potential to provide a comprehensive database and analytical capabilities to be applied to a wide range of geo-referenced data sets, including those obtained by means of digital image analysis. Databases need frequent updates (Gao 2009), land use/cover is a prominent example. While land use often remains quite static on a highly generalised observation level, as in case of a coarse classification into agricultural, forested, built-up areas and water bodies, land cover change becomes an extremely dynamic process if we look more closely, for example at the crops cultivated and their status on a plot basis. With the principal objective of agricultural monitoring in mind, the benefits of using a GIS as data management and analysis platform become obvious: Database updates can be assisted by provision of specialised image analysis tools. Aerial photographs, satellite images and all digital maps can be activated in the GIS and function as a part of the analysis or as a reference to the analysis. Vector GIS data even forms an integral part of the processing within the given concept. It represents a-priori knowledge on

plot shapes and agricultural crops (training data). The process chain results in a map, which can completely be produced using built-in GIS functionality.

## 4.5 Selected Model Features in Detail

### 4.5.1 Grey-Level Co-Occurrence Matrix (GLCM)

The principal concept of a grey-level co-occurrence matrix (GLCM) is that the texture information contained in an image is expressed by the adjacency relationship of grey values. It is assumed that the texture information is specified by frequencies  $f_{ij}$  within the GLCM, where  $f_{ij}$  denotes the frequency of occurrence of a grey value pair  $i$  and  $j$  respectively, separated by a distance  $d$  in a specific direction  $\alpha$  within the image. Basically, co-occurrences can be calculated for any direction and distance (cf. Figures 4.3 and 4.4). Practically, only four directions corresponding to angles of  $0^\circ$ ,  $45^\circ$ ,  $90^\circ$ , and  $135^\circ$  are used, since they coincide with the cell topology.

Figure 4.3a represents a  $4 \times 4$  image with four grey levels. Figure 4.3b displays the general form of the corresponding GLCM. For example, the value contained in cell (2, 3) represents the number of times that grey levels 2 and 3 co-occur in a specific direction and distance. Figures 4.3c through 4.3f present the results for four directions given above with  $d = 1$ , while H, V, LD, and RD denote the angles of  $0^\circ$  (horizontal),  $90^\circ$  (vertical),  $135^\circ$  (left diagonal), and  $45^\circ$  (right diagonal), respectively. Instead of directly using the frequency values, it is common practice to normalise in a GLCM in order to avoid scaling effects (Tso & Mather 2009).

### 4.5.2 Features Derived from GLCM

Already Haralick *et al.* (1973) proposed a variety of texture measures based on the *GLCM* and termed them *textural features*. In the following text,  $p(i, j)$  denotes the  $(i, j)^{\text{th}}$  entry within a normalised *GLCM*, and  $N$  denotes number of grey levels. All suggested textural features are extracted from these grey-tone spatial-dependence matrices. One group of these measures relates to image properties such as homogeneity, contrast, and the presence of an organised structure. Another group indicates the nature of grey-value transitions. It is, however, hard to identify which verbally specified textural feature is exactly represented by each numeric feature (Tso & Mather 2009). All features measure different properties, but are nevertheless not independent of each other. The texture-feature equations are listed in Table 4.1.

The homogeneity measure indicates local uniformity. If elements concentrate on the main diagonal, its value will be high (Navulur 2007). Conversely, the contrast is high, if high frequencies occur distantly from the main diagonal. Dissimilarity indicates how far adjacent elements are located from each other intensity-wise (Navulur 2007). The measure of the ASM will output a higher value when co-occurrence frequencies  $p(i, j)$  concentrate at few spots in the GLCM. If the  $p(i, j)$  entries are dominantly close to each other, then ASM will generate a small value. High ASM values indicate textural homogeneity, low values indicate heterogeneity (Tso & Mather 2009).

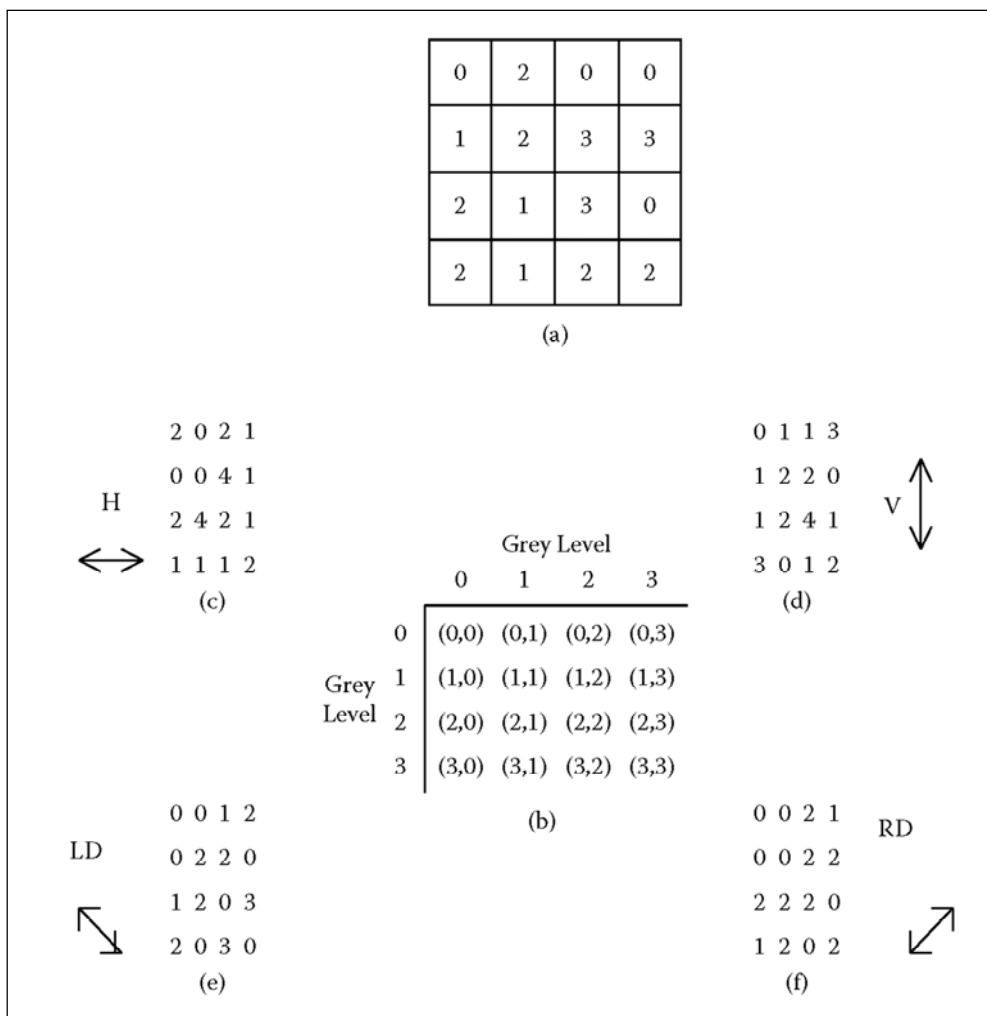


Figure 4.3. (a) A 4 x 4 image with four grey levels. (b) General form of GLCM with grey levels 0–3. The value in cell (i, j) stands for the number of times grey levels i and j occur with a specific direction and distance d. (c)–(f) present the results with respect to the four principal directions 0°, 90°, 135°, and 45° degrees, and d = 1 (from Tso & Mather, 2009).

Table 4.1. Texture Features on the basis of a GLCM (after Haralick *et al.* 1973).

Homogeneity	$\text{Homo.} = \sum_{i,j=0}^{N-1} \frac{P_{i,j}}{1 + (i - j)^2}$
Contrast	$\text{Con.} = \sum_{i,j=0}^{N-1} P_{i,j} (i - j)^2$
Dissimilarity	$\text{Diss.} = \sum_{i,j=0}^{N-1} P_{i,j}  i - j $
Angular Second Moment (ASM)	$\text{ASM} = \sum_{i,j=0}^{N-1} [P(i,j)]^2$
Energy	$\text{Energy} = \sqrt{\text{ASM}}$
Entropy	$\text{Entropy} = \sum_{i,j=0}^{N-1} P_{i,j} (-\ln P_{i,j})$
GLCM Mean	$\mu_i = \sum_{i,j=0}^{N-1} i (P_{i,j}) \qquad \mu_j = \sum_{i,j=0}^{N-1} j (P_{i,j})$
GLCM Variance	$\sigma_i^2 = \sum_{i,j=0}^{N-1} P_{i,j} (i - \mu_i)^2 \qquad \sigma_j^2 = \sum_{i,j=0}^{N-1} P_{i,j} (j - \mu_j)^2$
GLCM Standard Deviation	$\sigma_i = \sqrt{\sigma_i^2} \qquad \sigma_j = \sqrt{\sigma_j^2}$
GLCM Correlation	$\text{GLCM Corr.} = \sum_{i,j=0}^{N-1} P_{i,j} \left[ \frac{(i - \mu_i)(i - \mu_j)}{\sqrt{(\sigma_i^2)(\sigma_j^2)}} \right]$

In comparing energy and ASM, the first measure reacts on the extent of pixel pair repetitions; and the second one on the pixel orderliness (Navulur 2007). The entropy measure outputs a high value for a very even distribution of entries of  $p(i, j)$  to the GLCM, and a low one for sharp peaks within the matrix (Tso & Mather 2009). Entropy is a measure of randomness, and it will be at maximum when all the elements of C are equal (Navulur 2007).

Despite of a frequent use, there are disadvantages of grey-level co-occurrence matrices. There exists no established method for determining an optimum dimension of a displacement vector  $d$  and the angle  $\alpha$ , which together define the partner cells to be compared. Second, a large number of properties can be computed from the co-occurrence matrices which, consequently, requires an intelligent feature selection approach in the follow-on steps (Rahul 2008; Weng 2010). Third, each co-occurrence matrix must be computed for a spatially fixed group of pixels or objects. The result will be scale-dependent, since the analysis window determines what features will be highlighted (Lam *et al.* 2004).

### 4.5.3 Calculation of Separability

Separability for each class-pair of land cover types was quantified in two steps: the Jeffries-Matusita Distance  $J$  (Equation 2) was calculated using the Bhattacharya Distance  $B$  (Equation 1) as an intermediate result (Nussbaum & Menz 2008). Then the threshold  $T$  for each pair of the classes was calculated using the Equation 3.

$$B = \frac{1}{8} (m_1 - m_2)^2 \frac{2}{\sigma_1^2 + \sigma_2^2} + \frac{1}{2} \ln \left[ \frac{\sigma_1^2 + \sigma_2^2}{2 \sigma_1 \sigma_2} \right] \quad (1)$$

$$J = 2 (1 - e^{-B}) \quad (2)$$

$$x_{1(2)} = \frac{m_2 \sigma_1^2 - m_1 \sigma_2^2 \pm \sigma_1 \sigma_2 \sqrt{(m_1 - m_2)^2 + 2A(\sigma_1^2 - \sigma_2^2)}}{(\sigma_1^2 - \sigma_2^2)} \quad (3)$$

$$A = \log \left[ \frac{\sigma_1}{\sigma_2} * \frac{n_2}{n_1} \right] \quad (4)$$

The values of  $J$  range from 0 to 2.00 and are commonly divided into 4 classes according to the following assumptions (Mróz & Mleczo 2008):

- $0 < J \leq 1.0$  : very bad separability: classes have to be redefined
- $1.0 < J \leq 1.8$  : bad separability: classes rather have to be merged
- $1.8 < J \leq 1.9$  : good separability: good results can be expected
- $1.9 < J \leq 2.0$  : very good separability: perfect results can be expected.

## 4.6 Implementation

The present model has been implemented as an add-in to ESRI ArcGIS software. A toolbox allowing any user interaction to the added functionality can be opened. It makes use of the extensive programming interface of ArcGIS: The ArcObjects libraries. They give access to the complete built-in program functionality via COM classes and a COM-compatible programming language. As programming environment VB.NET has been chosen to build this model. Main programming tasks have been dedicated to the GLCM calculation on a polygon-feature basis (plots) and the derivation of the ten texture measures including the assignment of their values to the plot-attribute table. Moreover, the program extracts and displays the separability measures, in order to assist the user in successful texture-feature choice. Moreover, the above mentioned calculations can be run in a batch mode. Figure 4.4 shows the user interface generated for these tasks.

The proposed interface was designed to provide different capabilities for more flexible interaction according to the available data characteristics. This can be described as follow:

- 1- The model can be run one time for specific combination, either for one class-pair or for all classes
- 2- The processed parcels can be divided into subgroups in case of the large parcels number that exceeds the computer processing capacity.
- 3- For the available dimensions and distances, all possible combination can be selected.
- 4- The pixel-value range for the GLCM calculation can be adjusted according to the data used. Therefore, the very low values (i.e. close to zero) or the very high values can be excluded if required.
- 5- Separability value is calculated for selected features for quick review. While the statistics and thresholds are displayed, as in Figure 4.5, for selected class-pair. Figure 3.6 shows the output separability matrix for all class combinations.
- 6- The “copy” button copies the separability values of the selected class-pair to the clipboard (i.e. can be pasted in a text file) which can be used for further analysis.

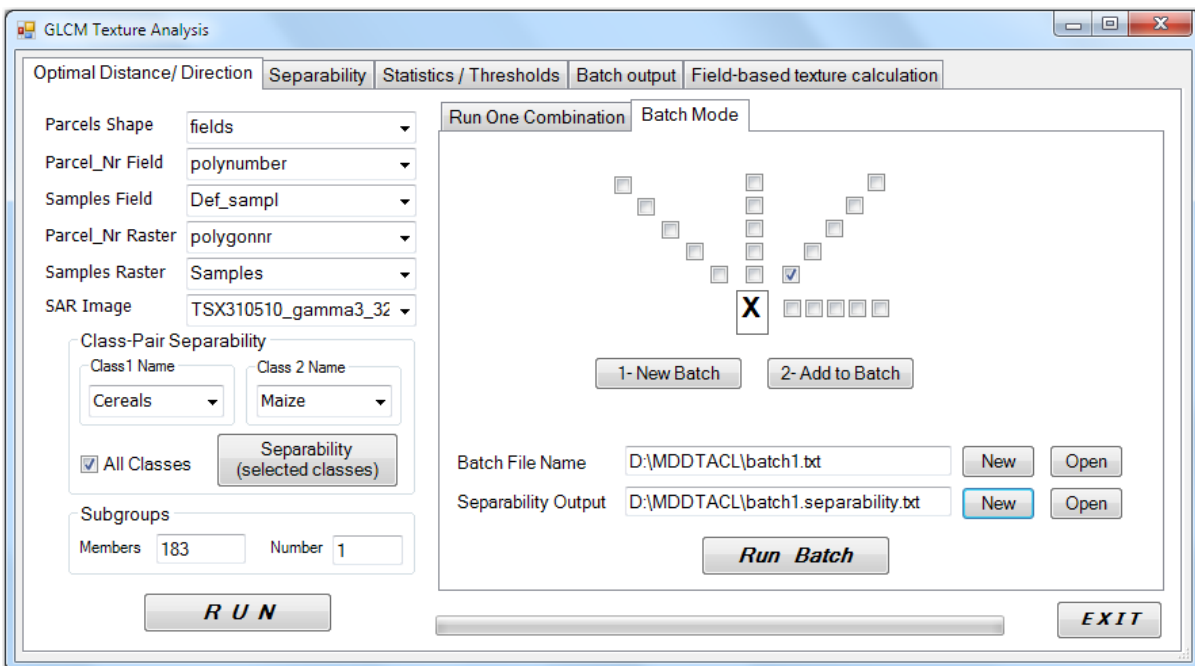
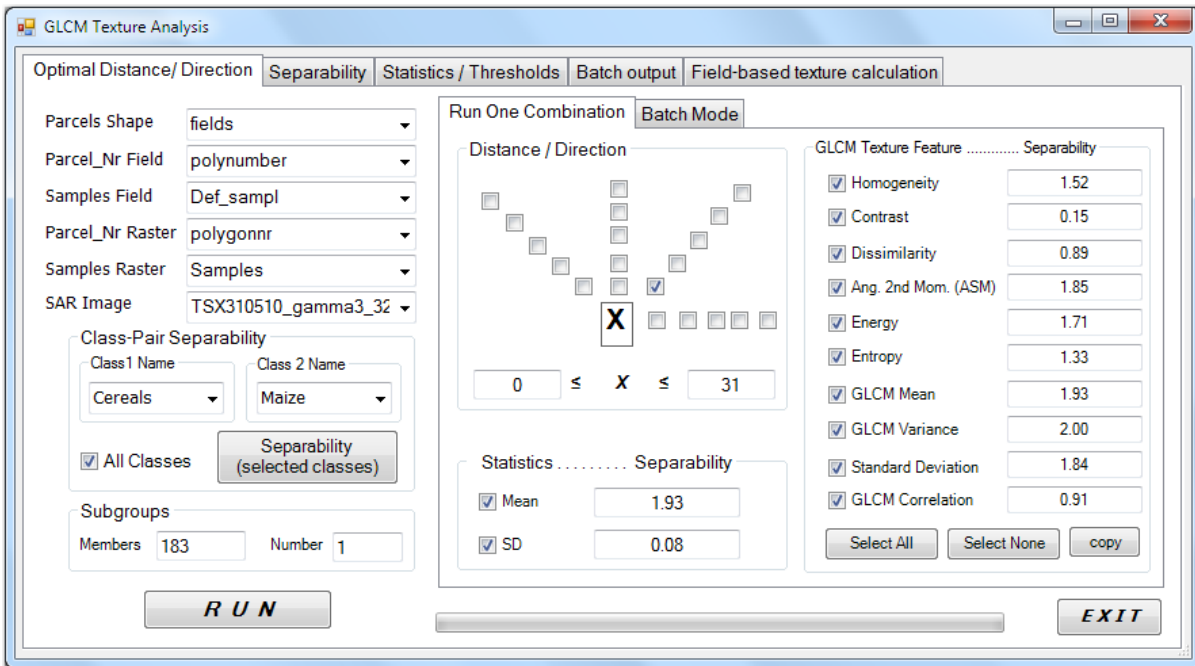


Figure 4.4. User interface for texture and separability calculation (top: one run, down: batch mode).

- 7- The batch mode is designed to save different combinations of distances and directions in a batch file to be run in a batch mode. Then both batch file and the separability matrices are saved as text files.
- 8- Figure 4.7 shows the output of the batch process, where all separability matrices are listed. The separability values are sorted in a descending order followed by the combination-number in the batch file. Therefore, the best separability values can be easily defined and the corresponding combination.
- 9- The final step is to run the model for all parcels using the best defined texture features from the previous steps. In this case the model can be run for one direction/distance combination (Figure 4.8) or in a batch mode (Figure 4.9) using the required combinations and corresponding field-name to be saved in the parcels attribute-table.

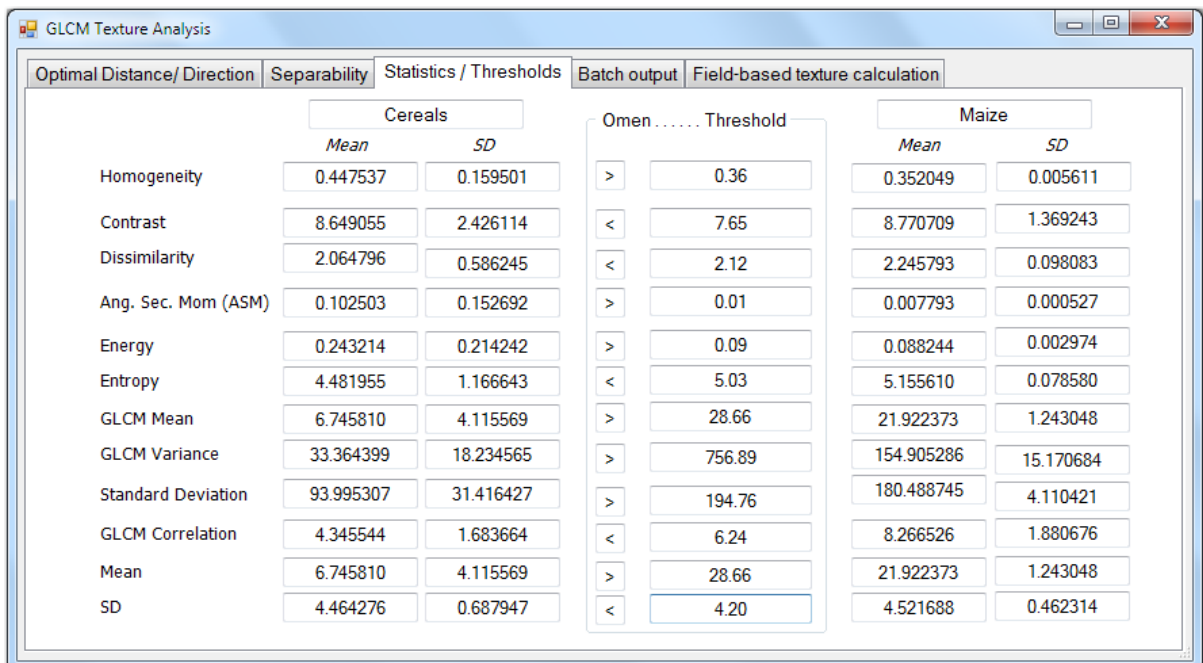


Figure 4.5. User interface showing the statistics and threshold output of one class-pair.

class1	class2	Mean	SD	Homo	Diss.	Cont.	Ang.	Energy	Entropy	GM	GV	GSD
Cereals	Maize	1.93	0.08	1.52	0.15	0.89	1.85	1.71	1.33	1.93	2	1.84
Cereals	Rape	1.93	0.21	1.28	0.36	0.83	1.84	1.69	1.21	1.93	1.99	1.6
Cereals	Grass	0.81	0.13	1.3	0.45	0.9	1.81	1.63	1.14	0.81	0.51	0.28
Grass	Maize	2	0.17	0.64	0.14	0.23	0.82	0.84	0.76	2	2	1.86
Grass	Rape	2	0.59	0	0.01	0.01	0.67	0.69	0.57	2	2	1.52
Orchards	Maize	1.42	0.44	0.65	0.02	0.1	0.01	0.01	0.03	1.42	1.58	1.77
Orchards	Grass	1.98	0.86	0	0.07	0.03	0.69	0.7	0.66	1.98	1.94	1.08
Orchards	Cereals	1.77	0.47	1.31	0.24	0.82	1.84	1.7	1.34	1.77	1.89	1.38
Orchards	Rape	1.38	0.1	0	0.04	0.01	0	0	0.08	1.38	1.4	0.96
Rape	Maize	0	0.23	0.63	0.08	0.19	0.01	0.02	0.05	0	0.02	0.6

Figure 4.6. User interface for separability output for one run.

class1	class2	Mean	SD	Homo.	Diss.	Cont.	Ang.
Orchards	Cereals	1.77 : b4 1.77 : b3	0.47 : b2 0.47 : b1	1.39 : b4 1.38 : b3	0.6 : b4 0.39 : b3	0.93 : b3 0.82 : b2	1.84 : 1.83 :
Orchards	Grass	1.98 : b4 1.98 : b3	0.86 : b4 0.86 : b3	0.28 : b1 0.2 : b4	0.25 : b4 0.24 : b1	0.26 : b4 0.22 : b1	0.82 : 0.79 :
Orchards	Rape	1.38 : b4 1.38 : b3	0.1 : b4 0.1 : b3	0.31 : b4 0.07 : b3	0.15 : b3 0.06 : b4	0.13 : b4 0.08 : b3	0.05 : 0.03 :
Orchards	Maize	1.42 : b4 1.42 : b3	0.44 : b4 0.44 : b3	0.95 : b4 0.76 : b3	0.28 : b4 0.1 : b3	0.71 : b3 0.45 : b4	0.09 : 0.02 :
Cereals	Grass	0.81 : b4 0.81 : b3	0.13 : b4 0.13 : b3	1.45 : b1 1.37 : b4	0.54 : b1 0.5 : b4	0.94 : b1 0.91 : b3	1.82 : 1.81 :
Cereals	Rape	1.93 : b4 1.93 : b3	0.21 : b4 0.21 : b3	1.28 : b2 1.26 : b3	0.38 : b4 0.36 : b2	0.83 : b2 0.75 : b3	1.84 : 1.82 :

Figure 4.7. User interface for the output separability matrices of the batch process. Where the separability values are sorted in a descending order followed by the corresponding combination number in the batch file.

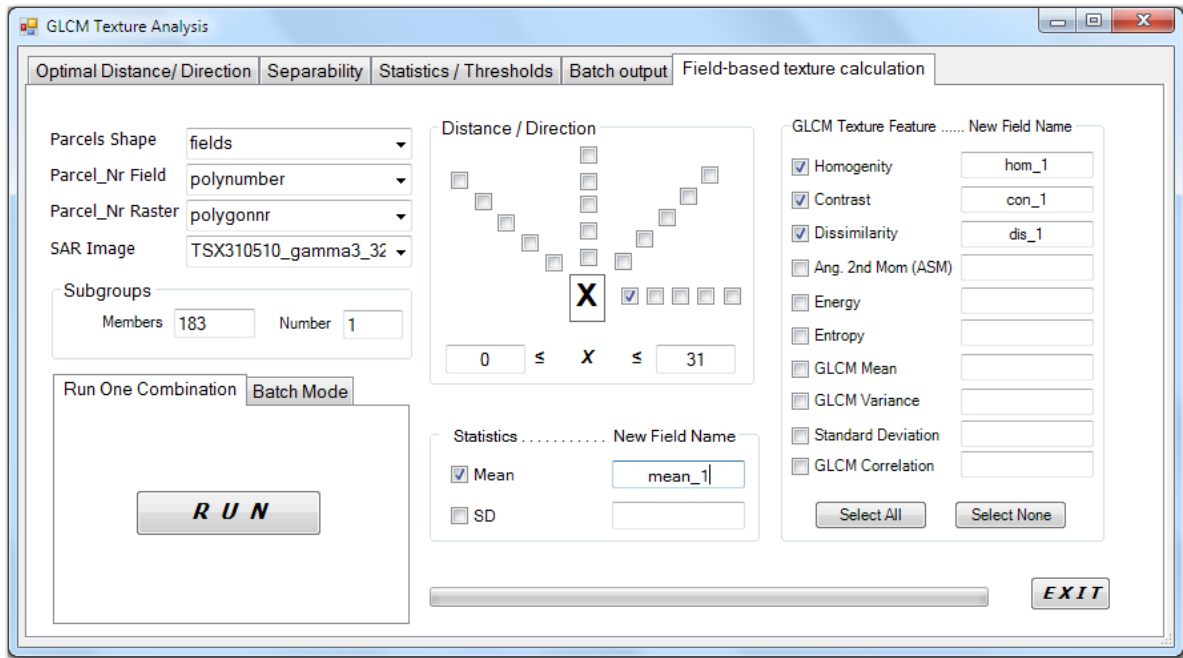


Figure 4.8. User interface for the final texture calculation step in case of a single run.

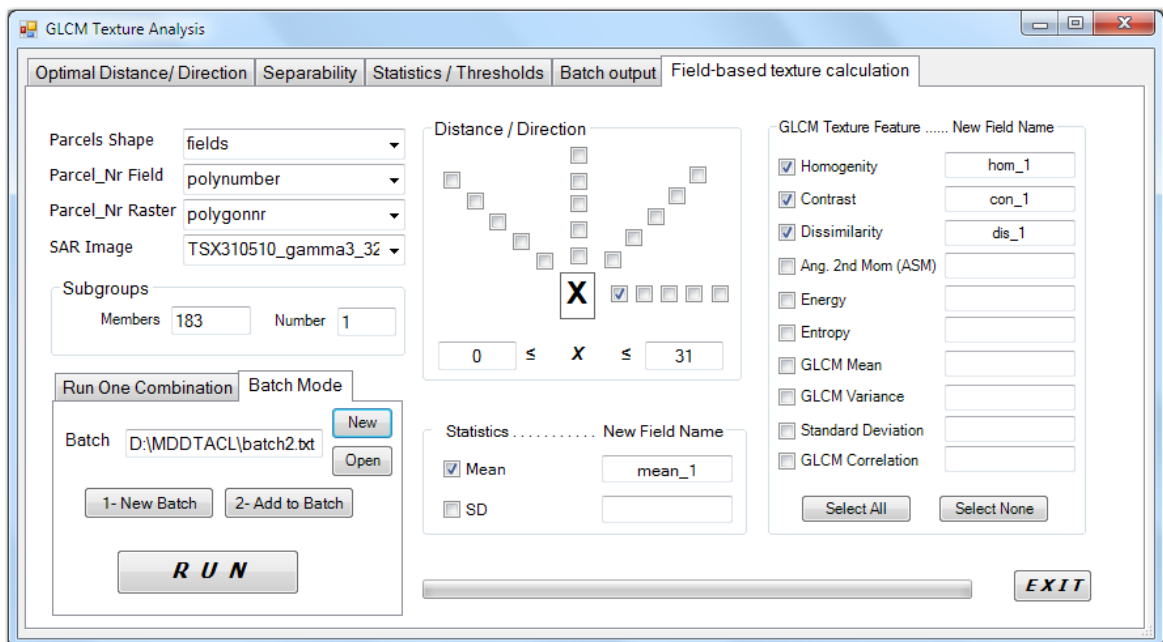


Figure 4.9. User interface for the final texture calculation step in case of a batch mode.

## 4.7 Results of the Model Application

This Section is dedicated to model functionality and texture feature extraction, comparison between different parameters used in the model, in addition to the effect of speckle filtering on the separability values. In this case, the separability is used to test and evaluate the developed model for different functionalities. In addition to the separability, the model supports different feature-selection methods. They will be discussed in Section 5 besides their performance in terms of data reduction, and classification accuracy.

### 4.7.1 Influence of Image Quantization

In order to determine the influence of image quantisation, the subset images have been rescaled to quantisation levels of 32, 64, 128, and 256. A uniform pixel distance of 1 in the 4 directions has been checked. Then, the separability values were statistically analysed with respect to varying quantisation using the ANOVA test. The results show no significant difference in separability values calculated from different grey levels in the case of TSX image and PALSAR, except for PALSAR there is only a significant difference ( $p < 0.01$ ) in the 2<sup>nd</sup> Angular Moment of HV-Band (Table 4.2). Accordingly, the user can compress the image with no significant loss of accuracy, especially in case of a large input image or a big number of parcels, in order to reduce memory space and computing time. The following results are based on a grey-value reduction to 5-bit data (32 grey-levels).

### 4.7.2 Feature Extraction

TerraSAR-X images (31/05/2011 and 17/06/2011) and ALOS PALSAR (31/05/2010) were used in order to investigate the behaviour of texture features of the predefined land cover types. The model has been used in the proposed order. First, the actual land cover classes were assigned to all plots. For this, the texture features were calculated for all plots using different distances and directions for further analysis. Then, the separability was calculated by means of the Jeffries-Matusita Distance (cf. Figure 4.4).

Table 4.2. Significant differences in the mean of separability values of image quantisation levels.

Texture Feature	Significance		
	TSX	ALOS B1	ALOS B2
Mean	1.000	1.000	1.000
Standard Deviation	0.999	0.999	0.997
Homogeneity	0.992	0.908	0.362
Contrast	1.000	0.994	0.997
Dissimilarity	1.000	0.992	0.998
Sec. Angular Moment	0.890	0.095	0.006
Energy	0.897	0.068	0.037
Entropy	0.962	0.019	0.588
GLCM Mean	1.000	1.000	1.000
GLCM Variance	1.000	1.000	1.000
GLCM Standard Deviation	0.972	0.995	0.484
GLCM Contrast	0.929	0.977	0.642

### 4.7.3 Influence of Direction

In order to investigate the effect of the direction, each direction has been combined with all distances. The distance effect can thus be minimised, while the direction effect is emphasized. Therefore, the available four directions were tested for both TSX and PALSAR data. The results showed that for some class-pairs there are no significant differences between different directions, while others showed a strong response to the direction. For TerraSAR-X images the results showed, in general, no significant effects of the direction on the separability values in the case of GLCM-Mean, GLCM-Variance and GLCM-Contrast. For PALSAR image this occurs only for GLCM-Mean and GLCM-Variance. For other texture features the direction-effect varies from one feature to another according to the class-pair.

In the TSX image (31/05/2010) the response of different class-pairs to the direction ranges from slight effects in the case of cereals-orchards and cereals-maize (Figure 4.10a and b), to significant effects like for maize-grass and maize-rape (Figure 4.10c and d). In case of the cereals-orchards and cereals-maize (Figure 4.11a and b) for the TSX image (17/06/2010) the effect was also weak, while it was significant in the

case of cereals-rape (Figure 4.11c and d). On the other hand, the HH-polarisation of the PALSAR image (31/05/2010) shows a significant response to different directions in all class-pairs; i.e. cereals-maize and maize-grass (Figure 4.12a and b). While for HV polarisation the minimum effect was found in the case of cereals-orchard, there was a significant effect in some class-pairs, i.e. grass-rape (Figure 4.12c and d). For PALSAR imagery, in general, a direction setting of 135° shows a strong response on the J values for most features.

#### **4.7.4 Influence of Distance**

To emphasize the effect of distance, each distance has been combined with all directions. Thus, the direction effect can be minimised. The available five distances were tested for both TSX and PALSAR data. The results indicate that, in general, no significant effect of the distance on the separability values of GLCM-Mean and GLCM-Variance for all SAR data and all parcel-pairs.

In the case of the TSX image (31/05/2010) the response of different class-pairs to the distance ranges from slight effects in case of cereals-orchard (Figure 4.13-a), to a significant effect for maize-grass (Figure 4.13b). For the TSX image (17/06/2010) the effect was also weak in case of orchards-grass (Figure 4.13c), while it was significant in case of cereals-grass (Figure 13d). On the other hand, for the PALSAR image (31/05/2010) the HH polarisation shows a significant response to different directions in all class-pairs, i.e. cereals-maize and maize-rape (Figure 4.14a and b). While for the HV polarisation there was almost no effect in the case of cereals-orchard, there occurred a significant effect in other class-pairs, i.e. for grass-rape (Figure 4.14c and d).

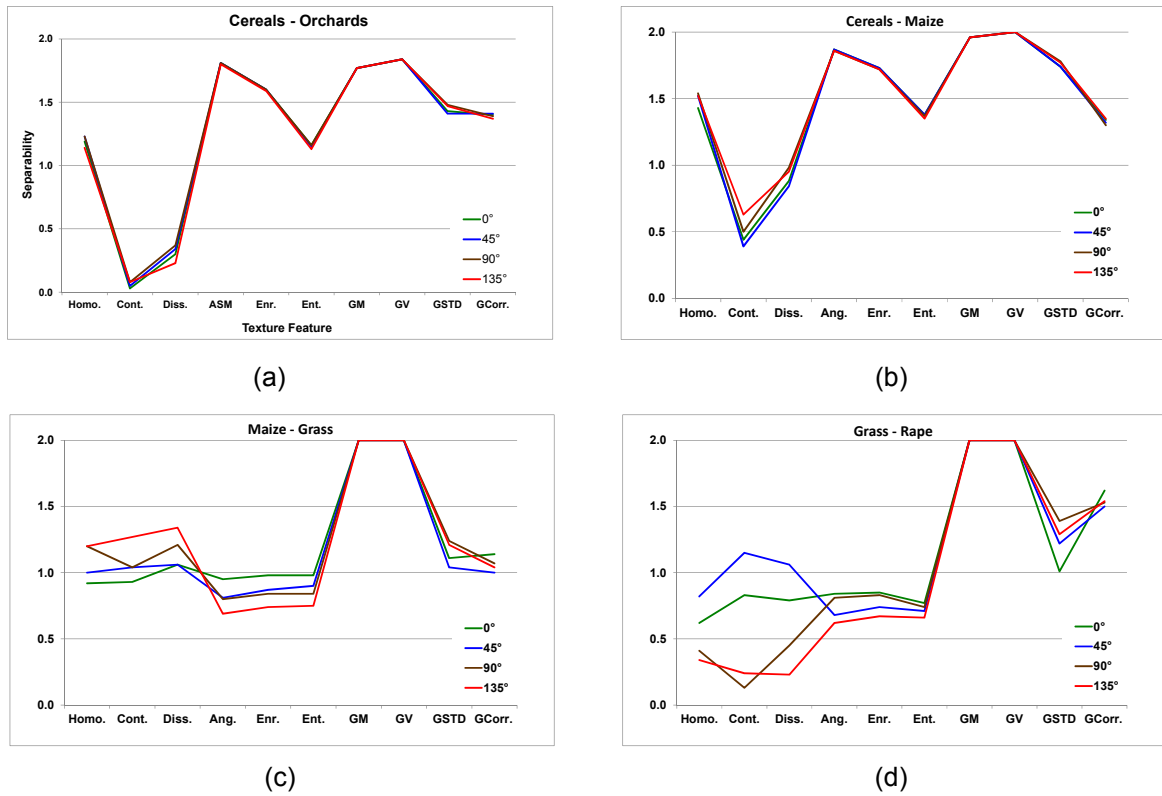


Figure 4.10: Effect of direction on separability values for TSX imagery (31/05/2010).

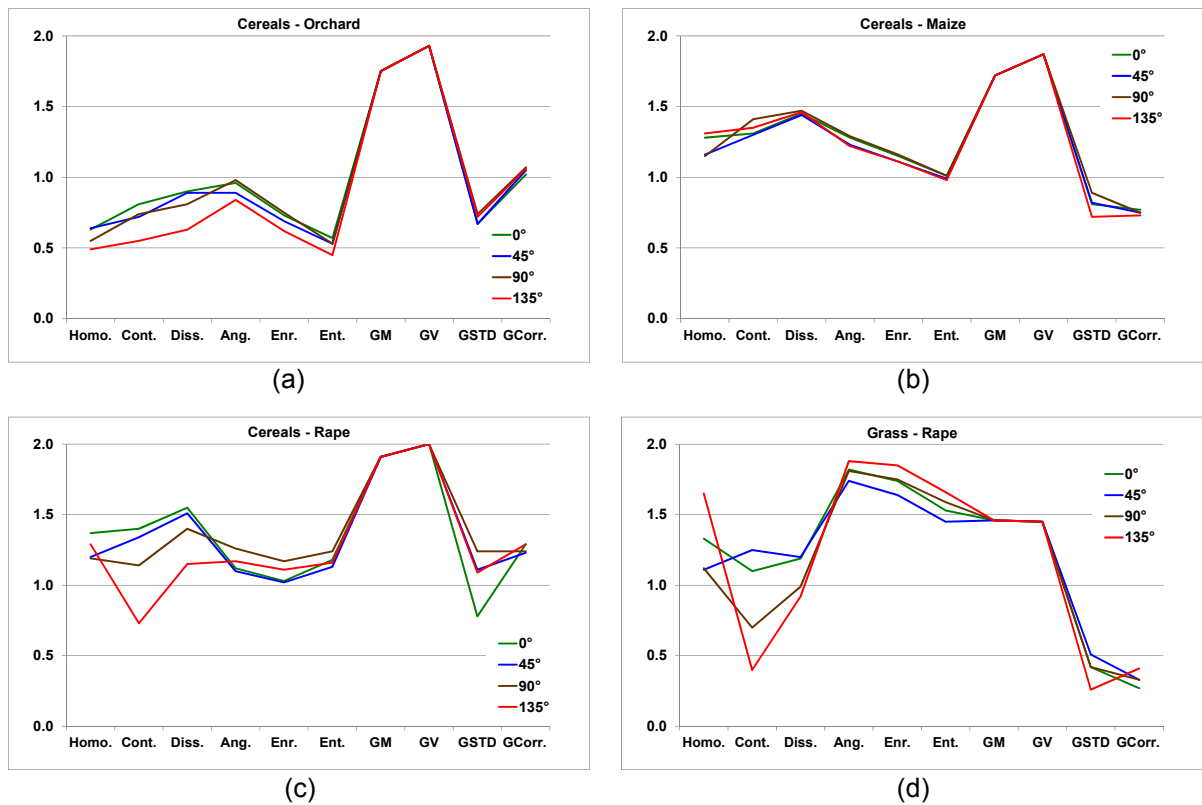


Figure 4.11: Effect of direction on separability values for TSX imagery (17/06/2010).

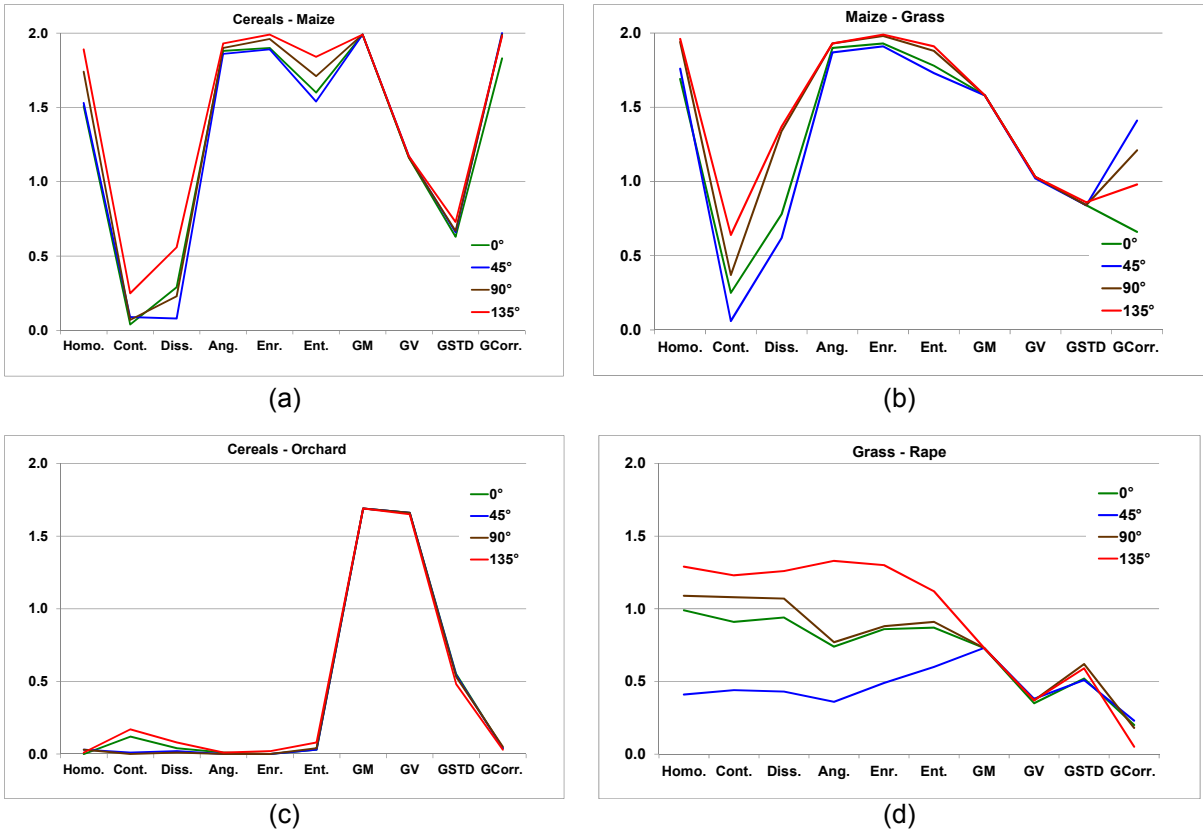


Figure 4.12: Effect of direction on separability values for ALOS imagery (31/05/2010); a, b) HH polarisation and c, d) HV polarisation.

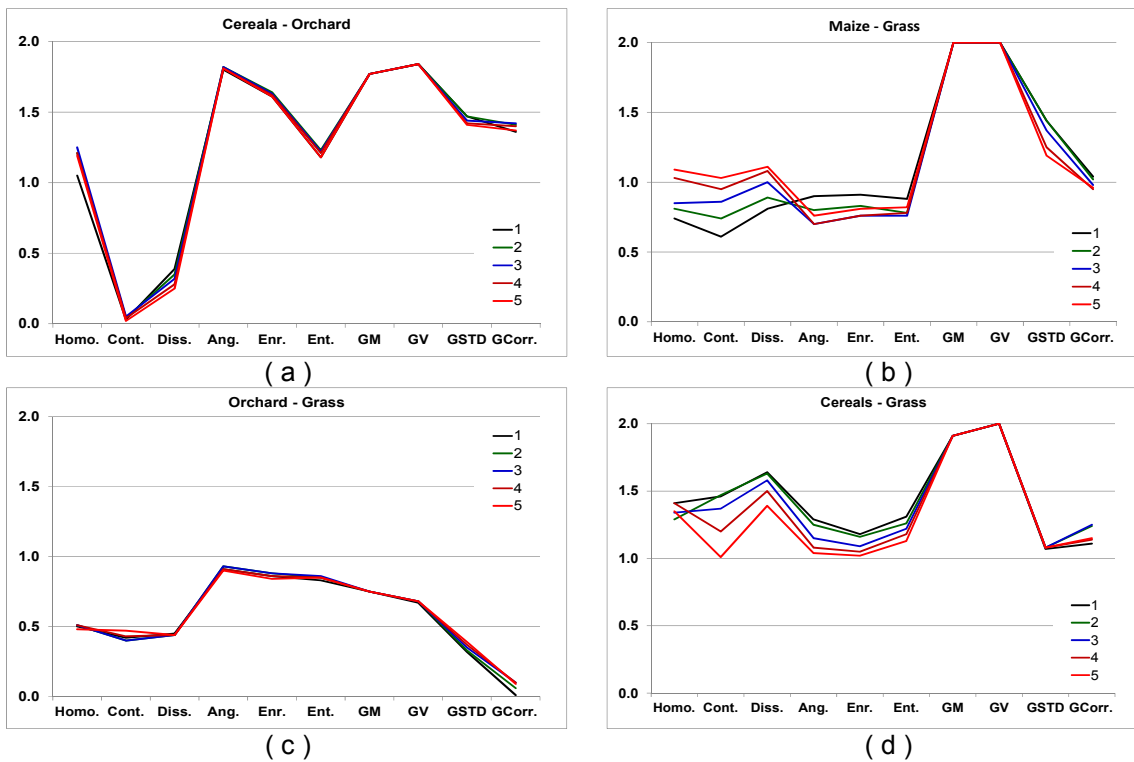


Figure 4.13: Effect of distance on separability values for TSX imagery (a, b: 13/05/2010 and c, d: 17/06/2010).

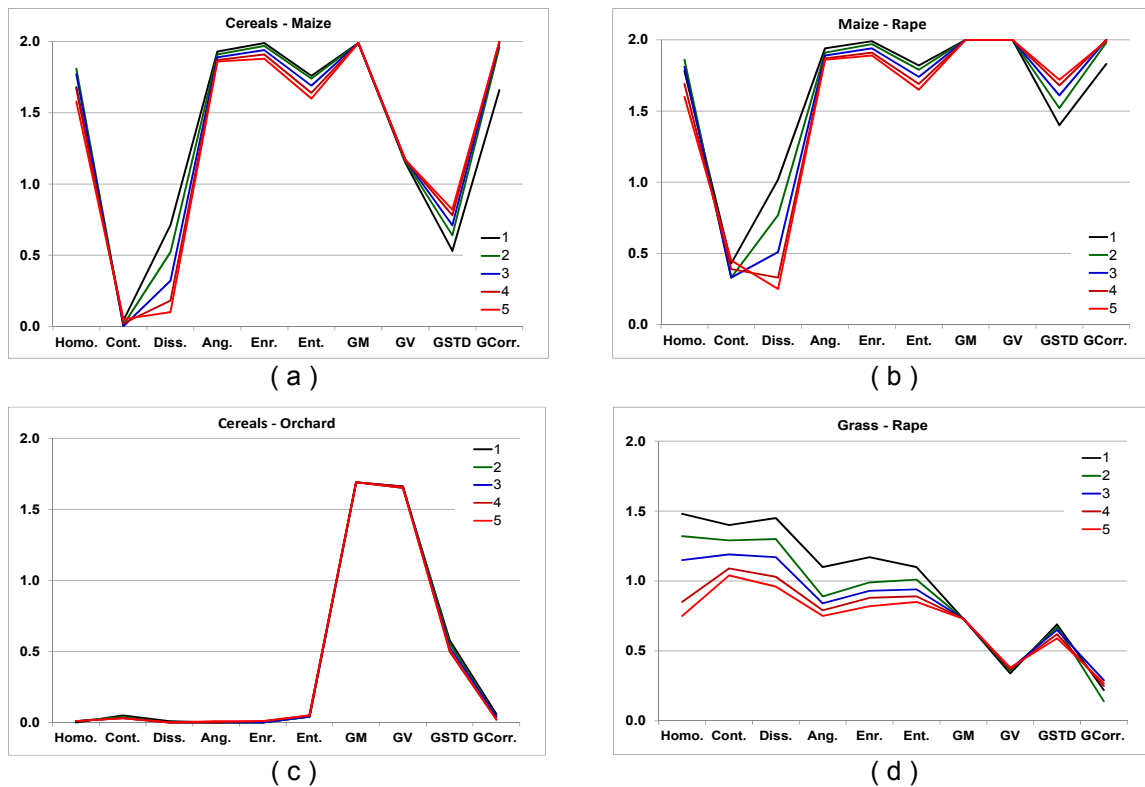


Figure 4.14: Effect of distance on separability values for ALOS imagery (31/05/2010); a, b) HH polarisation and c, d) HV polarisation

#### 4.7.5 Influence of Speckle Filtering

The effect of different speckle filters on separability values has been investigated. In this case, the distance was set to one combined with all directions, and then the separability values were calculated for the studied images. On the other hand, different signal-to-noise ratio (SNR) and equivalent number of looks (ENL) were calculated. As shown in Table 4.3, Gamma, Mean and Lee filters perform better in SNR and ENL measures. However, for some class-pairs the behaviour of these filters varies significantly in separability values. Moreover, the non-filtered TSX image achieved a higher separability value for some class-pairs. Two texture features, namely Homogeneity and Angular 2nd moment for the image from 31/05/2010 were chosen as an example to explain the variation in separability regarding to the filter type (Figure 4.15).

As shown in Figure 4.15a, the Gamma (3x3) filter improved the separability value for the cereals class-pairs, while the Median (3x3) filter improved the separability of

maize-grass. In the case of angular second moment (Figure 4.15b), the Gamma (3x3) filter improved the separability value for the cereals class-pairs, while the non-filtered image improved the separability of maize-grass and grass-rape. On the other hand, it is noticed that for most of the class-pairs (especially in the case of cereals) the kernel size of 3x3 performs better than 5x5 and 7x7. Figure 16a shows that the (5x5) kernel size performed better for maize-grass. In Figure 4.16b, the (3x3) kernel size either performs better (in most cases) or slightly lower than other kernel sizes.

It can be concluded that, the performance of different filters varies according to the land-cover type. Thus, for better separability between land-cover classes, more than one filter-type could be applied. Moreover, the results showed that, in general, the small kernel-size performs better than the larger ones. This can be attributed to the effect of the large kernel-size on speckle reduction and consequently to reducing the texture variation in the image.

Table 4.3. Signal-To-Noise Ratio and ENL for different filters of TSX 31/05/2010.

<b>Filter</b>	<b>Kernel size</b>	<b>SNR</b>	<b>ENL</b>
<b>Adaptive Median</b>	3x3	26.71	35.68
	5x5	21.25	54.38
	7x7	19.09	76.97
<b>Frost</b>	3x3	23.19	44.43
	5x5	19.59	67.06
	7x7	17.78	98.61
<b>Lee</b>	3x3	21.65	51.21
	5x5	17.40	93.83
	7x7	15.91	150.64
<b>Local Region</b>	3x3	18.80	33.24
	5x5	15.51	47.38
	7x7	14.38	68.40
<b>Mean</b>	3x3	21.50	51.90
	5x5	17.12	96.63
	7x7	15.60	155.27
<b>Median</b>	3x3	21.77	45.33
	5x5	17.19	82.39
	7x7	15.58	129.30
<b>Local Sigma</b>	3x3	27.12	30.40
	5x5	25.68	36.90
	7x7	25.00	41.13
<b>Gamma</b>	3x3	21.50	51.90
	5x5	17.12	96.63
	7x7	15.60	155.27

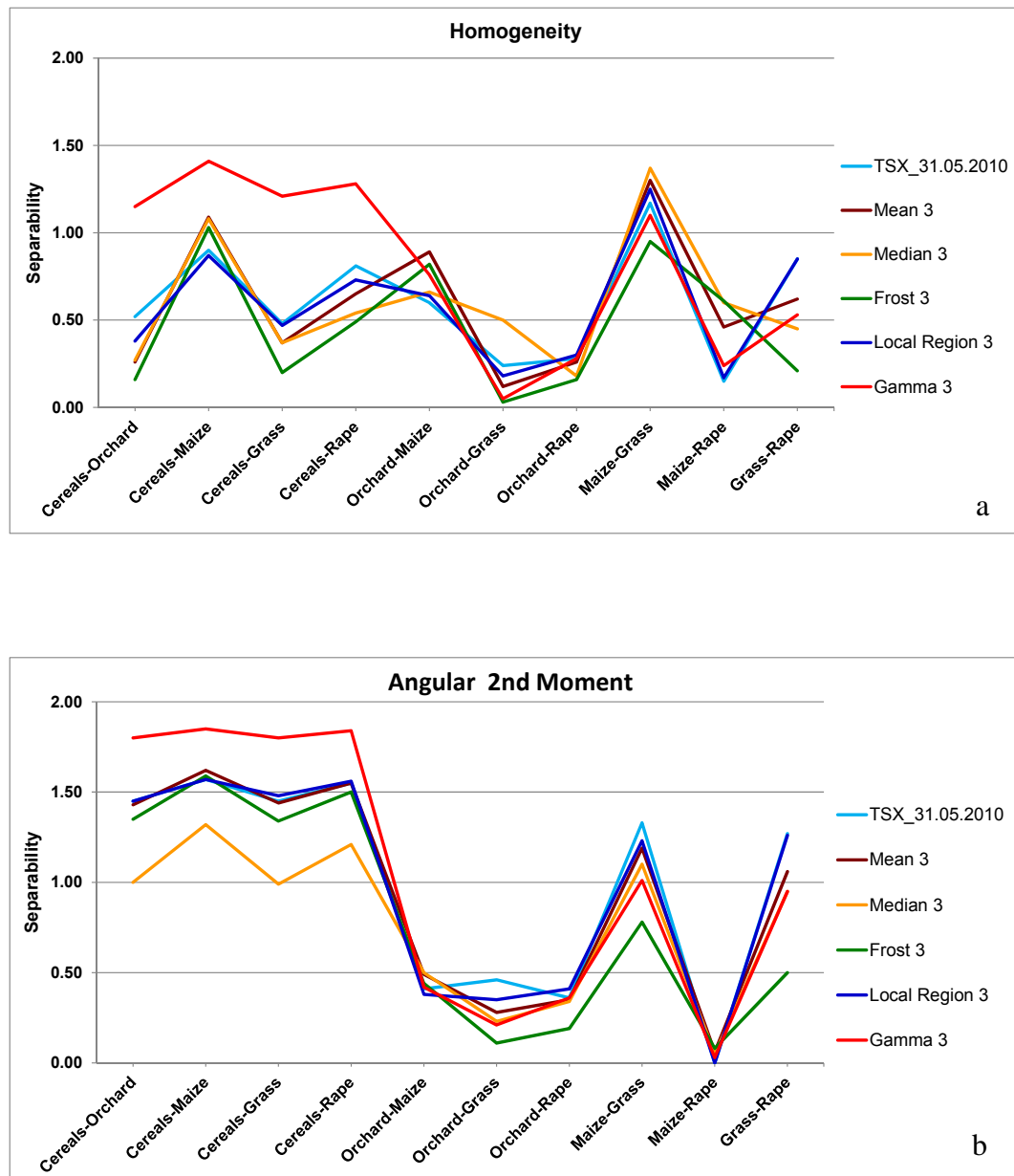


Figure 4.15. Effect of filter type on separability values for TSX imagery of 31/05/2010. a) homogeneity, and b) angular 2<sup>nd</sup> moment texture features.

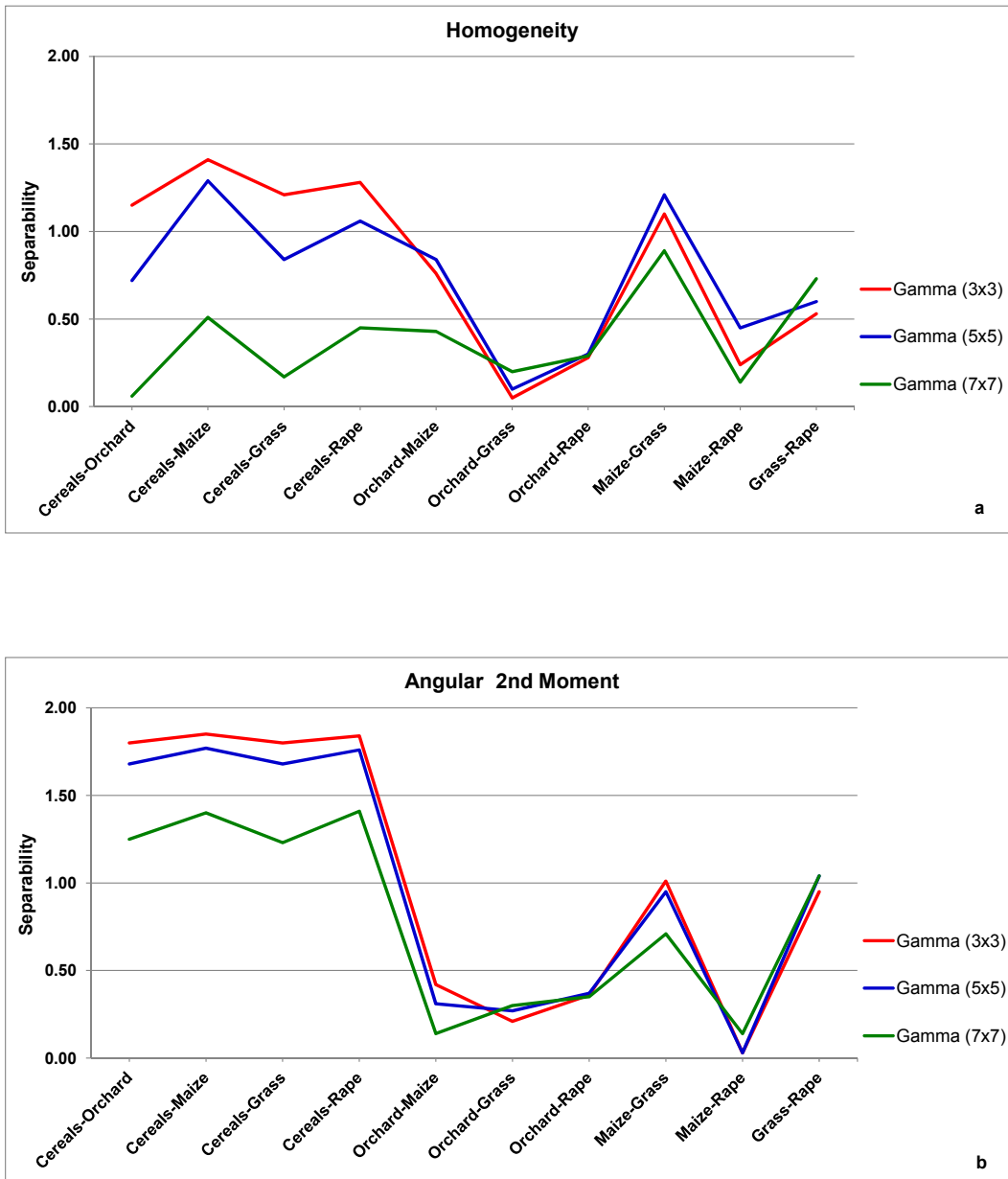


Figure 4.16. Effect of filter's kernel size on separability values for TSX imagery of 31/05/2010. a) homogeneity, and b) angular 2<sup>nd</sup> moment texture features.

## 4.8 Conclusion

Texture analysis on a pre-defined plot basis proved to have a high potential in processing SAR images for the use in land cover classification. Full flexibility is offered by the developed software solution with respect to features, directions, and distances associated to texture, whilst the performance of all members of the calculated feature space can well be evaluated and reduced to a best-performing subset. Various feature combinations can easily be tested. Some of them can deliberately be included or excluded to estimate individual effects like those of direction or distance.

The so far developed software might help in gaining more knowledge about the information content of high-resolution SAR imagery in relation to the acquisition date. Until present all tests have been carried out with images presenting late spring phenology of the farm land. Using a time-series comprising phenological stages from late winter till harvest time might reveal variations of image texture due to cultivation measures and plant development. The prediction of an optimum data acquisition time is feasible.

## 5 Plot-Based Multi-Direction /-Distance Texture Analysis Model for Agricultural Land Cover Classification Using SAR Data

### II - Classification Module

#### 5.1 Introduction

As discussed in the previous section, the multi-distance and multi-direction Texture Analysis and Classification (TACL) model supports various classification approaches. Whereas the integration with R programming language facilitates a wide range of classification capabilities. This results in a flexible use and choice of the proper classification method according to the given classification problem. This section aims to give an overview of the main classification methods used in this model. Also, to evaluate those approaches using extracted SAR texture features for land cover classification. The optimum texture features could be defined depending on the separability value, as explained in the previous section, in addition to other data selection methods.

Different land-use/cover classification methods may be needed for different problems under different environmental conditions, making generalization and hence automation of the image classification process across time and space extremely difficult (Nina 2008). The question which classification approach is suitable for a specific study is not easy to answer. Different classification results may be obtained depending on the classifier(s) chosen (Lu & Weng 2007). As a result, new and sophisticated classification methods designed to improve the classification process continue to appear in the literature (Gong 2006; Jensen 2005; Nina 2008). Various approaches have been developed and successfully applied to SAR data, such as Maximum likelihood (Davidson *et al.* 2006; Frery, Correia & Freitas 2007; Kwarteng *et al.* 2008; Xing *et al.* 2010), fuzzy methods (Carincotte, Derrode & Bourennane 2006; Kersten, Lee & Ainsworth 2005; Park & Moon 2007), support vector machine (Lardeux *et al.* 2009; Lardeux *et al.* 2011; Michifumi Yoshioka, Toru Fujinaka & Sigeru Omatu 2008; Zhang *et al.* 2010), artificial neural network (Kuplich 2006; Peng, Wang & Zhang 2005; Zhang & Wu 2011; Zhang, Wu & Wei 2009), logistic regression

(Borghys *et al.* 2006), object-based classification (Benz *et al.* 2004; Definiens AG 2007; Evans *et al.* 2010) and others. However, these methods require extensive training and human supervision (Nina 2008).

Lu and Weng (2007) suggest that designing a suitable image processing procedure is a prerequisite for a successful classification of remotely sensed data into a thematic map. Effective use of multiple features of remotely sensed data and the selection of a suitable classification method are especially significant for improving classification accuracy (Lu & Weng 2007). Many factors, such as spatial resolution of the remotely sensed data, different sources of data, a classification system, and availability of classification software must be taken into account when selecting a classification method for use. Different classification methods have their own merits.

Non-parametric classifiers such as neural network, decision tree classifier, and knowledge-based classification have increasingly become important approaches for multisource data classification (Lu & Weng 2007). With non-parametric classifiers, the assumption of a normal distribution of the dataset is not required. No statistical parameters are needed to separate image classes. Non-parametric classifiers are thus especially suitable for the incorporation of non-spectral data into a classification procedure. Much previous research has indicated that non-parametric classifiers may provide better classification results than parametric classifiers in complex landscapes. Among the most commonly used non-parametric classification approaches are neural networks, decision trees, support vector machines, and expert systems (Lu & Weng 2007). Integration of remote sensing, geographical information systems (GIS), and expert system emerges as a new research frontier (Lu & Weng 2007).

## **5.2 Feature Extraction and Selection**

Selecting suitable variables is a critical step for successfully implementing an image classification. Many potential variables may be used in image classification, such as, textural or contextual information, multi-temporal images, multi-sensor images, and ancillary data. Due to different capabilities in land-cover separability, the use of too many variables in a classification procedure may decrease classification accuracy (Price, Guo & Stiles 2002). It is important to select only the variables that are most useful for separating land-cover or vegetation classes, especially when hyper-

spectral or multisource data are employed (Lu & Weng 2007). Many approaches, such as principal component analysis, discriminant analysis, non-parametric weighted feature extraction, and Bhattacharyya distance, Jeffreys–Matusita distance (Asner & Heidebrecht 2002; Lobell *et al.* 2002; Myint 2001; Okin *et al.* 2001; Platt & Goetz 2004) may be used for feature extraction in order to reduce the data redundancy inherent in remotely sensed data or to extract specific land-cover information (Lu & Weng 2007).

In practice, a comparison of different combinations of selected variables is often implemented, and a good reference dataset is vital. In particular, a good representative dataset for each class is the key for implementing a supervised classification. The divergence-related algorithms are often used to evaluate the class separability and then to refine the training samples for each class (Lu & Weng 2007).

### **5.3 Feature Selection Methods**

The TACL model supports several feature selection methods. In addition to the separability method, which is discussed in Section 3, there are two approaches available in the classification module. Attribute selection approach and Principle Component Analysis (PCA) approach.

#### **5.3.1 Attribute Selection Approach**

The attribute selection approach provides various functions for selecting attributes from a given dataset. This process identifies and removes as much of the irrelevant and redundant information as possible. This approach contains different algorithms for filtering attributes, i.e. Entropy ( $H$ ) based filters (information gain, gain ratio, symmetrical uncertainty), and Random Forest filter (random forest importance). In addition, algorithms for choosing a subset of ranked attributes based on attributes' weights. These algorithms are available in “FSelector” package which is utilised in the current model (Piotr 2011).

##### **5.3.1.1 Entropy-Based Filters**

The algorithms find weights of discrete attributes based on their correlation with continuous class attribute.

- Information Gain is

$$H(\text{Class}) + H(\text{Attribute}) - H(\text{Class}, \text{Attribute})$$

- Gain Ratio is

$$\frac{H(\text{Class}) + H(\text{Attribute}) - H(\text{Class}, \text{Attribute})}{H(\text{Attribute})}$$

- Symmetrical Uncertainty is

$$\frac{H(\text{Class}) + H(\text{Attribute}) - H(\text{Class}, \text{Attribute})}{2(H(\text{Attribute}) + H(\text{Class}))}$$

### 5.3.1.2 Random Forest Filter

The algorithm finds weights of attributes using Random Forest (RF) algorithm. RF is a newly developed machine learning algorithm as an extension to classification and regression trees (CART). The basic idea is to construct many trees using random vectors sampled from a data set. RF is able to provide a number of excellent features, for instance, the capability of handling a large number of variables, ranking the variables, and detecting the interaction among the variables (Yang 2010).

### 5.3.1.3 Cut-offs Algorithms

These algorithms choose a subset of ranked attributes based on attributes' weights. Therefore, after finding these weights through different filter-attribute algorithms, a specific subset can be extracted using one of the following methods:

- Cutoff k: chooses k best attributes
- Cutoff k percent: chooses best k \* 100% of attributes
- Cutoff biggest difference: chooses a subset of attributes which are significantly better than others.

### 5.3.2 Principle Component Analysis

Principal component analysis (PCA) as statistical technique aims, in general terms, at reducing the complexity of the interrelationships among a potentially large number of observed variables to a relatively small number of linear combinations of them, which

are referred to as principal components (Raykov & Marcoulides 2008). These components are uncorrelated, and ordered so that the first few retain most of the variation present in all of the original variables (Jolliffe 2002).

#### **5.4 Use of Multiple Features of Remotely Sensed Data**

As discussed previously, remote-sensing data have many unique spatial, spectral, radiometric, temporal and polarisation characteristics. Making full use of these characteristics is an effective way to improve classification accuracy. Generally speaking, the feature of spectral response is the most important information used for land-cover classification. As high spatial resolution data become readily available, textural and contextual information become significant in image classification (Lu & Weng 2007).

#### **5.5 The R Environment**

R is an environment for data analysis and graphics based on a high-level language (Crawley 2007). It is an open-source project developed by dozens of volunteers (Everitt & Hothorn 2006) and is made available through the Internet under the General Public License (GPL). This means it is supplied with a license that allows you to use it freely, distribute it, or even sell it, as long as the receiver has the same rights and the source code is freely available (Dalgaard 2002).

R is an integrated suite of software facilities for data manipulation, calculation and graphical display. Among others, it has:

- an effective data handling and storage facility,
- a suite of operators for calculations on arrays, in particular matrices,
- a large, coherent, integrated collection of intermediate tools for data analysis,
- graphical facilities for data analysis and display either directly at the computer or on hardcopy, and
- a well-developed, simple and effective programming language (called 'S') which includes conditionals, loops, user defined recursive functions and input and output facilities (Indeed most of the system-supplied functions are themselves written in the S language).

The term “environment” is intended to characterise it as a fully planned and coherent system, rather than an incremental accretion of very specific and inflexible tools, as is frequently the case with other data analysis software. “R” is very much a vehicle for developing new methods of interactive data analysis. It has developed rapidly, and has been extended by a large collection of packages. However, most programs in “R” are essentially ephemeral, written for a single piece of data analysis (Venables, Smith & Core Team 2011).

## **R Packages**

All R functions and datasets are stored in packages. Only when a package is loaded, its contents are available. This is done both for efficiency (the full list would take more memory and would take longer to search than a subset), and to aid package developers who are protected from name clashes with other codes (Venables, Smith & Core Team 2011).

## **5.6 Classification Approaches**

Image classification approaches may be grouped into supervised and unsupervised, or parametric and nonparametric, or hard and soft (fuzzy) classification, or per-pixel, sub-pixel, and per-field (Lu & Weng 2007). In recent years, many advanced classification approaches, such as artificial neural networks, fuzzy-sets, and expert systems, have been widely applied for image classification (Lu & Weng 2007).

The parametric classifiers assume that a normally distributed dataset exists, and that the statistical parameters (e.g. mean vector and covariance matrix) generated from the training samples are representative. However, the assumption of a normal spectral distribution is often violated, especially in complex landscapes. In addition, insufficient, non-representative, or multimode distributed training samples can further introduce uncertainty to the image classification procedure. Another major drawback of the parametric classifiers lies in the difficulty of integrating spectral data with ancillary data. The maximum likelihood may be the most commonly used parametric classifier in practice, because of its robustness and its easy availability in almost any image-processing software.

With non-parametric classifiers, the assumption of a normal distribution of the dataset is not required. No statistical parameters are needed to separate image classes.

Non-parametric classifiers are thus especially suitable for the incorporation of non-spectral data into a classification procedure (Lu & Weng 2007). Much previous research has indicated that non-parametric classifiers may provide better classification results than parametric classifiers in complex landscapes (Foody 2002). Among the most commonly used non-parametric classification approaches are neural networks, decision trees, support vector machines, and expert systems (Lu & Weng 2007).

### **5.6.1 Artificial Neural Network**

Artificial Neural Networks (ANNs) is a quantitative method for data analysis. It is based on the simulation of biological nervous systems' functions. The basic premise of this approach is that biological systems perform extraordinarily complex computations without recourse to explicit quantitative operations (Rosaria 2007). Generally, an ANN is an adaptive system that changes its structure based on external or internal information that flows through the network (Bhatta 2010). An advantage of ANNs lies in the high computation rate achieved by their massive parallelism, resulting from a dense arrangement of interconnections (weights) and simple processors (neurones), which permits real-time processing of very large data sets (Tso & Mather 2009). Furthermore, the nonparametric nature of ANN, arbitrary decision boundary capability, easy adaptation to different types of data and input structures, fuzzy output values, and generalisation for use with multiple images, making it a promising technique for land-cover classification (Lu & Weng 2007).

ANN may be viewed as a mathematical model composed of non-linear computational elements, named neurons, operating in parallel and connected by links characterised by different weights. A single neuron computes the sum of its inputs, adds a bias term and drives the result through a general non-linear activation function to produce a single output (Pacifici *et al.* 2008). Since the neural networks do not need any information about the probability distribution and a priori probabilities of different classes, they are widely used in pattern classification (Zhang, Wu & Wei 2009). However the performance of ANN depends to a significant extent on how well it has been trained (Tso & Mather 2009). A two-hidden-layer back-propagation neural network is adopted with sigmoid neurones in the hidden layers and linear neuron in the output layer. In this technique, the available data is divided into three subsets.

The first one is the training subset, which is used for computing the gradient and updating the network weights/biases, the second one is the validation subset, and the third one is the test subset (Zhang, Wu & Wei 2009).

During the training phase, the neural network “learns” about regularities present in the training data, and then constructs rules that can be extended to the unknown data. This is a special capability of neural networks. However, the architecture of the network, parameters such as the learning rate, and the rate of convergence of a neural network must be defined. There are no clear rules to assist with the design of the network. In general, five kinds of fundamental neural network architecture have been, or can be, used for classifying remotely sensed images. These kinds are the multilayer perceptron with back-error propagation, the self-organised feature map (SOM), counter-propagation networks, Hopfield networks, and ART systems (Tso & Mather 2009). Whereas the multilayer-perceptron with back-propagation technique is applied in the current study, it is discussed in quite details as follows.

### **Multilayer Perceptron**

The multilayer perceptron using the back-propagation learning algorithm (Pacifici *et al.* 2008; Tso & Mather 2009) is one of the most popular type of neural network in image classification. However, the accuracy of image classification is sensitive to the variation in the dimensionality of a dataset and the characteristics of training and testing sets (Lu & Weng 2007). In the case of networks with more than one layer of artificial neurons, and only forward connections from the input towards the output are allowed, these networks are called Multi-Layer Perceptrons (MLP) or Multilayer Feed-forward Neural Networks. Where each MLP consists of a set of input terminals, an output neural layer, and a number of layers of *hidden* neural units between the input terminals and the output layer (Rosaria 2007). A typical three-layer multilayer perceptron neural network is shown in Figure 5.1a. It can be seen that the leftmost layer of neurones in Figure 5.1a is the input layer, which contains the set of neurones that receive external inputs (i.e. feature values), and performs no computations, unlike the elements of the other layers. While the central layer is the hidden layer (Tso & Mather 2009).

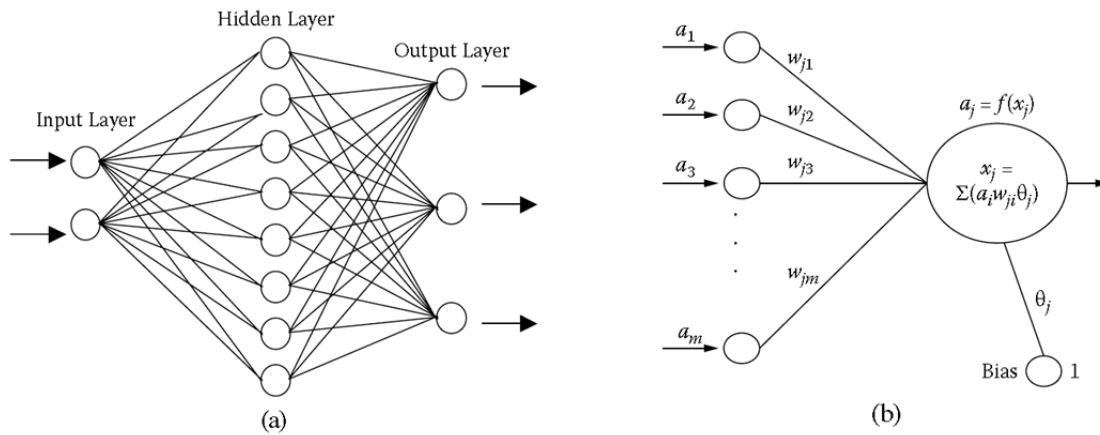


Figure 5.1. a) A typical three-layer multilayer perceptron neural network, and b) Example of forward propagation procedure on neurone  $j$  (Tso & Mather 2009).

The classification results are produced by the output layer (the rightmost layer of neurones). Within the same layer, there are no interconnections between neurones, but all of the neurones in a given layer are fully connected to the neurones in the adjacent layers. And the adjusted numerical weights  $w_{jm}$  are assigned to the interconnections. The value held by each neurone is called its *activity*  $a_m$  as shown in Figure 4.1b. The performance of a multilayer perceptron is controlled by several factors: the model-associated parameters, the network structure, and the nature of the training samples. Choosing the optimum combination of those factors is very difficult. For the most classification problems, a single hidden layer is enough. Whereas, for the large number of output classes, using two hidden layers may produce a more accurate result (Tso & Mather 2009).

### Back-Propagation

The back-propagation rule is used in the training process of the multilayer perceptron (Mather 2004). The discrimination capability of an ANN is contained in its weights. During training, the numerical weights  $w_{jm}$  are iteratively adjusted towards a configuration that allows the network to discriminate the prototype patterns of interest. The back-propagation algorithm minimizes the squared error over all patterns at the output of the network (Schowengerdt 2007). It involves two major steps, namely *forward* and *backward* propagation, to accomplish its modification of the neural state. The back-propagation is the most popular algorithm used for

updating the neuronal activities and the interconnection weights in a multilayer perceptron (Tso & Mather 2009).

### **Neural Networks in Remote Sensing Image Classification**

Neural networks have been most widely used in remote sensing for image classification and regression-type analyses. Due to their freedom from restrictive assumptions as well as practical demonstrations of their ability to commonly provide more accurate outputs than conventional methods, the use of neural networks for classifying remotely sensed imagery has developed rapidly (G.M.Foody 2006; Tso & Mather 2009). The multilayer perceptron is the most popular neural network classifier in remote sensing (Atkinson & Tatnall 1997; Kanellopoulos & Wilkinson 1997; Paola & Schowengerdt 1995). Recently, several studies archived higher classification accuracy using the Artificial Neural Networks (Canty 2009; Gong, Im & Mountrakis 2011; Heremans *et al.* 2011; Shimoni *et al.* 2009).

#### **5.6.2 Support Vector Machine**

Support Vector Machines (SVMs) has become an increasingly popular tool for machine learning tasks involving classification, recognition, or detection. SVM is based on the statistic learning theorem's VC Dimension concept and Structure Risk Minimization (SRM) principle. However, the SVM method does not need the statistic features of the training samples and it can easily deal with high-dimension data and nonlinear problems and can also achieve global optimisation (Zhang *et al.* 2010). The aim of Support Vector classification is to devise a computationally efficient way of learning 'good' separating hyper-planes in a high-dimensional feature space. The generalisation theory gives clear guidance about how to control capacity and hence prevent over-fitting by controlling the hyper-plane margin measures. Optimisation theory will provide the mathematical techniques necessary to find hyper-planes optimising these measures, and to study their properties (Nello & John 2007).

SVM fundamental idea is that the feature of input space is mapped into a high-dimensional feature space through nonlinear transformation. Then the Optimal Separating Hyper-plane (OSH) is established in the feature space. The nonlinear transformation is implemented by defining a proper kernel function. SVM has two

important features. First, the upper bound on the generalisation error does not depend on the dimension of the space. Second, the error bound is minimised by maximizing the margin, i.e. the minimal distance between the hyper-plane and the closest data points (Zhang *et al.* 2010).

The attractiveness of SVMs is their ability to minimise the so-called structural risk, or classification errors, when solving the classification problem. The structural risk minimisation concept adopted by SVMs is to minimise the probability of misclassifying a previously unseen data point drawn randomly from a fixed but unknown probability distribution. Such a property is also different from the decision boundary–forming logic of ANN. Specifically, SVM training always finds a global minimum (Tso & Mather 2009). SVMs may reach in terms of accuracy performances similar to those obtainable by means of neural networks without suffering from the problem of local minima and with limited effort required for architecture design (Pacifici *et al.* 2008). It is not necessarily that all the training samples contribute to the building of the hyper-plane, but normally only a subset of training samples are chosen as support vectors. This attribute is unique to SVMs. As shown in Figure 5.2, only the shaded points are support vectors that define the hyper-plane  $b$  separating the two classes with maximal distance (Tso & Mather 2009).

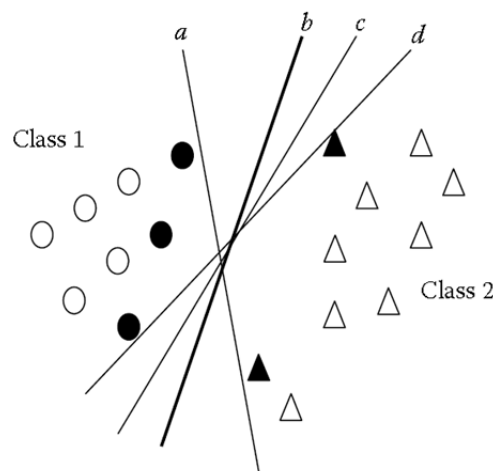


Figure 5.2. Hyper-plane  $b$  separates the two classes with the maximal margin.

## Parameter Determination

Performance of SVM models can be improved by defining the appropriate parameters. Two of these parameters are the Cost of Penalty (C) and Gaussian Kernel Parameter ( $\sigma$ ). The parameter C influences the classification performance. If C is too large, the classification accuracy is very high in training data set, but very low in testing data set. If C is too small, the classification accuracy is lower. The parameter  $\sigma$  has more influence than parameter C on classification outcome, because the value affects the partitioning outcome in the feature space. Over-fitting and under-fitting occur in case of large value and small value of parameter  $\sigma$  respectively. In order to determine the parameters of SVM models, the Grid search is the most common approach. However, this approach is a local search technique, and tends to reach the local optima. Moreover, setting appropriate search intervals is an essential problem (Cortez 2011; Pai & Hsu 2011). The concept of grid search is similar to that of the exhaustive search within a solution space. The user starts by randomly choosing the parameter values that are input to the classifier to evaluate the  $t$ -fold cross-validation performance. Then the parameter values are increased or decreased, and the performance is re-evaluated until all the chosen parameters have been evaluated (Tso & Mather 2009).

## SVM Classification of Remotely Sensed Data

Recent studies have shown that using SVMs to deal with classification issues may result in higher accuracy than other classifiers and also require fewer training samples. E.g. Huang *et al.* (2002) analysed four kinds of classifiers, including SVMs, maximum likelihood (ML), ANN and the decision tree classifier, and concluded that the SVMs generate more stable overall accuracies (Huang, Davis & Townshend 2002). Also, Pal and Mather (2005) compare SVMs with ML and ANN methods. The results showed that the SVMs achieved a higher level of classification accuracy than either the ML or the ANN classifier. Moreover, the SVM can be used with small training data sets and high-dimensional data (Pal & Mather 2005). On the other hand, Foody and Mathur (2004, 2006) investigated both the characteristics and the size of training samples in SVMs, and illustrated the training data acquisition strategies to allow efficient and accurate image classification by small training samples (Foody & Mathur 2004; Foody & Mathur 2006). The study made by Keuchel *et al.* (2003) also

showed that SVMs are useful in classifying remotely sensed imagery (Keuchel *et al.* 2003).

### **5.6.3 Logistic Regression**

Statistics models are empirical models by nature and include both linear and logistic regression models that relate a dependent variable to one or more independent variables, which can be further used for prediction and simulation. When both dependent and independent variables are numerical, the linear regression model is applied. While in the case that the dependent variable is categorical and independent variables are numerical, categorical, or both, then the logistic regression should be used. Logistic regression uses the natural logarithm of the odds as the dependent variable. It does not require linear relationships between the dependent and the independents, but does assume a linear relationship between the logit of  $y$  and the independents. In this sense, logistic regression is still intrinsically linear (Wang, Zhou & Yang 2009).

### **5.6.4 Linear Discriminant Analysis**

Linear discriminant analysis (LDA) is a learning algorithm which has the advantages of simplicity and intuitiveness. It also referred to as Fisher discriminant analysis (FDA) and has been widely used in many areas. LDA aims at finding a linear function which linearly combines independent variables using a set of weights (model parameters) to determine the property of a dependent variable. The linear function is also called a hyper-plane which separates two classes of input vectors. The hyper-plane is called the decision boundary or surface while the linear function is called a linear classifier. This linearity does not mean data are completely separable. Data are often not separable even when generated from two linearly separable sources. Rather they are not separable because of large overlap (Yang 2010).

### **5.6.5 K-Nearest Neighbour**

K-Nearest Neighbour (KNN) is known as a fast learner because there is nearly no learning process at all. The theoretical background of KNN is simple. Imagine that there are  $K$  training input vectors around a query input vector within a specified volume, like shown in Figure 5.3. In this Figure the query input vector denoted by the

triangle is surrounded by two classes of training input vectors. Here, training input vectors are used to indicate that they have already been classified (Yang 2010).

### 5.7 Combination of Multiple Classifiers

Different classifiers such as parametric classifiers (e.g. maximum likelihood) and non-parametric classifiers (e.g. neural network, decision tree) have their own strengths and limitations (Tso & Mather 2009). For example, when sufficient training samples are available and the feature of land covers in a dataset is normally distributed, a maximum likelihood classifier (MLC) may yield an accurate classification result. In contrast, when image data are anomalously distributed, neural network and decision tree classifiers may demonstrate a better classification result (Lu *et al.* 2004; Pal & Mather 2003). Previous research has indicated that the integration of two or more classifiers provides improved classification accuracy compared to the use of a single classifier (Huang & Lees 2004; Steele 2000). A critical step is to develop suitable rules to combine the classification results from different classifiers. Some previous studies explored different techniques such as a production rule, a sum rule, stacked regression methods, majority voting, and thresholds to combine multiple classification results (Lu & Weng 2007).

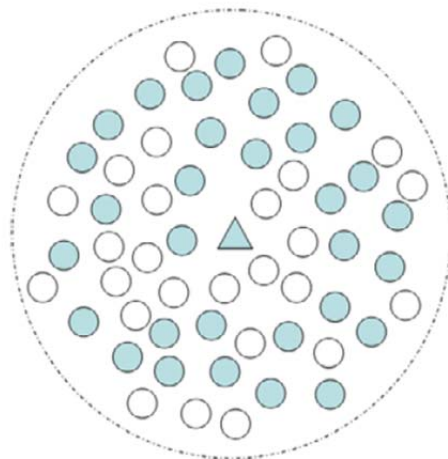


Figure 5.3. An illustration of KNN. The open circles and the filled circles represent two classes of data while the triangle represents a query data point. The dashed circle indicates the volume centred by the query data point (Yang 2010)

## 5.8 Selection of a Classification System and Training Samples

A suitable classification system and a sufficient number of training samples are prerequisites for a successful classification. Cingolani *et al.* (2004) identified three major problems when medium spatial resolution data are used for vegetation classification: defining adequate hierarchical levels for mapping, defining discrete land-cover units discernible by selected remote-sensing data, and selecting representative training sites (Cingolani *et al.* 2004). In general, a classification system is designed based on the user's need, spatial resolution of selected remotely sensed data, compatibility with previous work, image-processing and classification algorithms available, and time constraints. Such a system should be informative, exhaustive, and separable. In many cases, a hierarchical classification system is adopted to take different conditions into account. Many factors, like spatial resolution of the remotely sensed data, different sources of data, a classification system, and availability of classification software must be taken into account when selecting a classification method. Different classification methods have their own merits. The question which classification approach is suitable for a specific study is not easy to answer. Different classification results may be obtained depending on the classifier(s) chosen (Lu & Weng 2007).

## 5.9 Classification Accuracy Assessment

In addition to errors from the classification itself, other sources of errors, such as position errors resulting from the registration, interpretation errors, and poor quality of training or test samples, all affect classification accuracy. In general, the difference between an image classification results and the reference data is assumed to be due to the classification error. However, to provide a reliable report on classification accuracy, non-image classification errors should also be examined, especially when reference data are not obtained from a field survey. Generally, a classification accuracy assessment includes three basic components: sampling design, response design, and estimation and analysis procedures. Selection of a suitable sampling strategy is a critical step. The major components of a sampling strategy include sampling unit (pixels or polygons), sampling design, and sample size (Lu & Weng 2007).

The error matrix (sometimes called a confusion matrix or a contingency table) is one of the most common means used in classification accuracy assessment. Error matrices compare, on a category-by-category basis, the relationship between known reference data (ground truth) and the corresponding results of an automated classification. Such matrices are square, with the number of rows and columns equal to the number of categories whose classification accuracy is being assessed (Lillesand, Kiefer & Chipman 2008). The error matrix is used to derive other important accuracy assessment elements such as overall accuracy, omission error, commission error, and kappa coefficient. The kappa coefficient is a measure of overall statistical agreement of an error matrix, which takes non-diagonal elements into account. Kappa analysis is recognised as a powerful method to analyse a single error matrix and compare the differences between various error matrices (Lu & Weng 2007). Classification accuracy depends mainly on the quality of features which should be robust with maximum discrimination power and must encompass most of the information available in the data (Zhang, Wu & Wei 2009).

## **5.10 Classification Model Description**

### **5.10.1 Implementation**

As explained in Section 4, the present model has been implemented as an add-in to ESRI ArcGIS software. A toolbox allowing any user interaction to the added functionality can be opened. On the basis a polygon-feature and the derivation of texture measures, and in order to support different classification methods with flexible user-controlled selection, two main programming tasks have been dedicated to the GLCM calculation.

For the classification module, the general capability of the “R” environment and the available free packages for various elaborate classification techniques, in addition to an available interface allowing an integration of R-classes into the VB.NET source, were utilised. Figure 5.4 represents the methodological flowchart. The current model enables the user to export the training, reference and test data (Figure 5.5) for a use in the “R” environment and calls the respective “R” code for the selected classification method. For convenience, the “R” code remains invisible to the user, since it is generated by the VB.NET program in the background.

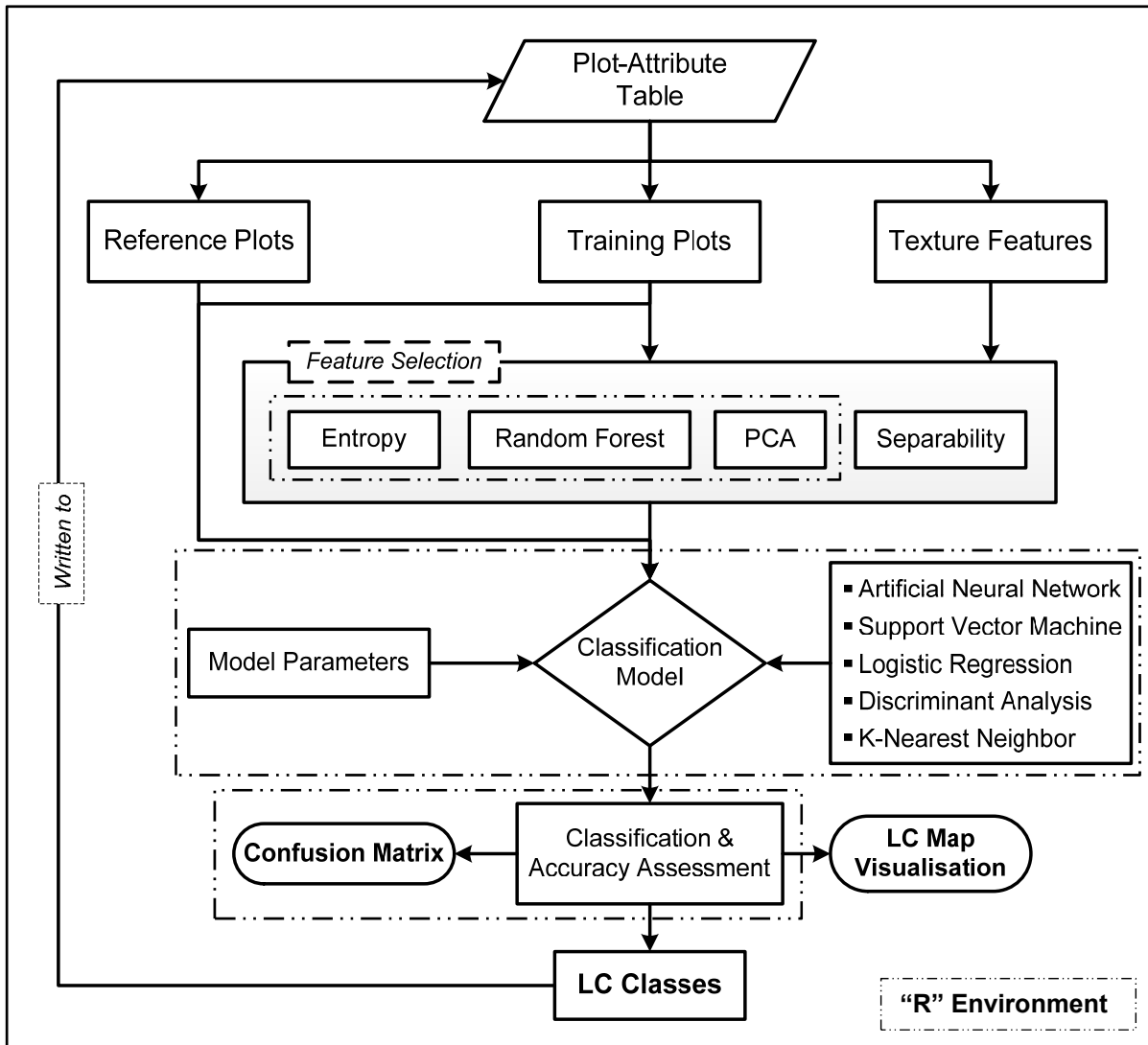


Figure 5.4. Methodological flowchart.

The corresponding user interface is given in Figure 5.6. Finally, the classification results are written back to the ArcGIS polygon attribute table. In addition, classification accuracy and kappa index are displayed in the model interface. Using a predefined colour scheme, the class assignment becomes visible in the map document immediately after the classification has been finished. Moreover, the selected features for the classification process can be modified, either manually or automatically, using one of the provided methods for feature selection. The model supports mainly two options: Attribute Selection methods (Entropy and Random Forest; Figure 5.7) and Principle Component Analysis (PCA; Figure 5.8). These two options can be applied either to all feature datasets or to a subset of features. On the other hand, the confusion matrix is saved as text file and could be shown in a matrix

format or in graphical format (Figure 5.9). Therefore, different classification methods using different combinations of texture features can be quickly evaluated.

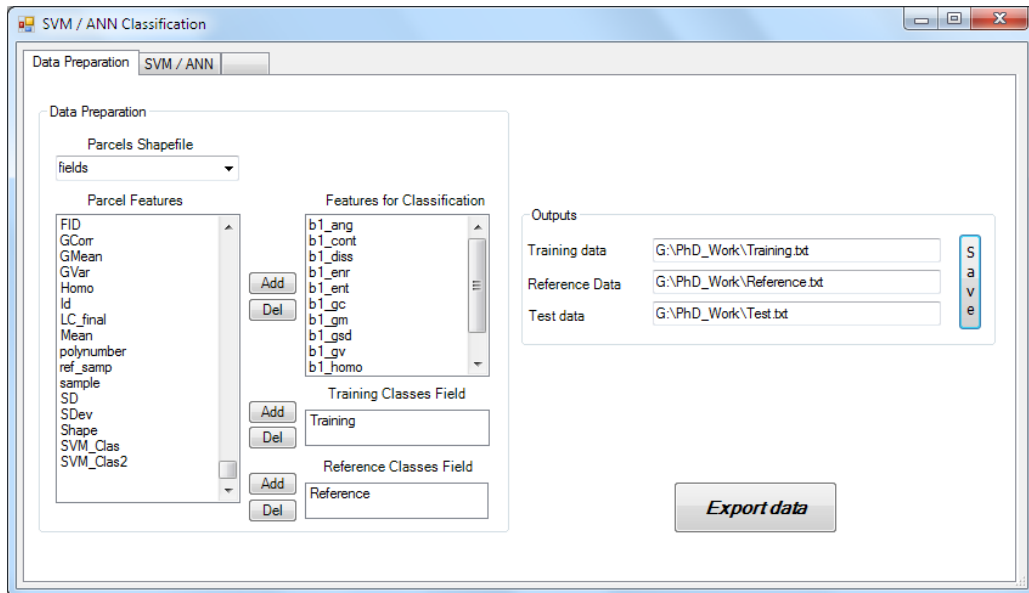


Figure 5.5. The user interface for data preparation.

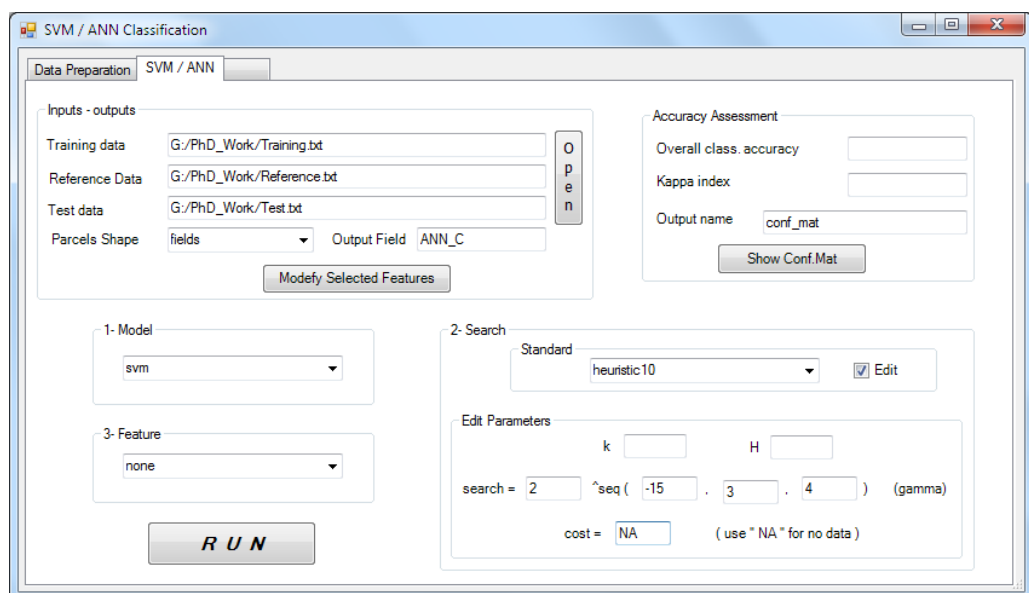


Figure 5.6. The user interface supporting different classification methods.

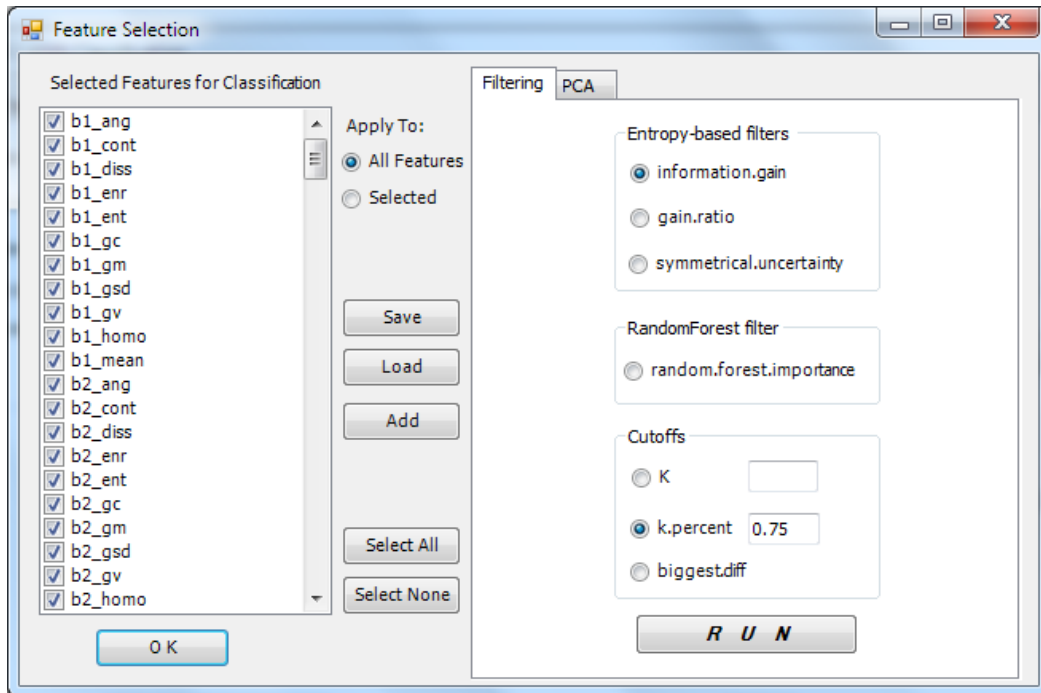


Figure 5.7. The user interface to modify the features selected for classification using filtering (attribute selection) methods.

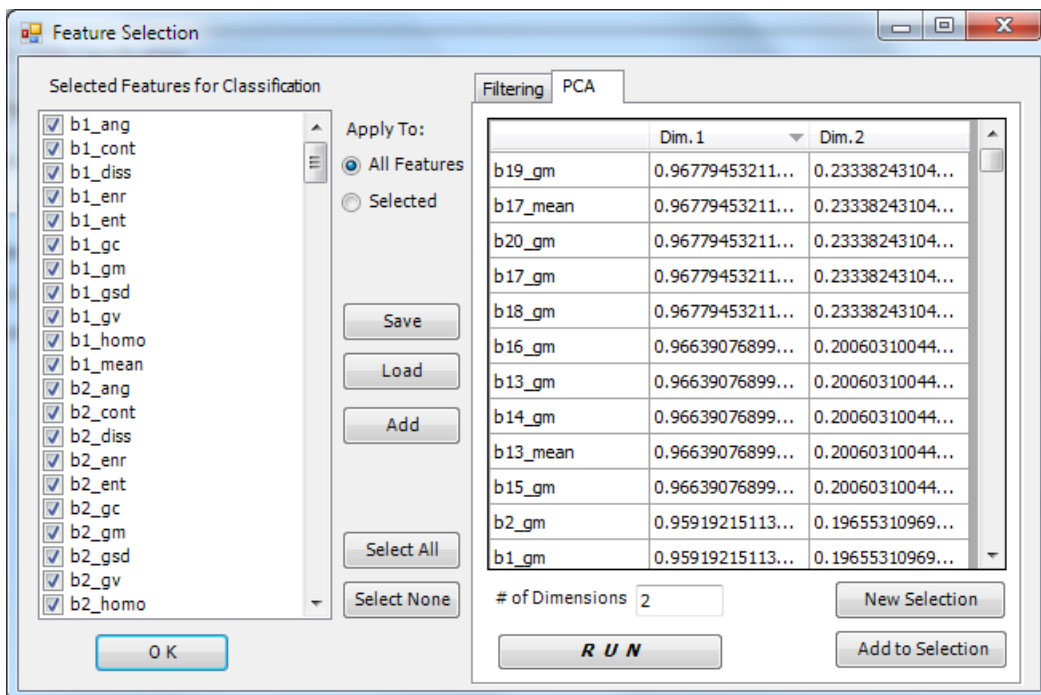


Figure 5.8. The user interface to modify the features selected for classification using principle component analysis technique.

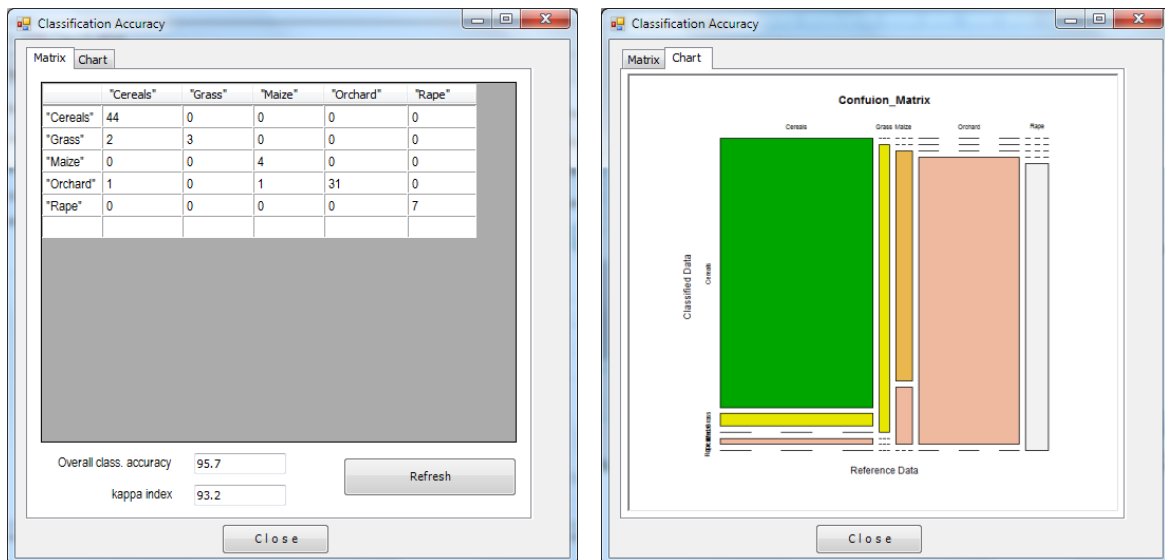


Figure 5.9. The classification accuracy results can be presented as confusion matrix (left) and graphical presentation (right).

### 5.10.2 R Packages Used in the Model

Several packages support different classification approaches. In the current model, the “rminer” package was chosen. This package facilitates the use of data mining algorithms in classification and regression tasks by presenting a short and coherent set of functions. While several DM algorithms can be used, it is particularly suited for Neural Networks (NN) and Support Vector Machines (SVM) (Cortez 2011). This package depends on other packages (nnet, kkn, kernlab, rpart, lattice, methods, and MASS).

### 5.11 Results of the Model Application

In order to evaluate and compare the supported classification and feature selection methods in the TACL model, the subsets of TSX images (dated 31/05/2010 and 17/06/2010), which are used in Section 4, are applied to land cover classification. Thus, both non-filtered images and Gamma (3x3) are used depending on the comparison results of different filters discussed in Section 4. A further image, termed Mean-TSX image, has been computed which contains the mean pixel intensities from both TSX images (Figure 5.10). On the other hand, the total number of plots (183) falls into two groups, one for training and a second one as independent reference (Table 5.1). The available classification methods were tested and compared for

TerraSAR-X images classification. For all classifications, accuracies and kappa indices were computed.

### 5.11.1 Classification and Feature Selection Methods

TerraSAR-X images were individually used for texture feature calculations. Whereas the model supports different feature-selection methods, the same parameters (i.e. TSX images, distances and directions) which have been used for separability analysis are again used for calculating texture features for all plots. Then, this texture-feature set is available for evaluating the feature selection methods in comparison to the separability method and their effects on classification results.

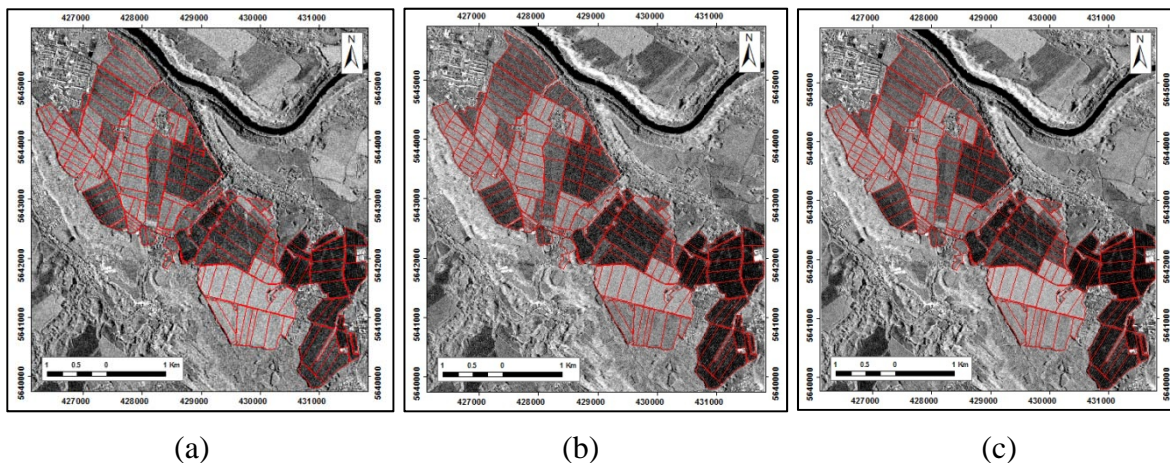


Figure 5.10. a) TSX image acquired on 31/05/2010, b) TSX image acquired on 17/06/2010 and c) Mean-TSX image. Redlines: parcel boundaries.

Table 5.1. Training and reference data used for land cover classification.

Crop	Training plots	Reference plots
Cereals	53	44
Maize	4	4
Rape	7	7
Grass	4	5
Orchard	22	33
<b>Total</b>	<b>90</b>	<b>93</b>

Table 5.2. Batch-code for image-direction combinations.

Direction	TSX 31.05.10	Gamma 31.05.10	TSX 17.06.10	Gamma 17.06.10	Mean Image
0°	b1	b5	b9	b13	b17
45°	b2	b6	b10	b14	b18
90°	b3	b7	b11	b15	b19
135°	b4	b8	b12	b16	b20

PCA as a feature selection method is important in the case of missing required training data for separability calculation (i.e. unsupervised classification). The combination of five images, four directions, ten texture features, mean and standard deviation of each image results in a total number of 205 features. The feature selection interface with checklist facilitates to select specific features; therefore, investigating different combinations is available (comparing images, comparing directions, etc.).

#### 5.11.1.1 Separability Analysis Approach

The separability values of texture features for each class-pair were sorted in a descending order. The first two-values are shown in Table B.1 (in Appendix B), from which the features with high separability values, in general more than 1.75 were utilised for classification using different methods. The classification was evaluated in two ways; first, using the highest values for each class-pair, after that using the highest two values of separability for each class-pair.

The results show that the classification accuracy varies according to the classification method (Table 5.3) and the number of features used in classification (Figure 5.11). In general, SVM performs better than other methods in both cases of selected separability values, after that come KNN and ANN (mlpe). According to the current results, choosing features with the highest separability values (for each class-pair) could provide high classification accuracy using SVM method.

Table 5.3. Classification performance using features selected by separability approach.

	Highest separability-value		Highest two separability-values	
	Accuracy %	Kappa%	Accuracy %	Kappa%
SVM	94.62	91.58	94.62	91.58
ANN (mlp)	89.25	83.51	91.40	86.90
ANN (mlpe)	92.47	88.22	91.40	87.11
KNN	91.40	86.58	93.55	89.94
LR	81.72	73.70	81.72	73.22
LDA	91.40	86.56	89.25	83.44

### 5.11.1.2 Attribute Selection Methods

In this module, two methods are provided Entropy-Based Filters (information gain, gain ratio and symmetrical uncertainty) and Random Forest filter (random forest importance). To evaluate these methods, different numbers of features were selected and used for classification, where the used cut-off method is “number of features”.

As shown in Tables B.2, B.3 and B.4, the classification accuracy values vary significantly from the first method to the second and third methods. Starting with 10 features, the Information Gain method performed well in the selection of the features that achieve significantly higher classification accuracy than other methods. These 10 features are shown in Table B.7 for all selection methods. It is, however, clear that selected features are in general mean, GLCM-mean and GLCM-variance, but the corresponding images are different.

The Information Gain method selected the TSX of 17/06/2010 and the Mean-TSX image, while for both Gain Ratio and Symmetrical Uncertainty the selected features are the same and the selected images are TSX of 31/05/2010 and Gamma 31/05/2010. This means that the Mean-TSX image provides more information required for classification. Such image is, somehow, a combination between both TSX images, in which the pixels having consistent values in both images are preserved closed to the original images. On the other hand, the pixels with different response in each image are re-presented as the mean values. These conditions exist in the current datasets, where the brightness of both maize and rape are too close in

the TSX of 31/05/2010 while they are easily distinguishable in TSX 17/06/2010. It also happens with some other land cover classes, which results in better separation between those classes in the new Mean-TSX image. The selected images in the case of Random Forest Importance are the Gamma of 17/06/2010 and the Mean-TSX image. Therefore, the classification (Table B.5) resulted in the same accuracy as that of the Information Gain method.

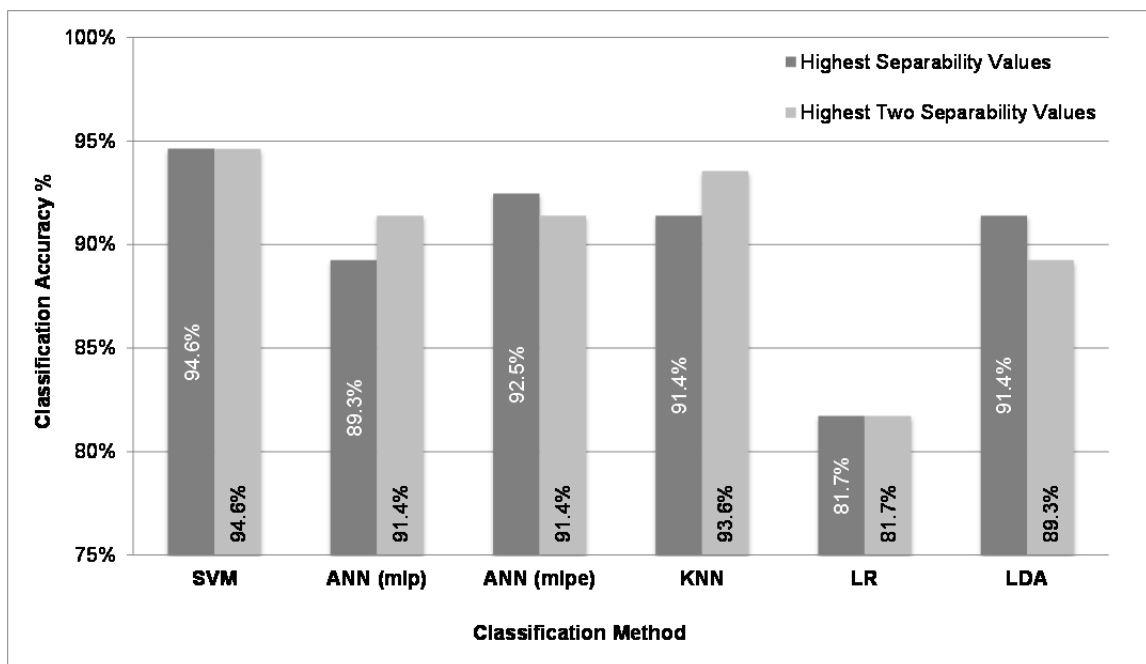


Figure 5.11. Performance of different classification methods using features selected according to their separability values.

On the other hand, for Gain Ratio and Symmetrical Uncertainty, increasing the number of features improved the accuracy. Selecting 30 features with Gain Ratio or 25 with Symmetrical Uncertainty performs the same accuracy as Information Gain or Random Forest Importance using 10 features. These last two methods, selecting more features than 10, causes a little variation in the accuracy except for the LR and LDA methods, where the accuracy decreases with the large number of features. Figure 4.13 shows the final assignment to five land-cover types using the SVM method based on 40 features, moreover, the confusion matrix and overall classification accuracy are illustrated in Table 5.4.

### 5.11.1.3 Principle Component Analysis

The principle component analysis can be applied to the texture features, and then the score values can be sorted in order to select features with highest values for classification. In the current comparison the dimension of PC is set to one, and then the selection is done with different numbers of features for classification comparison as shown in Table B.6. In comparison to the attribute selection methods, the selected 10 features using PCA (Table B.7) provided high accuracy like that of Information Gain method. The selected features are Mean and GLCM-Mean, and the images are Gamma (17/06/2010) and Mean-TSX image. More than 25 features, however, decrease the accuracy especially for KNN, LR and LDA.

Figure 5.12 depicts the comparison between different feature-selection methods and their performance in terms of the number of selected features, and the achieved classification accuracy. It is clear that both “information gain” and “random forest importance” perform well in all cases. The highest accuracy was achieved using “information gain” method to select 40 features.

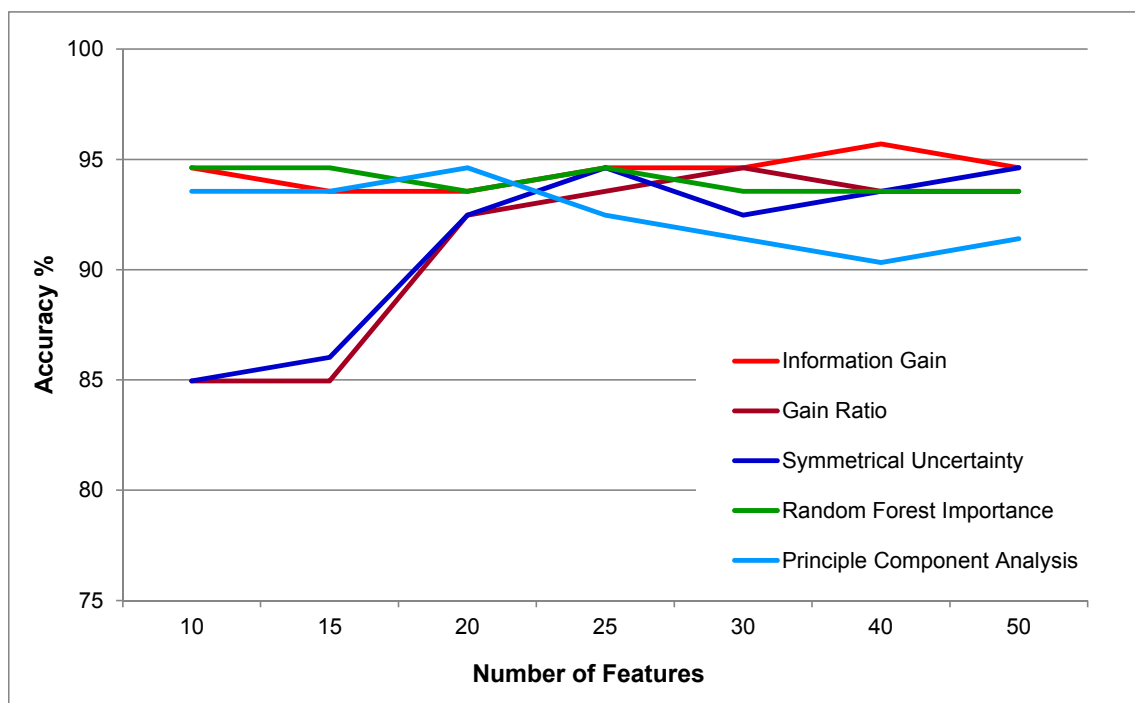


Figure 5.12. Performance of feature selection methods for different number of features and the classification accuracy using SVM.

Table 5.4. Overall classification accuracy statistics.

Classified Data	Reference Data					Sum.
	Cereals	Grass	Maize	Orchard	Rape	
Cereals	44	0	0	0	0	44
Grass	2	3	0	0	0	5
Maize	0	0	4	0	0	4
Orchard	1	0	1	31	0	33
Rape	0	0	0	0	7	7
<b>Sum.</b>	<b>47</b>	<b>3</b>	<b>5</b>	<b>31</b>	<b>7</b>	<b>93</b>
<b>Accuracy</b>						
Producer	94 %	100 %	80 %	100 %	100 %	
User	100 %	60 %	100 %	94 %	100 %	
<b><math>k_{hat}</math></b>	<b>93.20 %</b>					
<b>Overall Accuracy</b>	<b>95.70 %</b>					

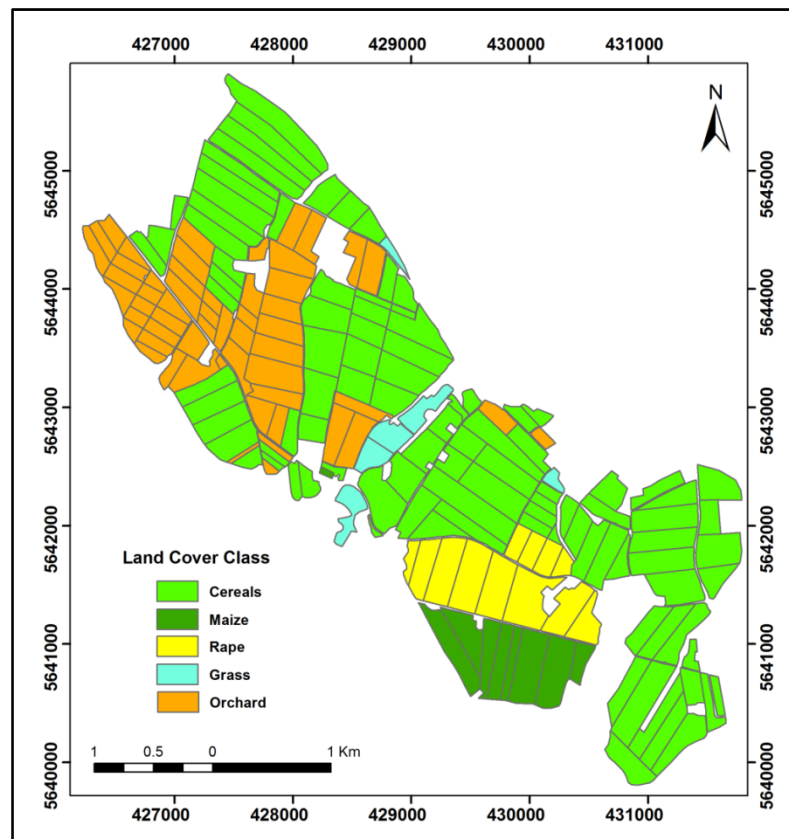


Figure 5.13. Land cover map based on the classification of TSX imagery acquired on 31/05/2010 and 17/06/2010 using SVM method.

## 5.12 Conclusion

The developed model provides various classification approaches in a flexible interaction like SVM and ANN. In addition, the capability of selecting the optimum features for further classification is supported. Feature selection can be conducted using i.e. separability analysis and principle component analysis. In order to evaluate and compare the supported classification and feature selection methods in the TACL model, the subsets of TSX images (dated 31/05/2010 and 17/06/2010) are applied to land cover classification. Different texture features were extracted for specific filtered images (according the obtained results in Section 4). Then the feature selection methods were utilised and subsequently different classification methods were evaluated. The results indicated that the separability analysis, entropy (Information Gain), random forest and principle component analysis perform well in feature selection (or data reduction). On the other hand the SVM performs better than other methods.

## 6 TerraSAR-X and ALOS PALSAR Data Application to Land Cover Classification

### 6.1 Introduction

Mapping and identifying land use/land cover (LULC) and its change is a highly important as well as the widely researched topic in remote sensing (Nina 2008). Radar remote sensing is an increasingly powerful tool for this mapping at regional and global scales (Henderson *et al.* 1998). Besides, Synthetic Aperture Radar (SAR) is unaffected by haze and clouds (Richards 2009), SAR data provide additional and unique vegetation characterizations when compared with the information obtained by optical imagery (Xianfeng *et al.* 2010). The magnitude of radar backscatter from agricultural targets is dependent upon frequency due to the variation in water contents and canopy parameters (Henderson *et al.* 1998).

Improvement of classification accuracy has been achieved for radar imagery (Blaes *et al.* 2005; Waske and Braun, 2009). Recently, TerraSAR-X (TSX) imagery (Baghdadi *et al.* 2009; Biro 2011; Breidenbach, Ortiz & Reich 2010; Burini *et al.* 2008; Esch *et al.* 2011; Mahmoud *et al.* 2011; Mróz & Mleczko 2008) and ALOS PALSAR imagery (Evans *et al.* 2010; Torbick *et al.* 2011; Wang *et al.* 2009; Zhang *et al.* 2009) have been used in various studies for land cover classification. Breidenbach *et al.* (2010) stated that the use of textural parameters (Haralick, Shanmuga & Dinstein 1973; Liang 2008; Lloyd *et al.* 2004; Tso & Mather 2009), object-based classification approaches and multi-temporal data can significantly improve the classification result of the TSX images.

In this section the capability of TerraSAR-X (X-band) and ALOS PALSAR (L-band) data for land cover classification in single and combined use, representing a multi-dimensional approach, is investigated. The TACL Model is used for land cover classification. The results show that the combined use of X- and L-Band improves the overall classification accuracy.

## 6.2 Multi-Dimensional SAR Data

Under certain conditions, however, a single channel and date of SAR data, provides useful information for crop classification, multi-dimensional SAR data improve the classification results (Henderson *et al.* 1998). In this context, there are several approaches for multi-dimensional SAR data (i.e., multi-frequency, multi-polarisation, multi-date, multi-features, etc.). Another concept for a multi-dimensional SAR data approach is the combination of tone and texture features extracted from a single image. As texture is an important feature in many types of images (Liang 2008; Rahul 2008), using textural parameters can improve the classification results of SAR images.

### 6.2.1 Multi-Frequency

Multi-sensor or multi-frequency data provide more information for the same land-cover type, whereas the crop-canopy behaviour differs according to the used frequency (Baghdadi *et al.* 2009; Kuhbauch *et al.* 1995; Schmullius & Nithack 1995). Multi-frequency data has been applied to various land-cover classification studies using different band-combinations. Pierce *et al.* (1995) used different frequencies (X-, C-, L-band) for land-cover classification. They concluded that the joint use of both C- and X-band could reveal accurate land cover classification, and it is likely that temporal changes can be accounted for in a single classifier to allow for accurate single-date classification maps (Pierce *et al.* 1995). De Matthaeis *et al.* (1995) used P-, L-, C-band for crop type identification where they found that L band is more effective for crops with low plant density, while C-band is better for high plant-density crops (de Matthaeis *et al.* 1995).

Recently several studies achieved better results based on the combination between L-, C- and X-band. Hoekman *et al.* (2011) used full-polarimetric C- and L-band (PALSAR) for classification of agricultural areas (Hoekman, Vissers & Tran 2011). Jia *et al.* (2009) studied the effect of integrating C- and X-band (TerraSAR-X) SAR data on the improvement of classification accuracy (Jia *et al.* 2009). Furthermore, the combined use of TerraSAR-X and ALOS PALSAR for land-cover classification (Lardeux *et al.* 2011; Xin *et al.* 2010) and for above-ground biomass estimations (Dhar *et al.* 2010; Englhart, Keuck & Siegert 2011) has been investigated and found effective in improving the results.

### 6.2.2 Multi-Polarisation

Multi-polarisation data has an advantage for crop mapping due to the significant effect of plant canopy on the depolarisation process. Many studies have been carried out using multi-polarisation data for land-cover classification (Stolz & Mauser 1995; Wever, Henkel & Hafner 1995). Skriver *et al.* (1999, 2000) analysed the Danish polarimetric L- and C-band SAR (EMISAR) for crop classification. They found that both dual-frequency and multi-temporal combination produce large improvements over single frequency, single data acquisitions (Skriver *et al.* 1999; Skriver, Schon & Dierking 2000). Jong-Sen *et al.* (2001) evaluated the classification capabilities for fully polarimetric (P-, L-, and C-band) combinations of dual polarisation and single polarisation SAR. They found that L-band fully polarimetric SAR data are best for crop classification, but P-band is best for forest age classification. Also, for crop classification, the L-band complex HH and VV can achieve correct classification rates almost as good as for full polarimetric SAR data. For forest age classification, P-band HH and VV should be used in the absence of fully polarimetric data (Jong-Sen, Grunes & Pottier 2001). Furthermore, PALSAR multi-polarisation and polarimetric data have been used for land cover/crop classification (McNairn *et al.* 2009; Xinwu, Touzi & Huadong 2008). Recently, the combination of different polarisations of ALOS PALSAR and TerraSAR-X proved to be effective in land cover classification (Dabrowska-Zielinska *et al.* 2010).

### 6.2.3 Multi-Temporal

Multi-temporal SAR data reflects variations over time. Therefore the crop monitoring and preferred times during the growing season for classification can be defined (Baghdadi *et al.* 2010; Nezry 1997; Park 2010; Schmullius & Nithack 1995; Schmullius & Schrage 1998). In addition, the temporal radar signature for land-cover classes can be investigated. Soo *et al.* (1998) investigated the temporal behaviour of ERS-2 images in delineating and mapping areas under different rice cropping systems (Soo *et al.* 1998). Del Frate *et al.* (2003) evaluated multi-polarisation and multi-temporal C-band for crop classification (Del Frate *et al.* 2003). Skriver (2008) used multi-temporal and polarimetric L-band for land-cover classification. He found that the best overall results are obtained using multi-

temporal information (Skriver 2008). Lam-Dao (2009) concluded that time-series Envisat ASAR imagery can generate accurate maps of rice-planted areas (Lam-Dao 2009). Also, temporal ALOS PALSAR data was applied to rice mapping (Wang *et al.* 2009). Skriver *et al.* (2011) used multi-temporal airborne SAR data to assess the performance of different polarisation modes for crop classification. They found that the multi-temporal information provides better results than that of multi-polarisation. If only few acquisitions are available, the polarimetric mode may perform better than the single and dual polarisation modes (Skriver *et al.* 2011).

#### **6.2.4 Multi-Features**

Using different features extracted from SAR imagery improves the classification results. Textural features are considered one of the most important features for land-cover mapping, especially in case of limited data sets (Paudyal, Eiumnoh & Aschbacher 1995; San Martin & Sadki 2004). Texture analysis of a single image improves the classification accuracy where the main land-cover classes can be defined (Esch *et al.* 2010; Mahmoud *et al.* 2011).

### **6.3 TerraSAR-X and ALOS/PALSAR for Land Cover Classification**

Several studies demonstrated the potentiality of different SAR data for land-cover classification. For example TerraSAR-X (Esch *et al.* 2011; Mahmoud *et al.* 2011; Mróz & Mleczo 2008) and PALSAR (Evans *et al.* 2010; Torbick *et al.* 2011; Wang *et al.* 2009; Zhang *et al.* 2009). In this section the combined use of TerraSAR-X and PALSAR will be investigated using the TACL model applying texture analysis.

## **6.4 Methodology**

### **6.4.1 Data Used**

In the current Section the following SAR data covering the study area were used: TSX data of 31/05/2010 and 17/06/2010 and ALOS PALSAR (31/05/2010). In addition, a further image, termed Mean-TSX image, has been computed which contains the mean pixel intensities of both TSX images. The used data were rescaled to 5 bits (32 grey levels). During the acquisition dates, the following land-cover classes were mapped in the field: cereal, maize, rape, grass and orchard.

Both training and reference data were assigned to the attribute table of the plot shape file.

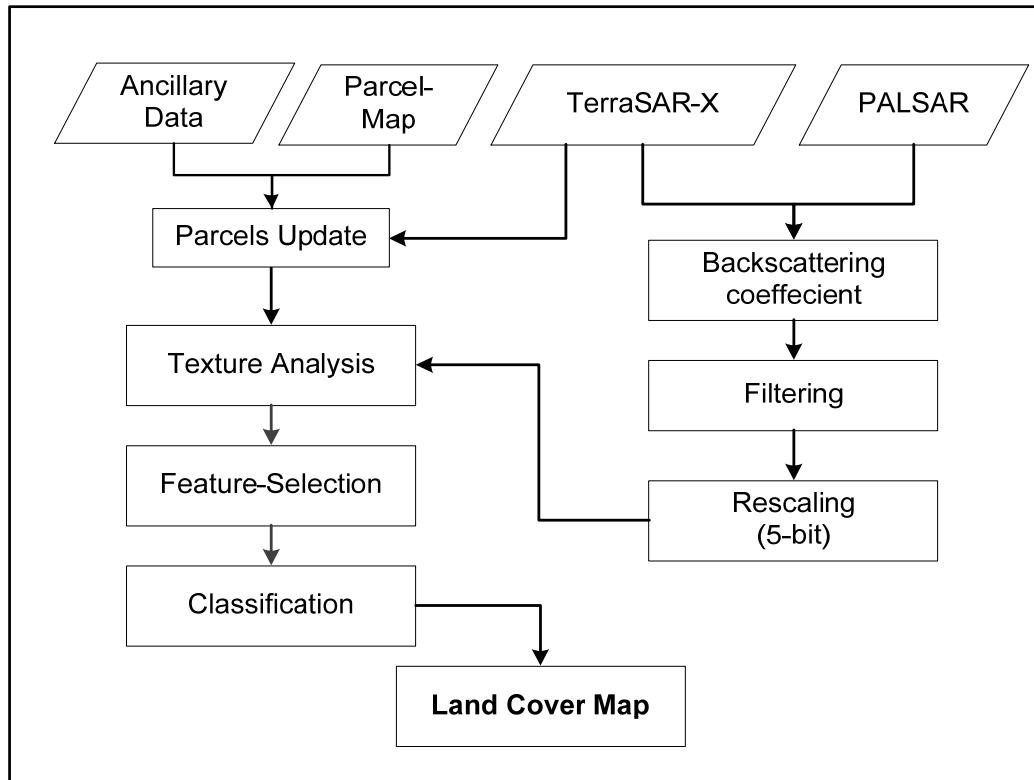


Figure 6.1. Methodological flowchart.

#### 6.4.2 Feature Extraction and Classification

The TACL Model was used in the proposed order to define the proper texture features separating between different land-cover classes (using representative samples for each land-cover type) and applying those features to all parcels. The separability values were used as a guide to calculate the texture features of all classes using the proper images and direction-distance combinations. All calculated features are stored in one attribute table, which enables further flexible selection for single-image attributes or various combinations within which the feature selection methods were utilised. The classification was applied to the images in a single and combined way. Figure 6.1 illustrates the methodological flowchart adapted in this study.

## **6.5 Results and Discussion**

### **6.5.1 Comparison between Different Grey Scales**

The backscattered images were rescaled into 32, 64, 128 and 256 grey-level using 2 and 3 standard deviations of the original image (backscattered images). The results of separability for each case were compared. In general, the rescaled data using 2 standard deviations revealed a higher separability for some texture features than when using 3 standard deviations (Table C.1, in Appendix C). The grey-scale comparison is illustrated in section 4.7.1.

### **6.5.2 Comparison between DTM and GIM in Backscattering Calculation**

A subset of the TSX image from 31/05/10 was used in this comparison where the backscattering coefficient was calculated in two ways: using the DTM (2m) and using the GIM file of the mentioned image. The backscattered images were rescaled into 8 bits (256 grey-level) using 2 standard deviations. Then the separability values (Table C.2) were calculated for all class-pairs of both images. The results show that the separability values are quite similar in both cases. Therefore, the GIM method is used for further analysis.

### **6.5.3 Separability Values**

As shown in Table C.3, in the case of the TSX image of 31/05/2010, the separability values for different class pairs indicate that there will be mixed classes. For example, for rape-orchard, maize-orchard and maize-rape the separability values are poor. Therefore, there will be a mixed classification among these pairs. The TSX image of 17/06/2010 revealed better separability values in the case of rape-orchard and maize-rape, but still low for maize-orchard. Accordingly, a combined use of both images can improve the classification accuracy. On the other hand, PALSAR (HV) has, in general, higher separability values than the HH polarisation (Table C.4). For example, rape-cereals and cereal-orchard are not well separated in HH; also maize-cereal is not well separated in HV. Therefore, using each single band will result in a mixed classification, while using both bands together improves the classification accuracy.

## **6.6 Classification Results**

The most suitable features for classification were defined using the feature selection methods available in the model. According to the separability values in case of TSX (31/05/2010), the land cover could be classified into three classes: cereals/grass, rape/maize and orchards. Therefore, using more sources of information, such as multi-temporal or multi-frequency data, improves the classification accuracy in addition to the multi-feature approach of the proposed TACL model. This model facilitates the investigation of combining different feature-sources and their performance in classification process. The following are examples of such combinations where the SVM approach is selected as the classification method.

### **6.6.1 Multi-Date Example**

In the multi-date approach the texture features of TSX 31/05/2010, 17/06/2010 and Mean-TSX images (with a total number of 324 features) were tested for classification. Different numbers of features were selected using feature selection methods and tested with respect of classification accuracy. The best performance was reached when using 80 features where the overall accuracy was 88.05% with a kappa value of 77.74% (Table 6.1). Figure 6.2a shows the obtained land cover map.

### **6.6.2 Multi-Frequency Example**

The joint use of TerraSAR-X (HH) and PALSAR (HH) was also evaluated. The results show that, using features of both images, improved the classification accuracy, as all classes could be separated in a better way (Figure 6.2b), since the behaviour of different land-cover types differs according to the used frequency. In this example, only PALSAR (HH) polarisation is used with TerraSAR-X (HH) to investigate the combination of two different frequencies. The total number of features for both data types is 277 and the classification was applied using 155 selected features. The overall accuracy lies at 87.29% with a kappa value of 83.49% (Table 6.2).

On the other hand, the same procedure was applied to combine features of TSX (31/05/2010) with features of ALOS PALSAR (HV). With 100 selected features the

classification accuracy reached 88.98% with a kappa value of 85.67% (Figure 5.2c). This slight improvement can be attributed to the fact that the HV polarisation is more sensitive to the vegetation.

### 6.6.3 Multi-Polarisation Example

The classification results of the PALSAR image both HH and HV polarisation show lower accuracy than when using two TSX images. This can be attributed to the higher resolution of TSX data, In addition to the higher texture-information contained in the TSX image. The total number of used features of PALSAR (HH/HV) is 253 from which 100 features were selected for classification. The obtained accuracy was 77% with a kappa value of 70% (Figure 6.2d).

### 6.6.4 Multi-Frequency/Multi-Polarisation Example

The combination of different features from both TSX of 31/05/2010 and ALOS PALSAR (HH/HV) from 31/05/2010 was also investigated. A total number of 349 features were used. This combination achieved higher classification accuracy. Using 110 selected features resulted in overall accuracy of 91.5% with a kappa value of 88.97% (Table 6.3). The corresponding land-cover map is shown in Figure 6.3.

Table 6.1. Overall classification accuracy statistics using features of TSX imagery of 13/05/2010, 17/06/2010 and Mean-TSX.

Classified Data	Reference Data					Sum.
	Cereals	Grass	Maize	Orchard	Rape	
Cereals	41	0	0	0	0	41
Grass	2	11	1	0	2	16
Maize	0	2	18	2	5	27
Orchard	0	0	1	8	2	11
Rape	0	0	0	3	20	23
<b>Sum.</b>	43	13	20	13	29	<b>118</b>
<b>Accuracy</b>						
Producer	95%	85%	90%	62%	69%	
User	100%	69%	67%	73%	87%	
Kappa	100%	65%	60%	69%	83%	
$k_{hat}$	77.74%					
<b>Overall</b>	<b>83.05%</b>					

Table 6.2. Overall classification accuracy statistics using features of TSX imagery of 13/05/2010 and ALOS PALSAR (HH) of 31/05/2010.

	Reference Data					
Classified Data	Cereals	Grass	Maize	Orchard	Rape	Sum.
Cereals	35	6	0	0	0	41
Grass	2	13	0	0	1	16
Maize	0	2	25	0	0	27
Orchard	0	0	0	9	2	11
Rape	0	0	0	2	21	23
<b>Sum.</b>	<b>37</b>	<b>21</b>	<b>25</b>	<b>11</b>	<b>24</b>	<b>118</b>
<b>Accuracy</b>						
Producer	95%	62%	100%	82%	88%	
User	85%	81%	93%	82%	91%	
Kappa	79%	77%	91%	80%	89%	
$k_{hat}$	83.49%					
<b>Overall</b>	<b>87.29%</b>					

Table 6.3. Overall classification accuracy statistics of using features of TSX imagery of 31/05/2010 and ALOS PALSAR (HH/HV) of 31/05/2010.

	Reference Data					
Classified Data	Cereals	Grass	Maize	Orchard	Rape	Sum.
Cereals	38	3	0	0	0	41
Grass	1	13	0	1	1	16
Maize	0	3	23	1	0	27
Orchard	0	0	0	11	0	11
Rape	0	0	0	0	23	23
<b>Sum.</b>	<b>39</b>	<b>19</b>	<b>23</b>	<b>13</b>	<b>24</b>	<b>118</b>
<b>Accuracy</b>						
Producer	97%	68%	100%	85%	96%	
User	93%	81%	85%	100%	100%	
Kappa	89%	78%	82%	100%	100%	
$k_{hat}$	88.98%					
<b>Overall</b>	<b>91.53%</b>					

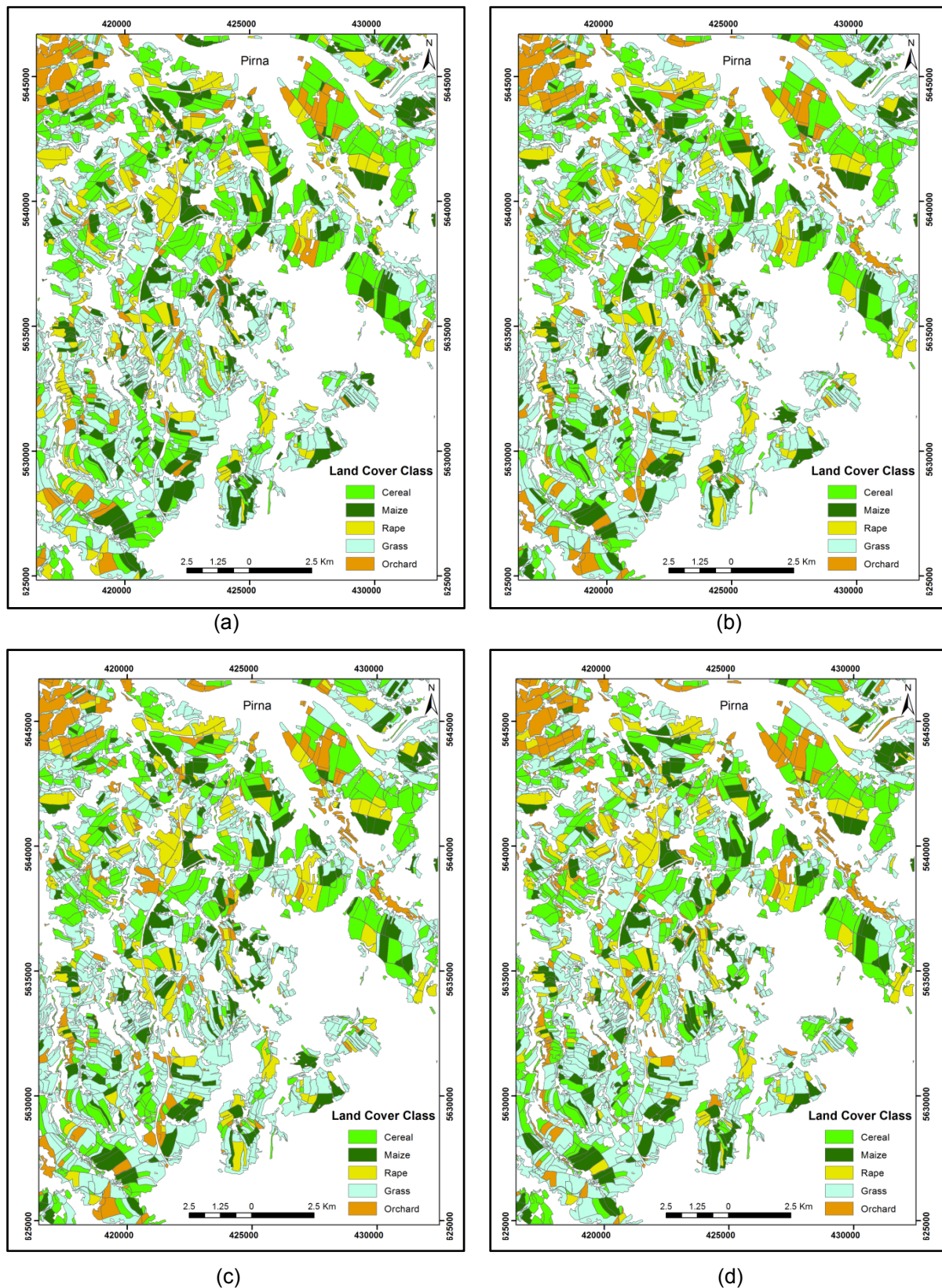


Figure 6.2. Land cover map of the study area using a) TSX imagery of 31/05/2010 and 17/06/2010, b) TSX and PALSAR HH of 31/05/2010, c) TSX and PALSAR HV of 31/05/2010 and d) PALSAR HH/HV acquired on 31/05/2010.

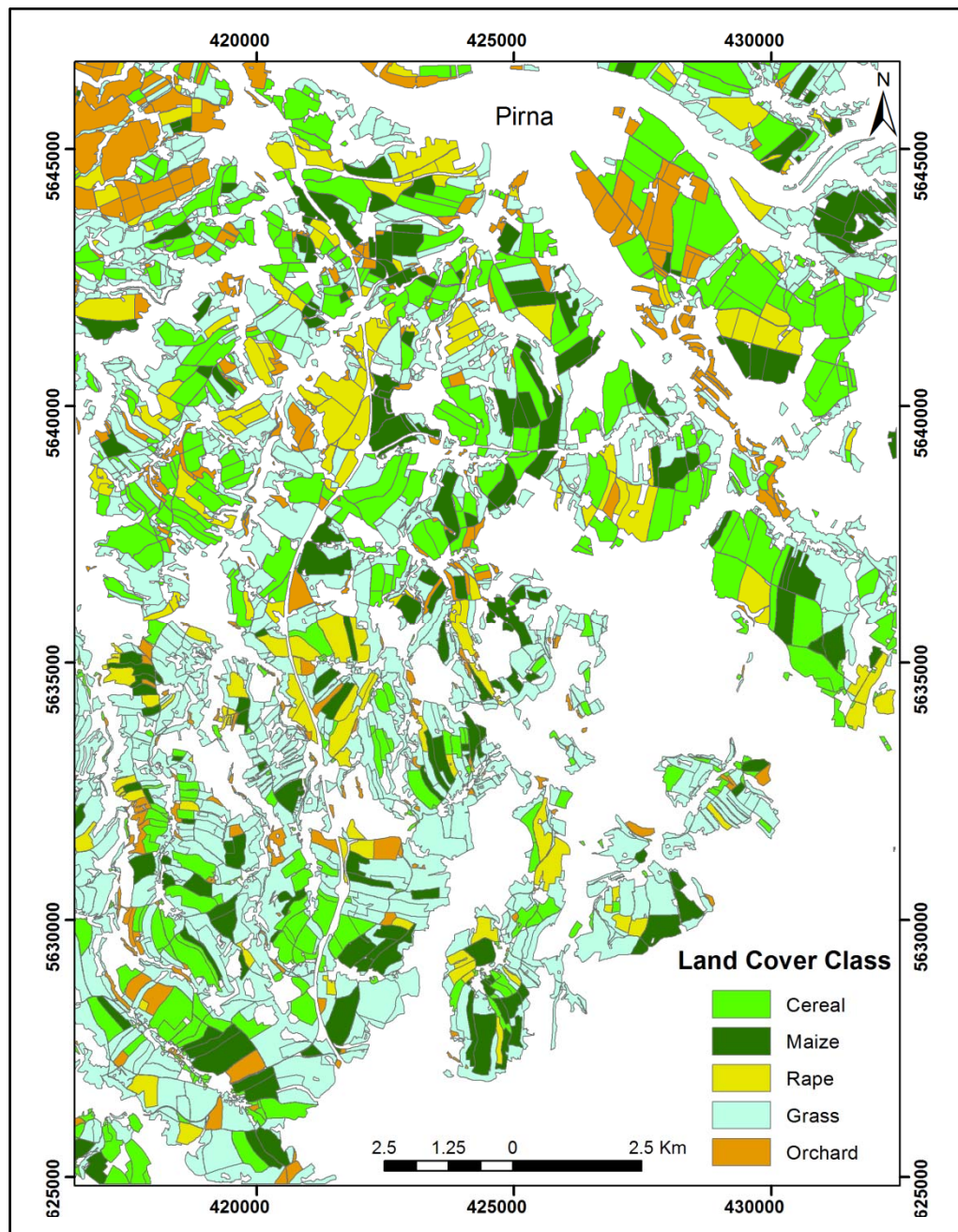


Figure 6.3. Land cover map of the study area using TSX and PALSAR HH/HV of 31/05/2010.

As shown in Figure 6.2, using both TSX of 31/05/2010 and 17/06/2010 achieved higher accuracy for cereal than other combinations. However there is a mixed classification between maize and rape. Using TSX of 31/05/2010 and PALSAR (HH) improved the separation between maize and rape, but the accuracy of the cereal is decreased. In Figure 6.3, using TSX of 31/05/2010 and PALSAR (HH+HV) achieved higher overall accuracy (91.53%) than the combinations in Figure 6.2.

## 6.7 Conclusions

In the current study, combinations of different features extracted from multi-temporal TSX data and single-date ALOS PALSAR imagery were investigated for land-cover classification. The combined use of TSX and ALOS PALSAR (HH), as a multi-frequency approach, improved the LCC accuracy. The improvement was higher when using two TSX images of different dates or using PALSAR HH and HV polarisations. The TACL model provided a flexible selection of various features, in addition to the potential of dealing with a large amount of features. Multi-dimensional SAR data proved to possess a high potential for land-cover classification (LCC). The findings of the study serve as a testimony of the applicability of multi-sensor SAR images for improving the classification accuracy.

## 7 Soil Moisture Mapping using TerraSAR-X Data

### 7.1 Introduction

Soil Moisture (SM) is important for various applications like crop-water management and hydrological modelling. For example, it is required as an important input to crop development models to set the initial conditions in the spring (Henderson *et al.* 1998). The deficit or surplus of soil moisture is often the key indicator of natural disaster events, such as drought and flood (Du, Shi & Sun 2010), as soil moisture data is a critical state variable of the watershed in assessing flood hazards (Henderson *et al.* 1998).

In situ soil-moisture measurements are invaluable for calibrating and validating land surface models and satellite-based soil moisture retrievals (Dorigo *et al.* 2011). Soil moisture mapping over a large area requires a lot of equipment and intensive field work. Therefore, active remote sensing can be applied in soil moisture mapping to overcome such problems (Ulaby, Aslam & Dobson 1982). Microwave remote sensing is able to provide quantitative information about surface soil moisture, particularly in the low-frequency microwave region from 1 to 10 GHz (Schmugge 1983).

Soil moisture can be studied at two spatial scales: regional or global scale and an agricultural field plot scale approximately between 0.01 and 0.5 km<sup>2</sup>. At the regional scale, different studies attempted to neglect the influence of roughness on soil moisture and proposed a linear relationship between surface moisture and backscattered radar signals with uncertainty of approximately 0.04 cm<sup>3</sup>.cm<sup>-3</sup>. While at the scale of an agricultural field, the roughness effect cannot be neglected (Anguela *et al.* 2010). Different studies have focused on coupling the data from different configurations in order to retrieve roughness and moisture simultaneously. Other analyses implement an approach involving the detection of changes while making the hypothesis that one parameter is stabilized (Anguela *et al.* 2010). Ulaby *et al.* (1978) demonstrated that the influence of surface roughness

decreases with increasing radar frequency (Ulaby, Batlivala & Dobson 1978). The dynamics of the relationship between the radar signal and roughness parameter are stronger in the L-band than in the C- and X-bands (Baghdadi *et al.* 2008a; Ulaby, Moore & Fung 1986) Moreover, SAR data are more sensitive to soil roughness at high incidence angles (Baghdadi *et al.* 2008a; Baghdadi *et al.* 2008b; Zribi & Dechambre 2003).

Aubert *et al.* (2011) concluded that for agricultural bare plots, the effects of soil roughness on the TerraSAR-X signal are small and function of the moisture content. Moreover, The results demonstrates that the SAR signal in the X-band is slightly more sensitive to soil moisture at a low incidence angle (25°), but soil-moisture mapping can be carried out with either low or high incidence angles, because both showed high sensitivities. And the sensitivity of the radar signal to soil moisture appears to be higher in the X-band than in the C-band, regardless of the incidence angle (Aubert *et al.* 2011).

Soil moisture extraction has been investigated using various SAR data sources. Paloscia *et al.* (2010) confirmed the sensitivity of C-band data (ENVISAT/ASAR) to SMC even in heterogeneous landscapes with soil covered by dense grass. Merzouki *et al.* (2011) investigated the potential of C-band RADARSAT-2 in combination with local autocorrelation statistics to estimate near-surface soil moisture. They concluded that the spatial soil moisture pattern was clearly captured (Merzouki, McNairn & Pacheco 2011). Several studies investigated the L-band SAR data for soil moisture mapping (Kasischke *et al.* 2011; Mattia *et al.* 2009). X-band data has been applied in several studies indicating their potentiality in soil-moisture mapping for bare fields and specific conditions of vegetated area. Kseneman *et al.* (2011) used Spotlight TerraSAR-X data for soil moisture mapping for bare soils and vegetated areas, obtaining well estimated results (Kseneman, Gleich & Cucej 2011).

In fact, the speckle effects and low resolution (between 10 and 30 m) of the first-generation SAR data (ERS, RADARSAT-1 and ASAR) prevented the analysis of small-scale variations. The high spatial resolution of the TerraSAR-X sensor (1 m) provides access to soil-surface heterogeneities at a finer scale (Aubert *et al.* 2011).

The current Section (soil moisture extraction) represents a continuous work on a joint project to investigate the potentiality of TSX and ALOS PALSAR data for soil moisture mapping. The first results considered both SAR data types (Elbially 2011). The current work investigates only the TSX data, where an additional TSX imagery (on 18/04/2011) was acquired. Furthermore, selection of optimum linear-regression equations takes into consideration the coefficient of determination ( $R^2$ ) value besides the ENL and visual evaluation of filtered images, as explained below.

## **7.2 Data Used and Methodology**

### **7.2.1 Data Used**

The data preparation and processing are explained in Section 3. The data used in this section are:

- TerraSAR-X data namely; TerraSAR-X imagery acquired on 31/05/2010, 17/06/2010 and 18/04/2011.
- DTM-based Backscattering coefficient image of TerraSAR-X imagery acquired on 31/05/2010.

### **7.2.2 Field Work**

#### **TDR Measurements**

Synchronise soil moisture measurements were applied around the acquisition time using TDR instrument. For each sampling plot, two perpendicular sampling sections were applied with total number of 8–12 measurements for the first 5 cm of the surface layer. These measurements were filtered to exclude the strange values (outliers), and then the mean and standard deviation were calculated. The obtained mean is assigned to the representative sampling-point (Figure 7.1) for the further processes.

#### **Soil-Moisture Sampling**

Laboratory measurements for volumetric soil moisture were conducted to validate the TDR measurements. This validation yielded Route Mean Square Error (RMSE) of 0.98 %. Soil core sampler (with height of 5 cm, and diameter of 5 cm) was used

to collect relatively undisturbed soil samples for soil moisture measurement. And then gravimetric soil moisture content was determined and converted to volumetric soil moisture content. These calculations can be explained as following:

$$\text{Gravimetric Soil Moisture} = \frac{\text{mass of water}}{\text{mass of oven - dried soil}}$$

$$\text{Volumetric Soil Moisture} = \text{gravimetric soil moisture} * \text{soil bulk density}$$

## **Soil Roughness**

Due to some technical limitations, soil roughness has not been investigated. However, a recent study by Aubert *et al.* (2011) found that for agricultural bare plots, the effects of soil roughness on the TerraSAR-X signal are small and function of the moisture content.

### **7.2.3 Data Processing**

#### **7.2.3.1 Speckle Reduction**

Two different approaches were applied:

- a) Starting with applying different filters then calculating the backscattering coefficient for each filtered image,
- b) Starting with calculation of the backscattering coefficient then applying different filters.

The results of both sequences were compared to find out the highest correlation between measured soil moisture and backscattering ( $\sigma^0$ ); then the best approach was defined. The decision was made according to: the ENL of the last product of each approach, the coefficient of determination ( $R^2$ ) between the calculated  $\sigma^0$  values and the measured  $SMv$  data, in addition to the visual evaluation of the filtered images. The methodological flowchart is shown in Figure (7.2).

#### **7.2.3.2 Comparison between DTM and GIM for Backscattering Calculation**

This comparison was applied to the TSX image of 31/05/2010 where the backscatter coefficient was calculated using DTM (2m) and GIM file accompanied with the mentioned TSX image. The image was filtered using different filters and

kernel sizes (3x3, 5x5 and 7x7), then the coefficient of determination  $R^2$  was determined in each case (Table D.1).

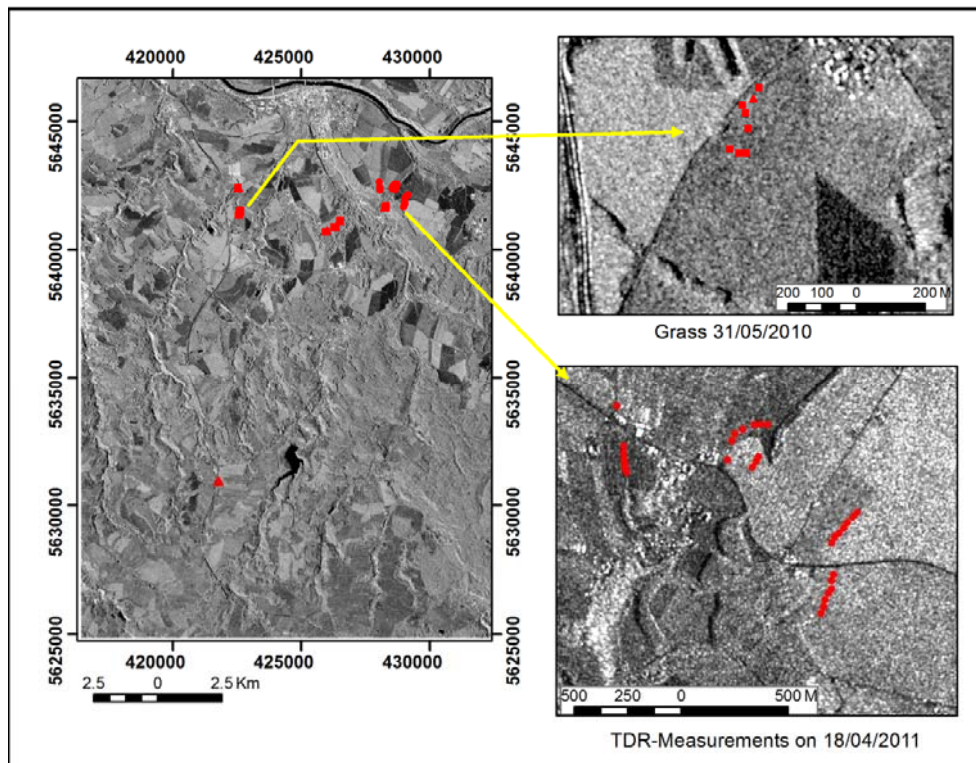


Figure 7.1. TDR measurements collected during the field work.

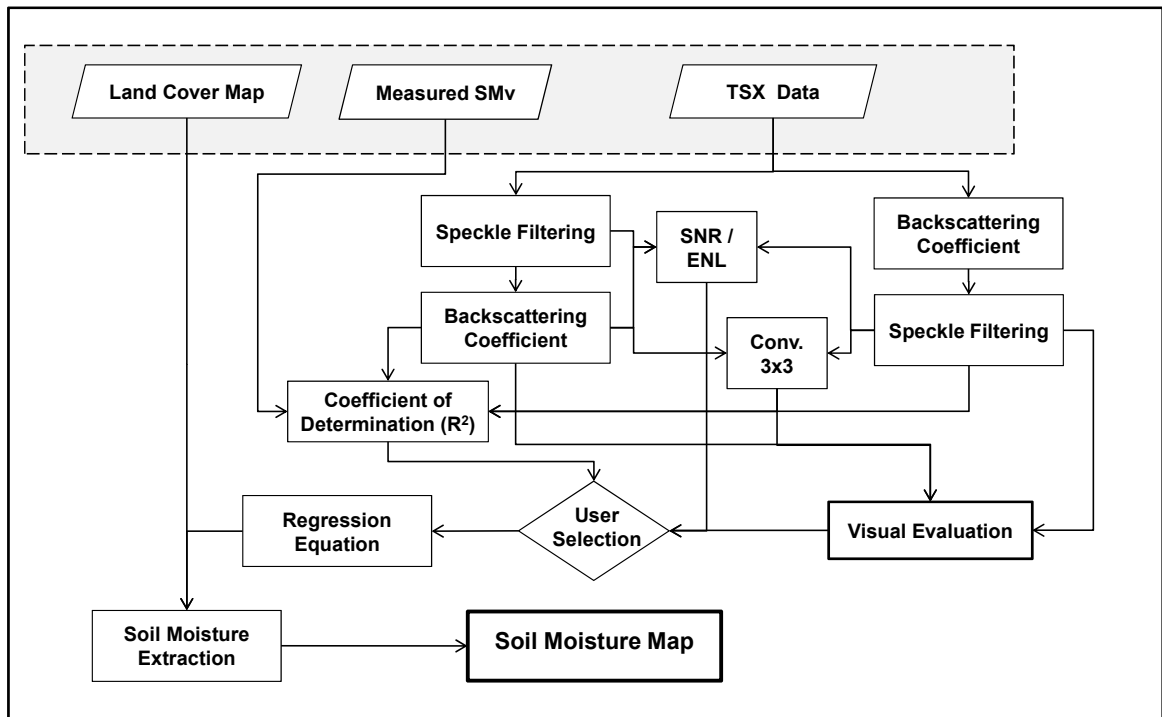


Figure 7.2. Methodological flowchart.

### 7.2.3.3 Extracting the Backscattering Values

The obtained backscattering images from the above mentioned approaches were used to extract the sigma naught values which represent the collected samples. These images were used directly to extract the sigma naught values. In addition, the mean (convolution 3x3) of backscattering image was calculated, and then sigma values were extracted to the corresponding sampling point. This process was applied using the ArcGIS spatial analyst module (extract multi value to point).

## 7.3 Results and Discussion

### 7.3.1 DTM and GIM for Backscattering Calculation

The coefficient of determination  $R^2$  values (Table D.1, in Appendix D), as an indicator to compare DTM and GIM for Backscattering Calculation, show almost no significant variation between these two methods under the conditions of the studied agricultural area. However, using the higher resolution DTM provided more details in undulated areas. In the current study, the GIM data were used in backscatter coefficient calculation of TSX data.

### 7.3.2 Effect of Speckle Reduction on Backscattering

As shown in Tables D.1 and D3 there are significant differences in  $R^2$  values according to the applied filtering parameters (type and kernel size). The soil moisture is measured in sampling plots (represented as points) and it has some kind of heterogeneity within the same field. Whereas the speckle reduction will be followed by quantitative image analysis using point targets, therefore, speckle filtered images must retain relative gain levels of mean reflectivity, and of impulse responses (Henderson *et al.* 1998). For the tested filters (Tables D.1 and D3) the  $R^2$  values varies independently of the SNR and ENL (Tables D.2 and D4). Therefore, selection of filtered image will be according to  $R^2$  value, in addition to the visual evaluation of the image.

TSX (31/05/2010) achieved high  $R^2$  value using median filter (5x5) with and without convolution mean (3x3). However the smoothed one has lower  $R^2$  value (0.873) than non-smoothed one with  $R^2$  value of 0.935, the smoothed one is

selected for further analysis according to the visual interpretation. Whereas the non-smoothed one shows the pixel values to be rounded to the integer values.

### 7.3.3 Soil Moisture Extraction

The proper filtered images for soil moisture extraction were selected. Then, jointly with the measured soil moisture values (Table 7.1) were used to calculate the parameters of the linear regression equations (Table 7.2). These equations were subsequently used to calculate the soil moisture for each corresponding area (land cover class). ERDAS imagine is used to achieve this process with the aid of the land cover map of the study area (which is obtained in Section 6). Figure 7.3 shows the soil moisture distribution over the study area for the studied two land cover classes. This pixel based map can be used as an input for some modelling process.

Table 7.1. Measured soil moisture, extracted sigma naught and The  $R^2$  values for TSX imagery acquired on 31/05/2010 and 17/06/2010.

Sample Nr.	31/05/2010				17/06/2010	
	Early growing maize		Grass		Early growing maize	
	SM <sub>v</sub> %	Sigma0	SM <sub>v</sub> %	Sigma0	SM <sub>v</sub> %	Sigma0
1	17.73	-9.111	43.85	-11.333	18.12	-10.222
2	17.98	-8.889	39.91	-13.111	22.04	-9.889
3	17.48	-8.889	40.23	-12.000	18.81	-9.000
4	16.41	-8.889	39.85	-12.000	13.28	-11.111
5	15.17	-10.333	39.76	-12.222	11.27	-12.667
6	17.78	-9.000	39.86	-13.000	19.60	-9.556
7	21.69	-7.444			28.86	-7.778
8					32.65	-7.222
<b>R<sup>2</sup></b>	<b>0.873</b>		<b>0.495</b>		<b>0.885</b>	

Table 7.2. Regression equations for TSX acquired on 31/05/2010 and 17/06/2010.

TSX	Land cover	Regression equation
31/05/2010	Early growing maize	$m_v = 2.233 \sigma^\circ + 37.71$
31/05/2010	Grass	$m_v = 1.685 \sigma^\circ + 61.27$
17/06/2010	Early growing maize	$m_v = 3.888 \sigma^\circ + 58.21$

Moreover, the plot- boundary map or catchment/sub-catchment map can be used to calculate different statistics (i.e. average) of soil moisture distribution for each plot or catchment/sub-catchment respectively. TSX image acquired on 17/06/2010 with lower looking angle performs better than TSX of 31/05/10. This is clear in Table D.3 where the  $R^2$  values in general are higher in comparison to the TSX of 31/05/2010 for different filtering parameters. However, in case of the early growing maize fields, the  $R^2$  value increased only by 0.012. This can be attributed to the difference in the plant parameters due to the degree of growth that occurred between the two acquisition dates (Appendix E-1). While the crop parameters and crop management are still enables the X-band to reach the soil surface.

The TSX imagery of 18/04/2011 shows various land cover classes (bare-soil, early growing maize, cereal, grass, rape and orchard) from which the bare-soil and early growing maize expressed high values of  $R^2$ , while cereal and grass showed lower values of  $R^2$ . These four classes (Appendix E-2) were represented by in-situ soil-moisture measurements (Table 7.3) and the corresponding linear regression equations were calculated (Table D.3). According to  $R^2$  values and the visual evaluation of the filtered images, two filters were selected as shown in Table 7.4. These two filters are the convolution (3x3) of: median 3x3 and median 5x5. The obtained equations were applied to each corresponding image and then by applying the conditional-statement, they were grouped in one image representing soil moisture for the studied land cover classes (Figure 7.4).

Table 7.3. Measured soil moisture, extracted sigma naught and The  $R^2$  values for TSX imagery acquired on 18/04/2011.

Sample Nr.	Bare-soil		Early growing maize		Cereal		Grass	
	SM <sub>v</sub> %	$\sigma^\circ$	SM <sub>v</sub> %	$\sigma^\circ$	SM <sub>v</sub> %	$\sigma^\circ$	SM <sub>v</sub> %	$\sigma^\circ$
1	23.97	-8.889	21.37	-9.000	27.64	-16.111	39.943	-9.778
2	24.34	-9.000	23.38	-8.111	27.60	-15.556	38.340	-13.556
3	22.49	-11.778	25.92	-8.000	27.33	-14.889	37.533	-12.333
4	24.41	-7.556	21.76	-9.222	27.80	-13.667	38.460	-12.444
5	22.73	-11.111	21.73	-9.333	27.54	-15.333	38.517	-13.111
6	23.37	-10.889	19.25	-9.667	25.74	-17.000		
<b>R<sup>2</sup></b>	<b>0.892</b>		<b>0.836</b>		<b>0.513</b>		<b>0.569</b>	

The obtained soil moisture map is a raster format which can be used as input for specific modelling. Various statistics can be applied to the raster image as required. For example, the average of soil moisture can be calculated for each plot (Figure 7.5) or any areal features, i.e. sub-catchments.

Table 7.4. Regression equations for TSX acquired on 18/04/2011 and the corresponding filtered image.

Land cover	Regression equation	image
Bare-soil fields	$m_v = 0.4761 \sigma^\circ + 28.251$	Median 3x3_conv3
Early growing maize	$m_v = 3.0016 \sigma^\circ + 48.916$	Median 5x5_conv3
Cereal	$m_v = 0.4875 \sigma^\circ + 34.795$	Median 3x3_conv3
Grass	$m_v = 0.4473 \sigma^\circ + 44.036$	Median 3x3_conv3

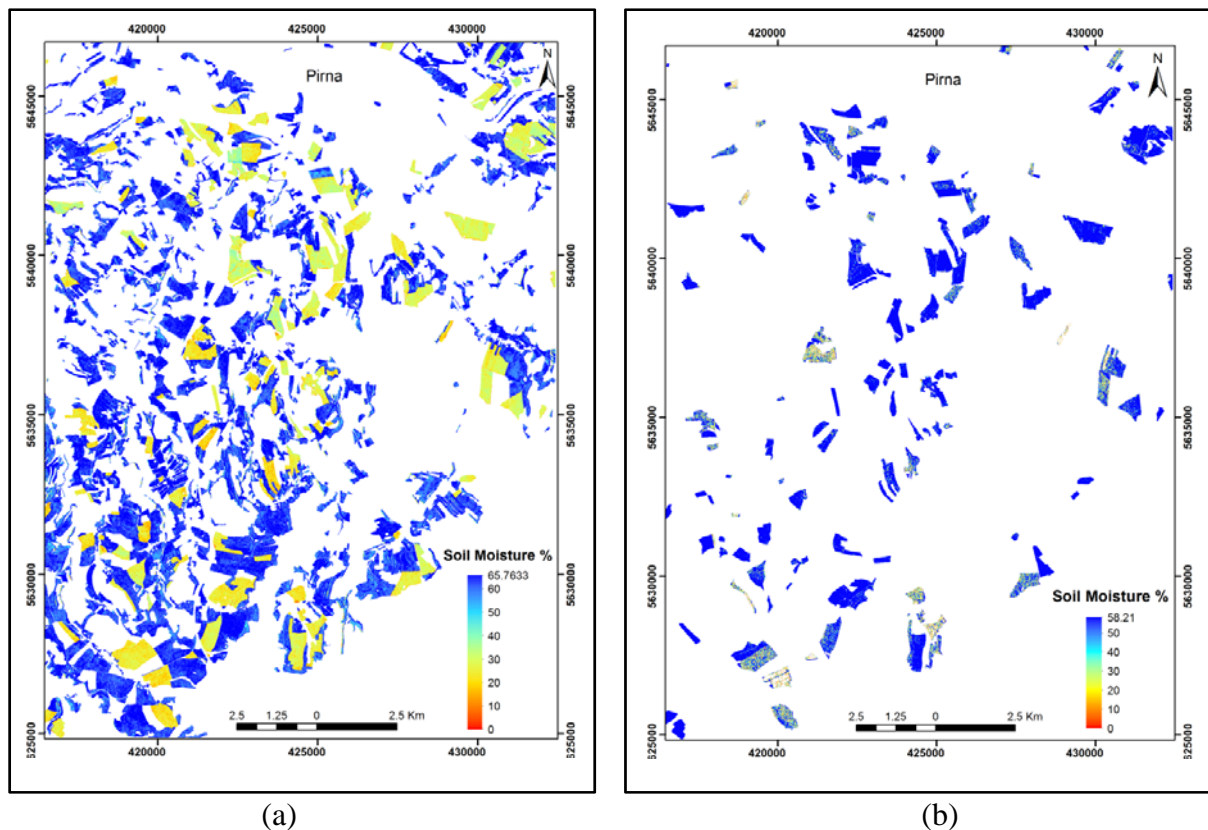


Figure 7.3. The extracted volumetric soil-moisture over the study area; a) on 31/05/2010 for early growing maize and grass, and b) on 17/06/2010 for early growing maize.

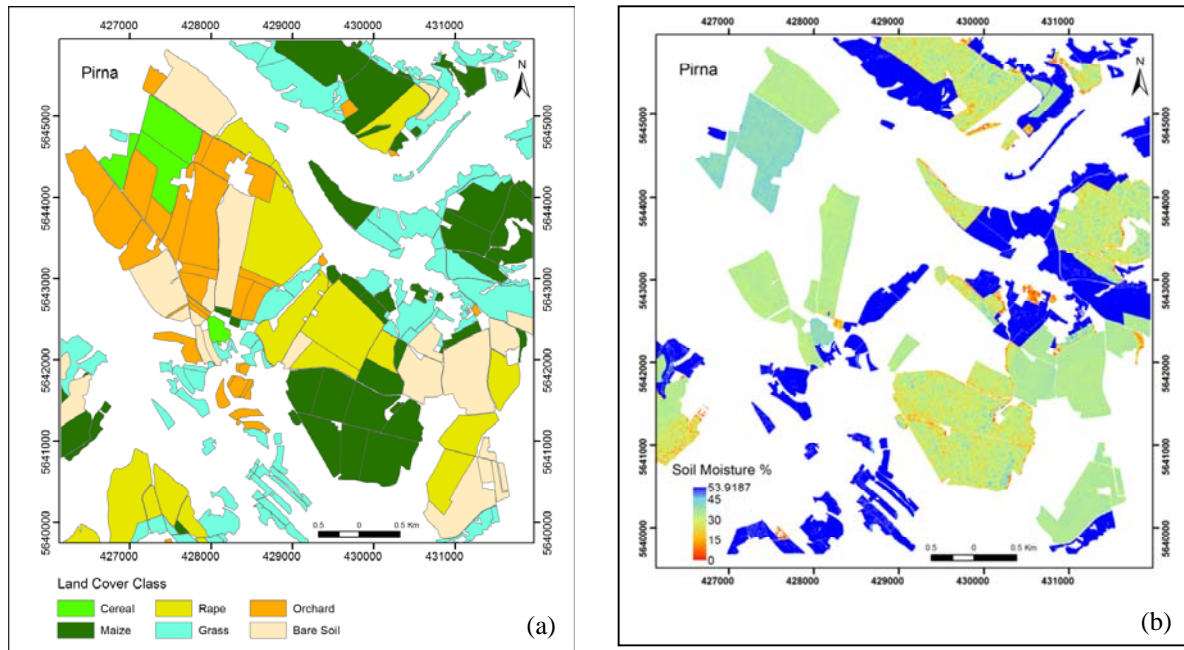


Figure 7.4. a) Land-cover map, and b) Extracted volumetric soil-moisture using a subset of the TSX image acquired on 18/04/2011.

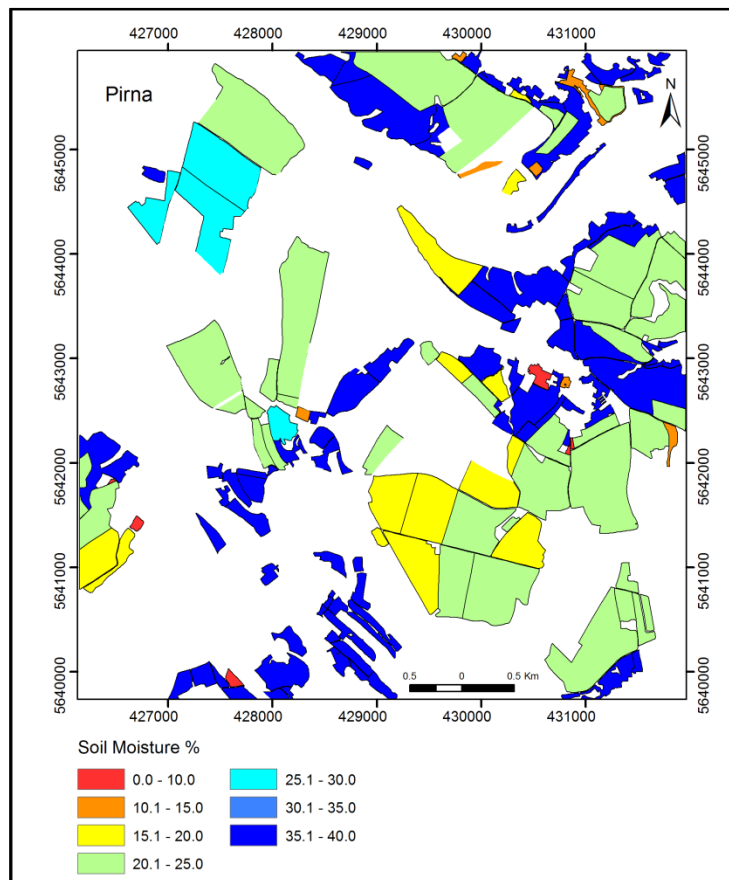


Figure 7.5. Average of volumetric soil-moisture at the plot level on 18/04/2011.

## 7.4 Conclusion

Soil moisture is important for various applications like crop-water management and hydrological modelling. In this section, the TerraSAR-X imagery were utilised to map the soil-moisture over the study area. In-situ measurements simultaneous with the acquisition time were conducted. The effect of different speckle filters was studied. In order to find the proper filtering parameters, three criteria were taken into consideration. These criteria are; the SNR and ENL, the coefficient of determination  $R^2$  between the calculated  $\sigma^0$  values and the measured *SM* data, and the visual evaluation of the image. The results demonstrated that the  $R^2$  values are good indicator in addition to the final visual evaluation. The TSX imagery expressed high  $R^2$  values for bare-fields and early-growing maize. For example, TSX image of 18/04/2011 achieved  $R^2$  value of 0.89 for the bare fields and 0.84 for the early-grown maize. These results proved the potential use of TSX imagery in soil moisture mapping at the field scale.

## 8 Conclusions and Outlook

### 8.1 Conclusions

A plot-based texture-analysis and classification model has been developed supporting the combination of different directions and distances for texture analysis and various classification methods. The model has been tested and applied to the TerraSAR-X and ALOS PALSAR data. On the other hand TerraSAR-X imagery were utilised for soil moisture mapping. The following conclusions can be drawn from the present study.

- Full flexibility is offered by the developed software solution with respect to features, directions, and distances associated to texture, whilst the performance of all members of the calculated feature space can be evaluated and reduced to a best-performing subset, in addition to the potential of dealing with large amounts of features for the classification process.
- The results indicate that multi-distance texture analysis enhanced the separability between some classes. Utilizing feature selection methods proved to be efficient in data reduction and improving the classification accuracy. Moreover, since all classification input is derived from the attribute tables, the feature space can eventually be extended to sources different from imagery (terrain parameters etc.).
- The performance of different filters to enhance separability varies according to the land-cover type. Thus, in case of few numbers of images, extracting multi-features from different filtered images will increase the classification accuracy.
- Various classification approaches are available and can flexibly react on different data distributions associated with the individual features. The results showed that for the current datasets, support-vector machine classification-method performs better than KNN and ANN.
- Combinations of different features extracted from temporal TSX data and a single ALOS PALSAR image were investigated. Using two different acquisitions of TSX

achieved an overall accuracy of 83%, while using TSX imagery (X-band) with a nearly synchronous PALSAR imagery (L-band) revealed an accuracy of 88.98%. Thus, multi-dimensional SAR data proved to have a high potential for land-cover classification (LCC). These findings serve as a testimony of the applicability of multi-sensor SAR images for improving the classification accuracy.

- Land-cover classification using two different acquisition dates of TSX achieved an overall accuracy of 83%, while using TSX imagery (X-band) with a nearly synchronous PALSAR imagery (L-band, HH/HV) revealed an accuracy of 91.53%.
- TerraSAR-X proved to be efficient for soil moisture mapping. The results revealed a high sensitivity of X-band to surface soil-moisture, where the obtained coefficient of determination  $R^2$  reached values about 0.885 for an early growing corn field.
- The  $R^2$  values vary significantly according to the filtering parameters and independently of the signal-to-noise ratios. Therefore, further studies are needed to investigate and improve the filtering techniques for point-target image analysis.

## 8.2 Outlook

In addition to some general recommendations, some functional additions to the software are yet desirable:

- The choice for the potentially most suitable classifier might be guided by extended software functionality in the form of an expert system. This will require an analytical handling of the specific properties of the feature space after each model run.
- Further work needs to be done to establish the capability of the multi-classifier approach which will improve the overall accuracy through using the benefits of different classifiers.
- The so far developed software might help in gaining more knowledge about the information content of high-resolution SAR imagery in relation to the acquisition date. Using a time-series comprising phenological stages from late winter until harvest time might reveal variations of image texture due to cultivation measures and plant development. The prediction of an optimum data acquisition time is feasible.

- A further study could assess the contribution of soil roughness to the radar backscattering, trying to investigate modern techniques for soil roughness estimation.
- More research is needed to better understand the effect of speckle reduction techniques on land-cover and soil-moisture mapping.
- The developed model can be applied to different remotely sensed data and different regions. Therefore, further applications and suggestions are highly recommended.

## 9 References

- Alex, Z.C. & Behari, J. 1996. Complex dielectric permittivity of soil as a function of frequency, moisture and texture. *Indian Journal of Pure & Applied Physics*, 34, (5) 319-323.
- Alharthi, A. & Lange, J. 1987. Soil-Water Saturation - Dielectric Determination. *Water Resources Research*, 23, (4) 591-595.
- ALOS products 2007, *Information ALOS PALSAR products for ADEN users*, Reference: ALOS-GSEG-EOPG-TN-07-0001, Technical Note, ESA, 5-Apr-2007.
- Anguela, T.P., Zribi, M., Baghdadi, N., & Loumagne, C. 2010. Analysis of local variation of soil surface parameters with TerraSAR-X radar data over bare agricultural fields. *IEEE Transactions on Geoscience and Remote Sensing*, 48, (2) 874-881.
- Asner, G.P. & Heidebrecht, K.B. 2002. Spectral unmixing of vegetation, soil and dry carbon cover in arid regions: comparing multispectral and hyperspectral observations. *International Journal of Remote Sensing*, 23, (19) 3939-3958.
- Atkinson, P.M. & Tatnall, A.R.L. 1997. Neural networks in remote sensing - Introduction. *International Journal of Remote Sensing*, 18, (4) 699-709.
- Aubert, M., Baghdadi, N., Zribi, M., Douaoui, A., Loumagne, C., Baup, F., El Hajj, M., & Garrigues, S. 2011. Analysis of TerraSAR-X data sensitivity to bare soil moisture, roughness, composition and soil crust. *Remote Sensing of Environment*, 115, (8) 1801-1810.
- Baghdadi, N., Boyer, N., Todoroff, P., El Hajj, M., & Begue, A. 2009. Potential of SAR sensors TerraSAR-X, ASAR/ENVISAT and PALSAR/ALOS for monitoring sugarcane crops on Reunion Island. *Remote Sensing of Environment*, 113, (8) 1724-1738
- Baghdadi, N., Cerdan, O., Zribi, M., Auzet, V., Darboux, F., El Hajj, M., & Kheir, R.B. 2008a. Operational performance of current synthetic aperture radar sensors in mapping soil surface characteristics in agricultural environments: application to hydrological and erosion modelling. *Hydrological Processes*, 22, (1) 9-20.
- Baghdadi, N., Cresson, R., Todoroff, P., & Moinet, S. 2010. Multitemporal observations of sugarcane by TerraSAR-X images. *Sensors*, 10, (10) 8899-8919.
- Baghdadi, N., Zribi, M., Loumagne, C., Ansart, P., & Anguela, T.P. 2008b. Analysis of TerraSAR-X data and their sensitivity to soil surface parameters over bare agricultural fields. *Remote Sensing of Environment*, 112, (12) 4370-4379.

- Barber, D.G. & Ledrew, E.F. 1991. SAR sea ice discrimination using texture statistics - a multivariate approach. *Photogrammetric Engineering and Remote Sensing*, 57, (4) 385-395.
- Behari, J. 2005. *Microwave dielectric behavior of wet soils*. New York, Springer.
- Benz, U.C., Hofmann, P., Willhauck, G., Lingenfelder, I., & Heynen, M. 2004. Multi-resolution, object-oriented fuzzy analysis of remote sensing data for GIS-ready information. *ISPRS Journal of Photogrammetry and Remote Sensing*, 58, (3-4) 239-258.
- Bhatta, B. 2010. *Analysis of urban growth and sprawl from remote sensing data*, 1st ed. New York, Springer.
- Blaschke, T., Lang, S., & Hay, G.J. 2008. *Object-based image analysis - spatial concepts for knowledge-driven remote sensing applications*, 1st ed. New York, Springer.
- Boisvert, J.B., Gwyn, Q.H.J., Chanzy, A., Major, D.J., Brisco, B., & Brown, R.J. 1997. Effect of surface soil moisture gradients on modelling radar backscattering from bare fields. *International Journal of Remote Sensing*, 18, (1) 153-170.
- Borghys, D., Yvinec, Y., Perneela, C., Pizurica, A., & Philips, W. 2006. Supervised feature-based classification of multi-channel SAR images. *Pattern Recognition Letters*, 27, (4) 252-258.
- Bouman, B.A.M. 1991. Crop parameter-estimation from ground-based X-band (3-Cm Wave) radar backscattering data. *Remote Sensing of Environment*, 37, (3) 193-205.
- Brisco, B., Brown, R.J., Snider, B., Sofko, G.J., Koehler, J.A., & Wacker, A.G. 1991. Tillage effects on the radar backscattering coefficient of grain stubble fields. *International Journal of Remote Sensing*, 12, (11) 2283-2298.
- Buchroithner, M. 1993, "Cartographic information extraction from SAR images using filtering and textural analysis," *In SAR geocoding: data and systems*, G. Schreier, ed., Karlsruhe: Wichmann, pp. 353-372.
- Buchroithner, M.F. & Granica, K. 1997. *Applications of Imaging Radar in Hydro-Geological Disaster Management: A Review*. Remote Sensing Reviews, 16.
- Buiten, H.J. & Clevers, J.G.P.W. 1993. *Land observation by remote sensing: theory and applications* Yverdon, Switzerland, Gordon and Breach Science Publishers.
- Canty, M.J. 2009. Boosting a fast neural network for supervised land cover classification. *Computers & Geosciences*, 35, (6) 1280-1295.
- Carincotte, C., Derrode, S., & Bourennane, S. 2006. Unsupervised change detection on SAR images using fuzzy hidden Markov chains. *Ieee Transactions on Geoscience and Remote Sensing*, 44, (2) 432-441.

- Cheney, M., Borden, B., Conference Board of the Mathematical Sciences, & National Science Foundation 2009. *Fundamentals of radar imaging*, 79 ed. Philadelphia, Society for Industrial and Applied Mathematics.
- Chmielewski, F.M., Muller, A., & Kuchler, W. 2005. Possible impacts of climate change on natural vegetation in Saxony (Germany). *International Journal of Biometeorology*, 50, (2) 96-104.
- Chukhlantsev, A.A. 2006. *Microwave radiometry of vegetation canopies* Dordrecht, Springer.
- Cingolani, A.M., Renison, D., Zak, M.R., & Cabido, M.R. 2004. Mapping vegetation in a heterogeneous mountain rangeland using Landsat data: an alternative method to define and classify land-cover units. *Remote Sensing of Environment*, 92, (1) 84-97.
- Clark, P.E. & Rilee, M.L. 2010. *Remote sensing tools for exploration: observing and interpreting the electromagnetic spectrum*, 1st ed. New York, Springer.
- Coburn, C.A. & Roberts, A.C.B. 2004. A multiscale texture analysis procedure for improved forest stand classification. *International Journal of Remote Sensing*, 25, (20) 4287-4308.
- Cortez, P. Data mining with neural networks and support vector machines using the R/rminer Tool, *In Advances in data mining - applications and theoretical aspects, 10th Industrial Conference on Data Mining, LNAI 6171*, P. Perner, ed., Berlin, Germany: Springer, pp. 572-583.
- Crawley, M.J. 2007. *The R book*. Chichester, West Sussex, John Wiley & Sons.
- Dabrowska-Zielinska, K., Budzynska, M., Ciolkosz, A., Kowalik, W., & Bochenek, Z. 2010. The status of agricultural ecosystem examined by microwave data. *Acta Astronautica*, 67, (7-8) 721-730.
- Dalgaard, P. 2002. *Introductory statistics with R*, 2nd ed. New York, Springer.
- Damoiseaux, T. 2003. *Untersuchungen zum Einsatz von Flugzeug-InSAR in der Gebirgskartographie*. PhD (Dissertation). Dresden University of Technology.
- Daughtry, C.S.T., Ranson, K.J., & Biehl, L.L. 1991. C-band backscattering from corn canopies. *International Journal of Remote Sensing*, Vol. 12, (No. 5) 1097-1109
- Davidson, G., Ouchi, K., Saito, G., Ishitsuka, N., Mohri, K., & Uratsuka, S. 2006. Single-look classification accuracy for polarimetric SAR. *International Journal of Remote Sensing*, 27, (22) 5073-5080.
- de Matthaeis, P., Ferrazzoli, P., Schiavon, G., & Solimini, D. Crop type identification and biomass estimation by SAR, *In Geoscience and Remote Sensing Symposium, 1995. IGARSS '95. 'Quantitative Remote Sensing for Science and Applications', International*, pp. 957-959.

De Wit, A.J.W. & Clevers, J.G.P.W. 2004. Efficiency and accuracy of per-field classification for operational crop mapping. *International Journal of Remote Sensing*, 25, 4091-4112

Definiens AG 2007, *Definiens Developer 7 User guide*, URL: [www.definiens.com](http://www.definiens.com).

Del Frate, F., Schiavon, G., Solimini, D., Borgeaud, M., Hoekman, D. H., & Vissers, M. A. M. 2003, On the potential of multi-polarization and multi-temporal C-band SAR data in classifying crops, *In Geoscience and Remote Sensing Symposium, 2003. IGARSS '03. Proceedings. 2003 IEEE International*, pp. 2195-2196.

Delta-T 2005, *WET Sensor User Manual v1.3 (2005)*. Delta-T Devices Ltd. UK.

Demirican, A., Ramach, H., & Mauser, W. 1992, Extraction of plant and soil parameters from multi-temporal ERS-1 SAR data of the Freiburg test site., *In First ERS-1 Symposium*, pp. 631-639.

Dhar, T., Menges, C., Douglas, J., Schmidt, M., & Armston, J. Estimation of pasture biomass and soil-moisture using dual-polarimetric X and L band SAR - accuracy assessment with field data, *In Geoscience and Remote Sensing Symposium (IGARSS), 2010 IEEE International*, pp. 1450-1453.

Dobson, M.C., Kouyate, F., & Ulaby, F.T. 1984. A Reexamination of Soil Textural Effects on Microwave Emission and Backscattering. *IEEE Transactions on Geoscience and Remote Sensing*, 22, (6) 530-536.

Dobson, M.C., Ulaby, F.T., Hillikaines, M.T., & El-Rayes, M.A. 1985. Microwave dielectric behavior of wet soil- Part II: Dielectric Mixing Models. *IEEE Trans.Geo.&Remote Sens.*, GE-23, 35-46

Dorigo, W.A., Wagner, W., Hohensinn, R., Hahn, S., Paulik, C., Xaver, A., Gruber, A., Drusch, M., Mecklenburg, S., van Oevelen, P., Robock, A., & Jackson, T. 2011. The international soil moisture network: a data hosting facility for global in situ soil moisture measurements. *Hydrology and Earth System Sciences*, 15, (5) 1675-1698.

Du, J.Y., Shi, J.C., & Sun, R.J. 2010. The development of HJ SAR soil moisture retrieval algorithm. *International Journal of Remote Sensing*, 31, (14) 3691-3705 .

Elachi, C. 1988. *Spaceborne radar remote sensing application and techniques*. IEEE Press, New York.

Elachi, C. & Van Zyl, J. 2006. *Introduction to the physics and techniques of remote sensing*, 2nd ed. Hoboken, N.J, Wiley-Interscience.

Elbially, S.G.K. 2011. *Potential of Spaceborne X & L-Band SAR-Data for Soil moisture mapping using GIS and its application to hydrological modelling: the example of Gottleuba Catchment, Saxony / Germany*. PhD (Dissertation). Dresden University of Technology.

Englhart, S., Keuck, V., & Siegert, F. 2011. Aboveground biomass retrieval in tropical forests - The potential of combined X- and L-band SAR data use. *Remote Sensing of Environment*, 115, (5) 1260-1271.

- Esch, T., Schenk, A., Thiel, M., Ullmann, T., Schmidt, M., & Dech, S. Land cover classification based on single-polarized VHR SAR images using texture information derived via speckle analysis, *In Geoscience and Remote Sensing Symposium (IGARSS), 2010 IEEE International*, pp. 1875-1878.
- Evans, D.L., Farr, T.G., Vanzyl, J.J., & Zebker, H.A. 1988. Radar Polarimetry - Analysis Tools and Applications. *IEEE Transactions on Geoscience and Remote Sensing*, 26, (6) 774-789.
- Evans, T.L., Costa, M., Telmer, K., & Silva, T.S.F. 2010. Using Alos/Palsar and Radarsat-2 to map land cover and seasonal inundation in the Brazilian Pantanal. *IEEE Journal of Selected Topics in Applied Earth Observations and Remote Sensing*, 3, (4) 560-575.
- Everitt, B. & Hothorn, T. 2006. *A handbook of statistical analyses using R*. Boca Raton u.a., Chapman & Hall/CRC.
- Foody, G.M. 2002. Status of land cover classification accuracy assessment. *Remote Sensing of Environment*, 80, (1) 185-201.
- Foody, G.M. & Mathur, A. 2004. Toward intelligent training of supervised image classifications: directing training data acquisition for SVM classification. *Remote Sensing of Environment*, 93, (1-2) 107-117.
- Foody, G.M. & Mathur, A. 2006. The use of small training sets containing mixed pixels for accurate hard image classification: Training on mixed spectral responses for classification by a SVM. *Remote Sensing of Environment*, 103, (2) 179-189.
- Fourikis, N. 2000. *Advanced array systems, applications and RF technologies*. San Diego, CA, Academic Press.
- Frery, A.C., Correia, A.H., & Freitas, C.D. 2007. Classifying multifrequency fully polarimetric imagery with multiple sources of statistical evidence and contextual information. *IEEE Transactions on Geoscience and Remote Sensing*, 45, (10) 3098-3109.
- Fritz, T. & Eineder, M. 2008, *TerraSAR-X Basic Product Specification Document TX-GS-DD-3302*, Issue 1.5.
- G.M.Foody 2006, "Pattern recognition and classification of remotely sensed images by artificial neural networks," *In Ecological Informatics: Scope, Techniques and Applications*, 2nd ed. F. Recknagel, ed., Berlin, Heidelberg: Springer-Verlag Berlin Heidelberg.
- Gao, J. 2009. *Digital analysis of remotely sensed imagery*. New York, McGraw Hill.
- Ghosh, A., Pyne, S., & Behari, J. 1998. Dielectric parameters of dry and wet soils at 14.89 HGz. *Ind.J.Radio Space.Phys.*, 27, 130-134
- Gomarasca, M. 2009. *Basics of geomatics*, 1st ed. New York, Springer.

- Gong, B.L., Im, J., & Mountrakis, G. 2011. An artificial immune network approach to multi-sensor land use/land cover classification. *Remote Sensing of Environment*, 115, (2) 600-614.
- Gong, P. 2006, "Information extraction," *In Remote sensing of human settlements*, ASPRS, Bethesda, MD, pp. 275-334.
- Gupta, K.K. & Gupta, R. 2007. Despeckle and geographical feature extraction in SAR images by wavelet transform. *Isprs Journal of Photogrammetry and Remote Sensing*, 62, (6) 473-484.
- Gupta, L., Mangai, U.G., & Das, S. 2008. Integrating region and edge information for texture segmentation using a modified constraint satisfaction neural network. *Image and Vision Computing*, 26, (8) 1106-1117.
- Hallikainen, M.T., Ulaby, F.T., Dobson, M.C., Elrayes, M.A., & Wu, L.K. 1985. Microwave dielectric behavior of wet soil.1. empirical-models and experimental-observations. *IEEE Transactions on Geoscience and Remote Sensing*, 23, (1) 25-34.
- Hanssen, R.F. 2002. *Radar Interferometry: Data Interpretation and Error Analysis*. Dordrecht, Kluwer Academic Publishers.
- Haralick, R.M., Shanmuga, K., & Dinstein, I. 1973. Textural features for image classification. *IEEE Transactions on Systems Man and Cybernetics*, SMC3, (6) 610-621.
- Henderson, F.M., Ryerson, R.A., Lewis, A.J., & American Society for Photogrammetry and Remote Sensing 1998. *Manual of remote sensing: Principles and applications of imaging radar*, v. 2. New York, J. Wiley.
- Heremans, S., Bossyns, B., Eerens, H., & Van Orshoven, J. 2011. Efficient collection of training data for sub-pixel land cover classification using neural networks. *International Journal of Applied Earth Observation and Geoinformation*, 13, (4) 657-667.
- Hoekman, D.H., Vissers, M.A.M., & Tran, T.N. 2011. Unsupervised full-polarimetric SAR data segmentation as a tool for classification of agricultural areas. *Selected Topics in Applied Earth Observations and Remote Sensing, IEEE Journal of*, 4, (2) 402-411
- Huang, C., Davis, L.S., & Townshend, J.R.G. 2002. An assessment of support vector machines for land cover classification. *International Journal of Remote Sensing*, 23, (4) 725-749.
- Huang, Z. & Lees, B.G. 2004. Combining non-parametric models for multisource predictive forest mapping. *Photogrammetric Engineering and Remote Sensing*, 70, (4) 415-425.
- Jackson, T.J. & Oneill, P.E. 1985. Aircraft scatterometer observations of soil-moisture on rangeland watersheds. *International Journal of Remote Sensing*, 6, (7) 1135-1152.

- Jensen, J.R. 2005. *Introductory digital image processing: a remote sensing perspective*, 3rd ed. Upper Saddle River, N.J, Prentice Hall.
- Jia, K., Wu, B., Li, Q., & Tian, Y. Improvement of classification accuracy integrating C- and X-band synthetic aperture radar data, *In Microwave, antenna, propagation and EMC technologies for wireless communications, 2009 3rd IEEE International Symposium on*, pp. 340-345.
- Jolliffe, I.T. 2002. *Principal component analysis*, 2nd ed. New York, Springer.
- Jong-Sen, L., Grunes, M.R., & Pottier, E. 2001. Quantitative comparison of classification capability: fully polarimetric versus dual and single-polarization SAR. *Geoscience and Remote Sensing, IEEE Transactions on*, 39, (11) 2343-2351
- Kanellopoulos, I. & Wilkinson, G.G. 1997. Strategies and best practice for neural network image classification. *International Journal of Remote Sensing*, 18, (4) 711-725.
- Kasischke, E.S., Tanase, M.A., Bourgeau-Chavez, L.L., & Borr, M. 2011. Soil moisture limitations on monitoring boreal forest regrowth using spaceborne L-band SAR data. *Remote Sensing of Environment*, 115, (1) 227-232.
- Kayitakire, F., Hamel, C., & Defourny, P. 2006. Retrieving forest structure variables based on image texture analysis and IKONOS-2 imagery. *Remote Sensing of Environment*, 102, (3-4) 390-401.
- Keil, M., Metz, A., Bock, M., Esch, T., Nieland, S., & Feigenspan, S. 2010, "Flächenerhebung und -statistik in CORINE Land Cover - Aktuelle Ergebnisse und Programmentwicklung," *In Flächennutzungsmonitoring II - Konzepte - Indikatoren - Statistik, IÖR Schriften*, vol. 52 G. Meinel & U. Schumacher, eds., pp. 93-108.
- Kersten, P.R., Lee, J.S., & Ainsworth, T.L. 2005. Unsupervised classification of polarimetric synthetic aperture radar images using fuzzy clustering and EM clustering. *IEEE Transactions on Geoscience and Remote Sensing*, 43, (3) 519-527.
- Keuchel, J., Naumann, S., Heiler, M., & Siegmund, A. 2003. Automatic land cover analysis for Tenerife by supervised classification using remotely sensed data. *Remote Sensing of Environment*, 86, (4) 530-541
- Kozlov, A.I., Ligthart, L.P., & Logvin, A.I. 2004. *Mathematical and physical modelling of microwave scattering and polarimetric remote sensing- monitoring the Earth's environment using polarimetric radar: formulation and potential applications*. Dordrecht, Kluwer Academic Publishers.
- Kseneman, M., Gleich, D., & Cucej, Z. 2011. Soil moisture estimation using high-resolution spotlight TerraSAR-X data. *IEEE Geoscience and Remote Sensing Letters*, 8, (4) 686-690.

- Kuhbauch, W., Davidson, M. J. W., Steingiesser, R., & Dockter, K. Investigation of agricultural land use in Italy and Germany by means of the multi-band/multi-frequency SIR-C/X-SAR system, *In Geoscience and Remote Sensing Symposium, 1995. IGARSS '95. 'Quantitative Remote Sensing for Science and Applications', International*, pp. 1061-1063.
- Kuplich, T.M. 2006. Classifying regenerating forest stages in Amazonia using remotely sensed images and a neural network. *Forest Ecology and Management*, 234, (1-3) 1-9.
- Kwarteng, A.Y., Dobson, M.C., Kellndorfer, J., & Williams, R. 2008. SAR-based land cover classification of Kuwait. *International Journal of Remote Sensing*, 29, (23) 6739-6778.
- Lacomme, P. 2001. *Air and spaceborne radar systems: an introduction* Norwich, N.Y, William Andrew Publishing.
- Lam, N., David Catts, Dale Quattrochi, Daniel Brown, & Robert McMaster 2004, "Scale," *In A research agenda for geographic information science*, R. B. McMaster & E. L. Uery, eds., Boca Raton, Fla: CRC Press, pp. 93-128.
- Lam-Dao, N. 2009. *Rice crop monitoring using new generation Synthetic Aperture Radar (SAR) imagery*. PhD University of Southern Queensland.
- Lardeux, C., Frison, P.L., Tison, C., Souyris, J.C., Stoll, B., Fruneau, B., & Rudant, J.P. 2009. Support vector machine for multifrequency SAR polarimetric data classification. *IEEE Transactions on Geoscience and Remote Sensing*, 47, (12) 4143-4152.
- Lardeux, C., Frison, P.L., Tison, C., Souyris, J.C., Stoll, B., Fruneau, B., & Rudant, J.P. 2011. Classification of tropical vegetation using multifrequency partial SAR polarimetry. *IEEE Geoscience and Remote Sensing Letters*, 8, (1) 133-137.
- Lee, J.S. & Pottier, E. 2009. *Polarimetric radar imaging: from basics to applications*. Boca Raton, CRC Press.
- Lewinski, St. & Bochenek, Z. 2009, "Rule-based classification of SPOT imagery using object-oriented approach for detailed land cover mapping," *In Remote sensing for a changing Europe*, Derya Maktav, ed., Amsterdam: IOS Press, pp. 197-204.
- Liang, S. 2004. *Quantitative remote sensing of land surfaces* Hoboken, N.J, Wiley-Interscience.
- Liang, S. 2008. *Advances in land remote sensing system, modeling, inversion and application*. Dordrecht, Springer.
- Lillesand, T.M., Kiefer, R.W., & Chipman, J.W. 2008. *Remote sensing and image interpretation*, 5th ed. New York, Wiley.
- Lloyd, C.D., Berberoglu, S., Curran, P.J., & Atkinson, P.M. 2004. A comparison of texture measures for the per-field classification of Mediterranean land cover. *International Journal of Remote Sensing*, 25, (19) 3943-3965.

- Lobell, D.B., Asner, G.P., Law, B.E., & Treuhaft, R.N. 2002. View angle effects on canopy reflectance and spectral mixture analysis of coniferous forests using AVIRIS. *International Journal of Remote Sensing*, 23, (11) 2247-2262.
- Lu, D. & Weng, Q. 2007. A survey of image classification methods and techniques for improving classification performance. *International Journal of Remote Sensing*, 28, (5) 823-870.
- Lu, D.S., Mausel, P., Batistella, M., & Moran, E. 2004. Comparison of land-cover classification methods in the Brazilian Amazon Basin. *Photogrammetric Engineering and Remote Sensing*, 70, (6) 723-731.
- Mahmoud, A., Elbially, S., Pradhan, B., & Buchroithner, M. 2011. Field-based landcover classification using TerraSAR-X texture analysis. *Advances in Space Research*, 48, (5) 799-805
- Maître, H. 2008. *Processing of synthetic aperture radar images* Hoboken, NJ, USA, Wiley.
- Major, D.J., Brisco, B., & Brown, R.J. 1991. Seasonal trajectory of radar backscatter of wheat and canola canopies. Proceedings of 4th Canadian Symposium on Remote Sensing 448-451.
- Massonnet, D. & Souyris, J.C. 2008. *Imaging with synthetic aperture radar*, 1st ed. Lausanne, Switzerland, EPFL Press.
- Mather, P.M. 2004. *Computer processing of remotely sensed images: an introduction*, 3rd ed. Chichester, West Sussex, England, John Wiley & Sons.
- Mattia, F., Satalino, G., Pauwels, V.R.N., & Loew, A. 2009. Soil moisture retrieval through a merging of multi-temporal L-band SAR data and hydrologic modelling. *Hydrology and Earth System Sciences*, 13, (3) 343-356.
- McNairn, H., Shang, J.L., Jiao, X.F., & Champagne, C. 2009. The contribution of ALOS PALSAR multipolarization and polarimetric data to crop classification. *IEEE Transactions on Geoscience and Remote Sensing*, 47, (12) 3981-3992.
- Mehta, N. S., Mohan, S., Das, D. K., Sundara Sarma, K. S., Bandyopadhyay, S., & Burman, D. 1995, *Microwave studies of soil/crop using ground based scatterometer data- scientific report*. SAC/RSA/RSAG/ARDSR/01/95.
- Merzouki, A., McNairn, H., & Pacheco, A. 2011. Mapping soil moisture using RADARSAT-2 data and local autocorrelation statistics. *IEEE Journal of Selected Topics in Applied Earth Observations and Remote Sensing*, 4, (1) 128-137.
- Michifumi Yoshioka, Toru Fujinaka, & Sigeru Omatu 2008, "SAR image classification by support vector machine," *In Image Processing for Remote Sensing*, C. H. Chen, ed., Boca Raton: CRC Press/Taylor & Francis Group, pp. 341-353.
- Myint, S.W. 2001. A robust texture analysis and classification approach for urban land-use and land-cover feature discrimination. *Geocarto International*, 16, 27-38

Navulur, K. 2007. *Multispectral image analysis using the object-oriented paradigm* Boca Raton, CRC Press/Taylor & Francis.

Nello, C. & John, S.-T. 2007, "Support vector and kernel methods," *In Intelligent data analysis: an introduction*, 2nd, rev. and extended ed. M. Berthold & D. J. Hand, eds., Berlin: Springer.

Nezry, E. Early identification and surface estimation of agricultural crops using ERS SAR images, *In Geoscience and Remote Sensing, 1997. IGARSS '97. Remote Sensing - A Scientific Vision for Sustainable Development., 1997 IEEE International*, pp. 2035-2037.

Nina, S.-N. L. 2008, "Methodologies for mapping land cover/land use and its change," *In Advances in land remote sensing system, modeling, inversion and application*, S. Liang, ed., Dordrecht: Springer, pp. 341-367.

Nussbaum, S. & Menz, G. 2008. *Object-based image analysis and treaty verification: new approaches in remote sensing - applied to nuclear facilities in Iran*. Springer.

Oh, Y., Sarabandi, K., & Ulaby, F.T. 1992. An empirical-model and an inversion technique for radar scattering from bare soil surfaces. *IEEE Transactions on Geoscience and Remote Sensing*, 30, (2) 370-381.

Okin, G.S., Roberts, D.A., Murray, B., & Okin, W.J. 2001. Practical limits on hyperspectral vegetation discrimination in arid and semiarid environments. *Remote Sensing of Environment*, 77, (2) 212-225.

Oliver, C. & Quegan, S. 2004. *Understanding synthetic aperture radar images* Boston, Artech House.

Ouma, Y.O., Ngigi, T.G., & Tateishi, R. 2006. On the optimization and selection of wavelet texture for feature extraction from high-resolution satellite imagery with application towards urban-tree delineation. *International Journal of Remote Sensing*, 27, (1) 73-104.

Pacifici, F., Del Frate, F., Solimini, C., & Emery, W. J. 2008, "Neural networks for land cover applications," *In Computational intelligence for remote sensing*, M. Graña & R. J. Duro, eds., Berlin: Springer, pp. 267-293.

Pai, P.-F. & Hsu, M.-F. 2011, "An enhanced support vector machines model for classification and rule generation," *In Computational Optimization, Methods and Algorithms*, S. Koziel & X. S. Yang, eds., Berlin, Heidelberg: Springer Berlin Heidelberg.

Pal, M. & Mather, P.M. 2003. An assessment of the effectiveness of decision tree methods for land cover classification. *Remote Sensing of Environment*, 86, (4) 554-565.

Pal, M. & Mather, P.M. 2005. Support vector machines for classification in remote sensing. *International Journal of Remote Sensing*, 26, (5) 1007-1011.

- Paola, J.D. & Schowengerdt, R.A. 1995. A review and analysis of backpropagation neural networks for classification of remotely-sensed multispectral imagery. *International Journal of Remote Sensing*, 16, (16) 3033-3058.
- Park, N.W. 2010. Accounting for temporal contextual information in land-cover classification with multi-sensor SAR data. *International Journal of Remote Sensing*, 31, (2) 281-298.
- Park, S.E. & Moon, W.M. 2007. Unsupervised classification of scattering mechanisms in polarimetric SAR data using fuzzy logic in entropy and alpha plane. *IEEE Transactions on Geoscience and Remote Sensing*, 45, (8) 2652-2664.
- Paudyal, D. R., Eiumnoh, A., & Aschbacher, J. Textural information in SAR images for land-cover applications, *In Geoscience and Remote Sensing Symposium, 1995. IGARSS '95. 'Quantitative Remote Sensing for Science and Applications', International*, pp. 1020-1022.
- Peng, X.L., Wang, J.F., & Zhang, Q.F. 2005. Deriving terrain and textural information from stereo RADARSAT data for mountainous land cover mapping. *International Journal of Remote Sensing*, 26, (22) 5029-5049.
- Pepin, S., Livingston, N.J., & Hook, W.R. 1995. Temperature-dependent measurement errors in time-domain reflectometry determinations of soil-water. *Soil Science Society of America Journal*, 59, (1) 38-43.
- Pierce, L. E., Bergen, K., Dobson, M. C., & Ulaby, F. T. Land-cover classification using SIR-C/X-SAR data, *In Geoscience and Remote Sensing Symposium, 1995. IGARSS '95. 'Quantitative Remote Sensing for Science and Applications', International*, pp. 918-920.
- Piotr, R. <http://cran.r-project.org/web/packages/FSelector/FSelector.pdf>. 9-27-2011.
- Platt, R.V. & Goetz, A.F.H. 2004. A comparison of AVIRIS and Landsat for land use classification at the urban fringe. *Photogrammetric Engineering and Remote Sensing*, 70, (7) 813-819.
- Price, K.P., Guo, X.L., & Stiles, J.M. 2002. Optimal Landsat TM band combinations and vegetation indices for discrimination of six grassland types in eastern Kansas. *International Journal of Remote Sensing*, 23, (23) 5031-5042.
- Rahul, R. 2008. *Multi-scale texture analysis of remote sensing images using gabor filter banks and wavelet transforms*. MSc. Texas A&M University.
- Raykov, T. & Marcoulides, G.A. 2008. *Introduction to applied multivariate analysis* New York, NY u.a., Routledge.
- Reddy, A.M. 2008. *Textbook of Remote Sensing and Geographical Information Systems*.
- Richards, J.A. 2009. *Remote sensing with imaging radar*. New York, Springer.

- Rosaria, S. 2007, "Neural Networks," *In Intelligent data analysis: an introduction*, 2nd, rev. and extended ed. M. Berthold & D. J. Hand, eds., Berlin: Springer, pp. 269-320.
- Roth, K., Schulin, R., Fluhler, H., & Attinger, W. 1990. Calibration of time domain reflectometry for water-content measurement using a composite dielectric approach. *Water Resources Research*, 26, (10) 2267-2273.
- San Martin, M. T. & Sadki, M. FCM and HCA performance analysis for crop type classification of SAR imagery, *In Geoscience and Remote Sensing Symposium, 2004. IGARSS '04. Proceedings. 2004 IEEE International*, pp. 2692-2694.
- Schauer, J. 2010, "Neue Grundlage der amtlichen Flächennutzungsstatistik: ALKIS - Chancen und Probleme," *In Flächennutzungsmonitoring II - Konzepte - Indikatoren - Statistik, IÖR Schriften*, vol. 52 G. Meinel & U. Schumacher, eds., pp. 67-78.
- Schmugge, T.J. 1983. Remote sensing of soil moisture- recent advances. *IEEE Transactions on Geoscience and Remote Sensing*, 21, (3) 336-344.
- Schmullius, C. & Furrer, R. 1992. Frequency-dependence of radar backscattering under different moisture conditions of vegetation-covered soil. *International Journal of Remote Sensing*, 13, (12) 2233-2245.
- Schmullius, C. & Nithack, J. Crop monitoring with multi-temporal airborne DLR E-SAR images, *In Geoscience and Remote Sensing Symposium, 1995. IGARSS '95. 'Quantitative Remote Sensing for Science and Applications', International*, pp. 719-721.
- Schmullius, C. & Schrage, T. Classification, crop parameter estimation and synergy effects using airborne DLR E-SAR and DAEDALUS images, *In Geoscience and Remote Sensing Symposium Proceedings, 1998. IGARSS '98. 1998 IEEE International*, pp. 97-99.
- Schowengerdt, R.A. 2007. *Remote sensing, models, and methods for image processing*, 3rd ed. Burlington, MA, Academic Press.
- Scott, W.R. & Smith, G.S. 1992. Measured electrical constitutive parameters of soil as functions of frequency and moisture-content. *IEEE Transactions on Geoscience and Remote Sensing*, 30, (3) 621-623.
- Shimoni, M., Borghys, D., Heremans, R., Perneel, C., & Acheroy, M. 2009. Fusion of PolSAR and PolInSAR data for land cover classification. *International Journal of Applied Earth Observation and Geoinformation*, 11, (3) 169-180.
- Skriver, H., Mattia, F., Satalino, G., Balenzano, A., Pauwels, V.R.N., Verhoest, N.E.C., & Davidson, M. 2011. Crop classification using short-revisit multitemporal SAR data. *Selected Topics in Applied Earth Observations and Remote Sensing, IEEE Journal of*, 4, (2) 423-431
- Skriver, H., Schon, J., & Dierking, W. Land-cover mapping using multitemporal, dual-frequency polarimetric SAR data, *In Geoscience and Remote Sensing Symposium, 2000. Proceedings. IGARSS 2000. IEEE 2000 International*, pp. 331-333.

- Skriver, H., Svendsen, M. T., Nielsen, F., & Thomsen, A. Crop classification by polarimetric SAR, *In Geoscience and Remote Sensing Symposium, 1999. IGARSS '99 Proceedings. IEEE 1999 International*, pp. 2333-2335.
- Soergel, U. 2010, "Review of Radar Remote Sensing on Urban Areas," *In Radar remote sensing of urban areas*, New York: Springer.
- Soo, C.L., Suan-Pheng, K., To-Phuc, T., Ping, C., Vo, Q.M., & Hock, L. 1998. Application of multitemporal ERS-2 synthetic aperture radar in delineating rice cropping systems in the Mekong River Delta, Vietnam. *Geoscience and Remote Sensing, IEEE Transactions on*, 36, (5) 1412-1420
- Steele, B.M. 2000. Combining multiple classifiers: An application using spatial and remotely sensed information for land cover type mapping. *Remote Sensing of Environment*, 74, (3) 545-556.
- Stimson, G.W. 1998. *Introduction to airborne radar*, 2nd ed. Mendam NJ, Scitech Publ.
- Stolz, R. & Mauser, W. First evaluations of Shuttle SIR-C and X-SAR data for landcover classifications, *In Geoscience and Remote Sensing Symposium, 1995. IGARSS '95. 'Quantitative Remote Sensing for Science and Applications', International*, pp. 1058-1060.
- Sullivan, R.J. 2004. *Radar foundations for imaging and advanced concepts* Raleigh, N.C, SciTech Pub.
- Tansly, K.J. & Millington, A.C. 2001. Investigating the potential for soil moisture and surface roughness monitoring in dry lands using ERS SAR data. *International Journal of Remote Sensing*, 22, (11) 2129-2149
- Thomas, J. J. 2008, "Passive microwave remote sensing for land applications," *In Advances in land remote sensing system, modeling, inversion and application*, S. Liang, ed., Dordrecht: Springer, pp. 341-367.
- Topp, G. C., Zegelin, S. J., & White, I. 1994, "Monitoring soil water content using TDR. An overview of progress," *In Symposium on time domain reflectometry in environmental applications*, K.M.O' Connor et al., ed., North Western University, Evanston, IL Spec. Publ., pp. 67-89.
- Torbick, N., Salas, W.A., Hagen, S., & Xiao, X.M. 2011. Monitoring rice agriculture in the Sacramento Valley, USA With Multitemporal PALSAR and MODIS Imagery. *Ieee Journal of Selected Topics in Applied Earth Observations and Remote Sensing*, 4, (2) 451-457.
- Treitz, P. M., Howarth, P. J., Filho, O. R., Soulis, E. D., & Kouwen, N. Classification of agricultural crops using SAR tone and texture statistics, *In Proceedings of 16th Canadian Symposium on Remote Sensing*, pp. 343-347.
- Tso, B. & Olsen, R.C. 2005. A contextual classification scheme based on MRF model with improved parameter estimation and multiscale fuzzy line process. *Remote Sensing of Environment*, 97, (1) 127-136.

- Tso, B. & Mather, P.M. 2009. *Classification methods for remotely sensed data*, 2nd ed. Boca Raton, CRC Press.
- Ulaby, F.T., Aslam, A., & Dobson, M.C. 1982. Effect of vegetation cover on the radar sensitivity to soil moisture. *IEEE Trans.Geo.& Remote Sens.*, GE-20, 476-481
- Ulaby, F.T., Batlivala, P.P., & Bare, J.E. 1980. Crop Identification with L-Band Radar. *Photogrammetric Engineering and Remote Sensing*, 46, (1) 101-105.
- Ulaby, F.T., Batlivala, P.P., & Dobson, M.C. 1978. Microwave backscatter dependence on surface-roughness, soil-moisture, and soil texture .1. Bare Soil. *IEEE Transactions on Geoscience and Remote Sensing*, 16, (4) 286-295.
- Ulaby, F.T., Held, D., Dobson, M.C., Mcdonald, K.C., & Senior, T.B.A. 1987. Relating polarization phase difference of SAR signals to scene properties. *IEEE Transactions on Geoscience and Remote Sensing*, 25, (1) 83-92.
- Ulaby, F.T., Li, R.Y., & Shanmugan, K.S. 1982. Crop classification using airborne radar and landsat data. *IEEE Transactions on Geoscience and Remote Sensing*, 20, (1) 42-51.
- Ulaby, F.T., Razani, M., & Dobson, M.C. 1983. Effects of vegetation cover on the microwave radiometric sensitivity to soil-moisture. *IEEE Transactions on Geoscience and Remote Sensing*, 21, (1) 51-61.
- Ulaby, F.T., Moore, R.K., & Fung, A.K. 1981. *Microwave remote sensing: active and passive* Reading, Mass, Addison-Wesley Pub. Co., Advanced Book Program/World Science Division.
- Ulaby, F.T., Moore, R.K., & Fung, A.K. 1986. *Microwave remote sensing: active and passive* Reading, Mass, Addison-Wesley Pub. Co., Advanced Book Program/World Science Division.
- Van Zyl, J. 2011. *Synthetic aperture radar polarimetry*, 1st ed. Hoboken, NJ, Wiley.
- Venables, W.N., Smith, D.M., & Core Team, R.D. 2011. *An introduction to R: notes on R: a programming environment for data analysis and graphics, Version 2.13.0* Bristol, Network Theory.
- Wang, B.C. 2008. *Digital signal processing techniques and applications in radar image processing* Hoboken, N.J, John Wiley.
- Wang, C.Z., Wu, J.P., Zhang, Y., Pan, G.D., Qi, J.G., & Salas, W.A. 2009. Characterizing L-band scattering of paddy rice in southeast china with radiative transfer model and multitemporal ALOS/PALSAR imagery. *IEEE Transactions on Geoscience and Remote Sensing*, 47, (4) 988-998.
- Wang, J., Zhou, L., & Yang, X. 2009, "Geographic information systems and spatial analysis for coastal ecosystem research and management," *In Remote sensing and geospatial technologies for coastal ecosystem assessment and management*, X. Yang, ed., Berlin: Springer, pp. 45-66.

- Wang, X. & Wang, H. 2004. Markov random field modeled range image segmentation. *Pattern Recognition Letters*, 25, (3) 367-375.
- Weng, Q. 2010. *Remote sensing and GIS integration: theories, methods, and applications* New York, McGraw-Hill.
- Wever, T., Henkel, J., & Hafner, B. Crop identification using multifrequency and polarimetric SAR data, *In Geoscience and Remote Sensing Symposium, 1995. IGARSS '95. 'Quantitative Remote Sensing for Science and Applications', International*, pp. 1213-1215.
- Wilson, E. A. & Ulaby, F. T. 1984, *The microwave propagation and backscattering characteristics of vegetation, Radiation Laboratory Technical Report*, The University of Michigan. Ann Arbor.
- Xianfeng, J., Heather, M., Jiali, S., & Jianguo, L. The sensitivity of multi-frequency (X, C and L-Band) radar backscatter signatures to bio-physical variables (LAI) over corn and soybean fields, *In ISPRS TC VII Symposium - 100 Years ISPRS*, Part 7B edn, W. Wagner & B. Székely, eds., Vienna, Austria.
- Xin, T., Erxue, C., Zengyuan, L., Su, Z. B., Feilong, L., Lina, B., & Fengyu, W. Comparison of crop classification capabilities of spaceborne multi-parameter SAR data, *In Geoscience and Remote Sensing Symposium (IGARSS), 2010 IEEE International*, pp. 359-362.
- Xing, M., Guo, R., Qiu, C.W., Liu, L., & Bao, Z. 2010. Experimental research of unsupervised Cameron/maximum-likelihood classification method for fully polarimetric synthetic aperture radar data. *Int Radar Sonar and Navigation*, 4, (1) 85-95.
- Xinwu, L., Touzi, R., & Huadong, G. Land cover characterization and classification using polarimetric ALOS PALSAR, *In Geoscience and Remote Sensing Symposium, 2008. IGARSS 2008. IEEE International*, p. IV-1276.
- Yang, Z.R. 2010. *Machine learning approaches to bioinformatics*, v. 4 ed. Singapore, World Scientific.
- Zhang, L.M., Zou, B., Zhang, J.P., & Zhang, Y. 2010. Classification of polarimetric SAR image based on support vector machine using multiple-component scattering model and texture features. *Eurasip Journal on Advances in Signal Processing*.
- Zhang, Y., Wang, C.Z., Wu, J.P., Qi, J.G., & Salas, W.A. 2009. Mapping paddy rice with multitemporal ALOS/PALSAR imagery in southeast China. *International Journal of Remote Sensing*, 30, (23) 6301-6315.
- Zhang, Y.D. & Wu, L.A. 2011. Crop Classification by Forward Neural Network with Adaptive Chaotic Particle Swarm Optimization. *Sensors*, 11, (5) 4721-4743.
- Zhang, Y.D., Wu, L.N., & Wei, G. 2009. A new classifier for polarimetric SAR images. *Progress in Electromagnetics Research*, 94, 83-104.

Zhongxin, C., Sen, L., Jianqiang, R., Pan, G., Mingwei, Z., Limin, W., Shenliang, X., & Daohui, J. 2008, "Monitoring and management of agriculture with remote sensing," *In Advances in land remote sensing system, modeling, inversion and application*, S. Liang, ed., Dordrecht: Springer, p. 397.

Zribi, M. & Dechambre, M. 2003. A new empirical model to retrieve soil moisture and roughness from C-band radar data. *Remote Sensing of Environment*, 84, (1) 42-52.

Zribi, M., Le Hetarat-Masclé, S., Ottele, C., Kammoun, B., & Guerin, C. 2003. Surface soil moisture estimation from the synergistic use of the (multi-incidence and multi-resolution) active microwave ERS Wind Scatterometer and SAR data. *Remote Sensing of Environment*, 86, (1) 30-41.

## Internet Resources

[www1] TerraSAR-X ground segment. Basic product specification document  
<http://sss.terrasar-x.dlr.de/pdfs/TX-GS-DD-3302.pdf> , accessed on 20/10/2011.

[www2] [http://earth.esa.int/download/alos/PALSAR\\_info\\_users\\_v1.1.pdf](http://earth.esa.int/download/alos/PALSAR_info_users_v1.1.pdf), accessed on 20/10/2011.

[www3] <http://www.smul.sachsen.de/lfulg/>, accessed on 20/10/2011.

[www4]

[http://www.landesvermessung.sachsen.de/inhalt/produkte/dhm/dgm/dgm\\_detail.html](http://www.landesvermessung.sachsen.de/inhalt/produkte/dhm/dgm/dgm_detail.html)  
accessed on 19-10-2011.

[www5] <http://www.landwirtschaft.sachsen.de/landwirtschaft/1058.htm>. 2011.

## 10 Appendices

### Appendix A

Table A.1. List of Software that supports ERSDAC PALSAR Products (Oct. 2011)

software	version	supported products	Image processing	SAR data processing	Interferometry	Polarimetric SAR data analysis	URL
ENVI	4.8	L1.1SLC, L1.5 <sup>*1</sup> , L4.1 <sup>*1</sup> , L4.2	0				<a href="http://www.itvis.com/language/en-US/ProductsServices/ENVI.aspx">http://www.itvis.com/language/en-US/ProductsServices/ENVI.aspx</a>
ENVI + SARscape		L1.0, L1.1SLC, L1.5, L4.1, L4.2	0	0	0	0	<a href="http://www.itvis.com/language/en-us/productservices/envi/sarscape.aspx">http://www.itvis.com/language/en-us/productservices/envi/sarscape.aspx</a>
PCI Geomatica	10.3	L1.5, L4.1, L4.2, L1.5long	0				<a href="http://www.pcigeomatics.com/">http://www.pcigeomatics.com/</a>
PG-Steamer	4.1	L1.5, L4.1, L4.2	0				<a href="http://www.pixoneer.com/">http://www.pixoneer.com/</a>
ERDAS IMAGINE		L1.1SLC, L1.5, L4.1, L4.2	0				<a href="http://www.erdas.com/products/ERDASIMAGINE/ERDASIMAGINE/Details.aspx">http://www.erdas.com/products/ERDASIMAGINE/ERDASIMAGINE/Details.aspx</a>
ERDAS IMAGINE + Radar Mapping Suite		L1.1SLC, L1.5, L4.1, L4.2	0		0		<a href="http://www.erdas.com/products/ERDASIMAGINE/IMAGINERadarMappingSuite/Details.aspx">http://www.erdas.com/products/ERDASIMAGINE/IMAGINERadarMappingSuite/Details.aspx</a>
PuSAR	8	L1.0, L1.1SLC	0	0	0		<a href="http://www.ists.co.jp/e/index.php/sc/products.html">http://www.ists.co.jp/e/index.php/sc/products.html</a>
Gamma Modular SAR Processor		L1.0, L1.1SLC		0			<a href="http://www.gamma-rs.ch/software/msp-modular-sar-processor.html">http://www.gamma-rs.ch/software/msp-modular-sar-processor.html</a>
Gamma Interferometric SAR Processor		L1.1SLC			0		<a href="http://www.gamma-rs.ch/software/isp-interferometric-sar-processor.html">http://www.gamma-rs.ch/software/isp-interferometric-sar-processor.html</a>
Focus		L1.0		0			<a href="http://www.seaspace.com/modules/layout/faceoff/attach/Focus_brochure.pdf">http://www.seaspace.com/modules/layout/faceoff/attach/Focus_brochure.pdf</a>
Phase		L1.1SLC			0		<a href="http://www.seaspace.com/modules/layout/faceoff/attach/phase_brochure.pdf">http://www.seaspace.com/modules/layout/faceoff/attach/phase_brochure.pdf</a>

#### Charge-free Software

software	version	supported products	Image processing	SAR data processing	Interferometry	Polarimetric SAR data analysis	URL
RAT	0.21	L1.1SLC, L1.5, L4.1	0		0	0	<a href="http://radartools.berlios.de/index.php">http://radartools.berlios.de/index.php</a>
POLSARPRO	4.2	L1.1SLC				0	<a href="http://earth.eo.esa.int/polsarpro/default.html">http://earth.eo.esa.int/polsarpro/default.html</a>
Quad-pol Viewer	0.1.2.0	L1.1SLC, L4.1				0	<a href="http://remote-sensing.isp.jp/Quad-pol/index.html">http://remote-sensing.isp.jp/Quad-pol/index.html</a>
GMTSAR		L1.0			0		<a href="http://topex.ucsd.edu/gmtsar/">http://topex.ucsd.edu/gmtsar/</a>
ROI_PAC	3.0.1	L1.0			0		<a href="http://www.roipac.org/ALOS_PALSAR">http://www.roipac.org/ALOS_PALSAR</a>

**Note:** L1.5, L4.1 and L4.2 Ortho products are readable by general-purpose image software that supports GeoTIFF.

\*1: Please inquire for the import patch (for ENVI) of L1.5, L4.1 and L4.2 Ortho product (binary format data) to the following addresses.

<http://www.itvis.com/UserCommunity/CodeLibrary.aspx>

([http://www.palsar.ersdac.or.jp/doc/pdf/SoftwareforProducts\\_jp.pdf](http://www.palsar.ersdac.or.jp/doc/pdf/SoftwareforProducts_jp.pdf))

Appendix B

Table B.1. Separability values of class-pairs indicating the relevant batch-code (Bold figures indicate value > 1.75).

Class-pair		Homo	Dissim.	Contrast	Ang. 2 <sup>nd</sup>	Energy	Entropy	GLCM Mean	GLCM Variance	GLCM STD	GLCM Correlation
Orchard	Cereals	1.39 b8	1.58 b11	1.42 b15	<b>1.84 b6</b>	1.7 b6	1.34 b6	<b>1.77 b9</b>	<b>1.97 b20</b>	1.44 b7	1.58 b10
		1.37 b7	1.57 b10	1.39 b14	<b>1.83 b8</b>	1.69 b7	1.33 b7	<b>1.77 b8</b>	<b>1.97 b19</b>	1.43 b8	1.54 b8
Orchard	Grass	1.48 b16	1.43 b16	1.45 b16	1.5 b20	1.5 b20	1.51 b20	<b>1.98 b8</b>	<b>1.97 b4</b>	1.24 b1	1.59 b8
		1.28 b4	1.41 b20	1.44 b20	1.44 b16	1.43 b16	1.5 b12	<b>1.98 b7</b>	<b>1.97 b3</b>	1.18 b3	1.55 b7
Orchard	Rape	0.31 b8	0.23 b19	0.15 b4	0.27 b16	0.27 b16	0.18 b3	1.4 b4	1.4 b8	1.04 b7	0.43 b13
		0.27 b4	0.21 b15	0.15 b19	0.24 b15	0.23 b15	0.17 b1	1.4 b3	1.4 b7	0.96 b6	0.21 b6
Orchard	Maize	0.95 b8	0.6 b11	0.71 b7	0.27 b11	0.26 b11	0.42 b11	1.42 b8	1.58 b8	<b>1.97 b2</b>	0.86 b11
		0.76 b7	0.6 b10	0.55 11	0.26 b16	0.25 b12	0.34 b10	1.42 b7	1.58 b7	<b>1.95 b3</b>	0.8 b10
Cereals	Grass	1.45 b5	1.19 b16	0.97 b16	<b>1.82 b8</b>	1.65 b8	1.17 b8	0.9 b4	0.74 b17	0.54 b10	0.8 b8
		1.37 b8	1.08 b20	0.94 b5	<b>1.81 b6</b>	1.65 b5	1.17 b5	0.9 b3	0.73 b20	0.53 b14	0.78 b4
Cereals	Rape	1.3 b16	1.48 b16	1.41 b16	<b>1.84 b6</b>	1.69 b6	1.21 b6	<b>1.93 b8</b>	<b>1.99 b9</b>	1.68 b7	1.73 b6
		1.28 b6	1.48 b3	1.32 b12	<b>1.82 b7</b>	1.67 b7	1.20 b7	<b>1.93 b7</b>	<b>1.99 b8</b>	1.67 b8	1.69 b8
Cereals	Maize	1.52 b6	1.55 b16	1.49 b16	<b>1.85 b8</b>	1.71 b8	1.35 b7	<b>1.93 b8</b>	<b>2.00 b9</b>	<b>1.9 b8</b>	1.34 b11
		1.44 b16	1.48 b20	1.33 b3	<b>1.83 b7</b>	1.68 b7	1.33 b6	<b>1.93 b7</b>	<b>2.00 b8</b>	<b>1.9 b3</b>	1.19 b12
Grass	Rape	1.73 b16	1.55 b16	1.63 b16	1.74 b20	1.72 b20	1.72 b12	<b>2.00 b8</b>	<b>2.00 b8</b>	1.52 b6	<b>1.91 b6</b>
		1.25 b20	1.48 b20	1.43 b20	1.74 b16	1.72 16	1.61 b16	<b>2.00 b7</b>	<b>2.00 b7</b>	1.51 b8	<b>1.85 b8</b>
Grass	Maize	<b>1.75 b16</b>	1.33 b20	1.51 b16	1.47 b20	1.47 b20	1.34 b20	<b>2.00 b8</b>	<b>2.00 b8</b>	<b>1.97 b2</b>	0.99 b5
		1.46 b20	1.24 b16	1.43 b20	1.39 b16	1.39 b16	1.27 b16	<b>2.00 b7</b>	<b>2.00 b7</b>	<b>1.97 b1</b>	0.96 b8
Rape	Maize	0.63 b6	0.52 b12	0.88 b7	0.91 b16	0.89 b16	0.7 b12	<b>1.88 b12</b>	<b>1.88 b12</b>	1.36 b2	0.71 b11
		0.57 b8	0.47 b16	0.46 b8	0.68 b13	0.65 b13	0.7 b11	<b>1.88 b11</b>	<b>1.88 b11</b>	1.33 b11	0.52 b10

Table B.2. Classification accuracy (%) and Kappa index (%) using the Information Gain method.

	10		15		20		25		30		40		50	
	ACC	Kappa												
SVM	94.62	91.55	93.55	89.75	93.55	89.91	94.62	91.55	94.62	91.52	95.70	93.20	94.62	91.61
ANN (mlp)	92.47	88.36	92.47	88.24	93.55	89.88	92.47	88.25	92.47	88.50	91.40	86.53	93.55	89.89
ANN (mlpe)	92.47	88.24	92.47	88.24	93.55	89.88	92.47	88.24	92.47	88.16	91.40	86.78	93.55	90.02
KNN	92.47	88.28	92.47	88.10	92.47	88.13	92.47	88.24	93.55	89.87	93.55	89.87	94.62	91.68
LR	90.32	85.27	91.40	86.76	91.40	86.73	87.09	80.35	82.80	74.24	78.49	68.30	82.80	74.25
LDA	91.40	86.70	90.32	85.10	90.32	85.09	92.47	88.25	92.47	87.98	89.25	82.97	88.17	81.26

Table B.3. Classification accuracy (%) and Kappa index (%) using the gain ratio method.

	10		15		20		25		30		40		50	
	ACC	Kappa												
SVM	84.95	75.78	84.95	75.66	92.47	88.41	93.55	89.95	94.62	91.61	93.55	89.91	93.55	89.95
ANN (mlp)	83.87	74.42	83.87	75.48	89.25	83.32	91.40	86.77	94.62	91.56	90.32	84.69	89.25	83.25
ANN (mlpe)	84.95	76.13	84.95	76.71	92.47	88.29	91.39	86.82	94.62	91.71	91.40	86.66	91.40	86.79
KNN	83.87	74.53	82.80	73.02	89.25	83.43	92.47	88.33	94.62	91.68	93.55	89.95	92.48	88.21
LR	75.27	61.86	73.12	59.12	80.65	71.64	80.65	71.28	79.57	70.31	73.12	59.16	75.27	62.27
LDA	77.42	63.91	77.42	64.30	90.32	84.71	89.25	83.14	87.09	79.82	89.25	83.40	88.17	81.61

Table B.4. Classification accuracy (%) and Kappa index (%) using the symmetrical uncertainty method.

	10		15		20		25		30		40		50	
	ACC	Kappa												
SVM	84.95	75.78	86.02	77.18	92.47	88.33	94.62	91.61	92.47	88.16	93.55	89.91	94.62	91.54
ANN (mlp)	87.09	79.49	86.02	77.76	92.47	88.18	88.17	81.48	91.40	86.59	90.32	85.21	91.40	86.83
ANN (mlpe)	86.02	77.82	86.02	77.78	91.40	86.63	91.40	86.51	91.40	86.63	90.32	85.02	93.55	89.92
KNN	83.87	74.53	87.10	79.49	91.40	86.82	93.55	89.95	93.55	89.95	93.55	89.95	94.62	91.68
LR	75.27	61.86	73.12	59.12	86.02	79.09	87.09	80.70	81.72	72.66	83.87	75.67	82.80	74.25
LDA	77.42	63.91	77.42	64.30	91.40	86.59	90.32	84.90	89.25	83.26	89.25	83.26	88.17	81.26

Table B.5. Classification accuracy (%) and Kappa index (%) using the random forest importance methods.

	10		15		20		25		30		40		50	
	ACC	Kappa												
SVM	94.62	91.52	94.62	91.46	93.55	89.77	94.62	91.46	93.55	89.80	93.55	89.72	93.55	89.98
ANN (mlp)	90.32	84.97	90.32	85.35	92.47	88.15	90.32	84.99	90.32	85.19	90.32	84.99	90.32	84.83
ANN (mlpe)	90.32	84.74	91.39	86.63	91.40	86.66	90.32	85.03	90.32	85.21	91.40	86.52	90.32	85.18
KNN	92.47	88.21	93.55	89.87	93.55	89.95	93.55	89.87	92.47	88.21	93.55	89.95	91.40	86.73
LR	83.87	75.71	84.95	77.42	87.09	80.43	87.10	80.38	80.65	71.73	87.09	80.47	84.95	76.33
LDA	89.25	83.55	92.47	88.33	93.55	89.95	92.47	88.11	89.25	82.71	89.25	82.76	87.10	79.52

Table B.6. Classification accuracy (%) and Kappa index (%) using the principle component analysis method.

	10		15		20		25		30		40		50	
	ACC	Kappa												
SVM	93.55	89.91	93.55	89.71	94.62	91.55	92.47	88.11	91.39	86.48	90.32	84.86	91.40	86.59
ANN (mlp)	92.47	88.23	91.40	86.58	92.47	88.14	91.40	86.37	89.25	82.92	87.10	79.89	87.09	80.21
ANN (mlpe)	92.47	88.36	91.40	86.61	92.47	88.31	91.40	86.50	89.25	82.92	87.10	80.14	87.10	80.11
KNN	91.40	86.63	92.47	88.33	92.47	88.25	88.17	81.51	87.10	79.69	87.10	79.89	88.17	81.32
LR	92.47	88.36	89.25	83.38	89.25	83.17	76.34	64.44	73.12	60.11	79.57	69.19	76.34	63.72
LDA	89.25	82.98	91.40	86.52	92.47	88.39	80.65	70.19	79.56	68.89	84.95	76.63	81.72	72.34

Table B.7. Selected 10 features using the four selection methods.

Selection Method	Features									
Information Gain	b9_gm	b17_gm	b17_gv	b17_mean	b18_gm	b18_gv	b19_gm	b19_gv	b20_gm	b20_gv
gain ratio	b1_gm	b1_gv	b1_mean	b2_gm	b2_gv	b3_gm	b3_gv	b4_gm	b4_gv	b5_gm
Symmetrical Uncertainty	b1_gm	b1_gv	b1_mean	b2_gm	b2_gv	b3_gm	b3_gv	b4_gm	b4_gv	b5_gm
Random Forest	b3_gv	b8_gv	b9_mean	b10_gm	b10_gv	b12_gm	b13_gv	b14_gm	b15_gv	b16_gv
Principle component	b13_gm	b13_mean	b14_gm	b15_gm	b16_gm	b17_gm	b17_mean	b18_gm	b19_gm	b20_gm

## Appendix C

Table C.1. Separability values for TSX backscattering image rescaled to 5 bits using 2 and 3 standard deviations.

	Class-pair	Separability											
		Mean	StD	H.	C.	D.	Ang	Enr	Ent	GM	GV.	GSD	GC
31.05.10 – 2 STD	Cereals-Orchard	1.66	0.50	0.68	0.67	0.73	0.44	0.44	0.79	1.66	1.82	1.08	0.67
	Cereals-Maize	1.89	0.76	1.60	1.30	1.47	0.94	1.00	1.51	1.89	1.99	1.61	0.55
	Cereals-Grass	0.98	0.13	0.14	0.25	0.24	0.27	0.23	0.13	0.98	0.73	0.29	0.57
	Cereals-Rape	1.90	1.21	1.40	1.32	1.36	0.88	0.95	1.46	1.90	1.99	1.59	1.01
	Orchard-Maize	1.38	0.06	0.56	0.44	0.56	0.41	0.44	0.39	1.38	1.43	0.37	0.09
	Orchard-Grass	1.89	0.23	0.23	0.18	0.20	0.44	0.42	0.42	1.89	1.86	0.38	0.02
	Orchard-Rape	1.56	0.44	0.31	0.48	0.40	0.35	0.37	0.31	1.56	1.58	0.41	0.13
	Maize-Grass	2.00	0.46	1.09	0.90	1.05	1.31	1.31	1.23	2.00	2.00	1.00	0.12
	Maize-Rape	0.17	0.24	0.11	0.07	0.10	0.00	0.01	0.01	0.17	0.14	0.08	0.22
Grass-Rape	2.00	1.01	0.85	0.91	0.88	1.25	1.25	1.16	2.00	2.00	0.98	0.24	
31.05.10 – 3 STD	Cereals-Orchard	1.64	0.53	0.8	0.76	0.79	0.88	0.86	0.83	1.64	1.76	0.32	0.24
	Cereals-Maize	1.88	0.71	1.42	1.19	1.33	1.47	1.42	1.31	1.88	1.97	0.71	0.25
	Cereals-Grass	0.99	0.29	0.46	0.45	0.47	0.40	0.48	0.46	0.99	0.86	0.09	0.12
	Cereals-Rape	1.89	1.19	1.27	1.32	1.29	1.42	1.36	1.29	1.89	1.97	0.78	0.32
	Orchard-Maize	1.37	0.03	0.60	0.32	0.50	0.45	0.48	0.37	1.37	1.42	0.10	0.11
	Orchard-Grass	1.89	0.21	0.21	0.17	0.19	0.42	0.40	0.40	1.89	1.89	0.08	0.03
	Orchard-Rape	1.56	0.47	0.32	0.51	0.40	0.37	0.39	0.34	1.56	1.57	0.13	0.18
	Maize-Grass	2.00	0.36	1.15	0.76	1.00	1.35	1.34	1.20	2.00	2.00	0.33	0.08
	Maize-Rape	0.17	0.33	0.12	0.09	0.06	0.01	0.01	0.01	0.17	0.16	0.00	0.01
Grass-Rape	2.00	1.04	0.86	0.93	0.89	1.27	1.26	1.18	2.00	2.00	0.39	0.14	
17.06.10 – 2 STD	Cereals-Orchard	1.76	1.08	0.70	1.34	1.41	1.18	0.97	0.66	1.76	1.93	1.00	1.32
	Cereals-Maize	1.73	1.35	1.01	1.51	1.60	1.46	1.33	1.00	1.73	1.87	1.10	1.05
	Cereals-Grass	1.05	0.05	0.04	0.37	0.32	1.13	0.86	0.03	1.05	1.09	0.77	0.77
	Cereals-Rape	1.92	1.64	1.16	1.69	1.77	1.36	1.24	1.29	1.92	2.00	1.34	1.51
	Orchard-Maize	1.07	0.19	0.23	0.18	0.22	0.28	0.31	0.27	1.07	1.20	0.55	0.06
	Orchard-Grass	0.75	0.71	0.53	0.61	0.60	0.90	0.86	0.89	0.75	0.66	0.37	0.36
	Orchard-Rape	0.76	0.44	0.28	0.43	0.37	0.48	0.50	0.45	0.76	0.78	0.12	0.06
	Maize-Grass	0.82	1.03	0.85	0.90	0.92	1.27	1.26	1.20	0.82	0.74	0.97	0.14
	Maize-Rape	1.98	0.64	0.55	0.48	0.52	0.98	0.97	0.89	1.98	1.98	0.98	0.22
Grass-Rape	1.46	1.30	1.04	1.22	1.17	1.66	1.60	1.54	1.46	1.43	0.54	0.67	
17.06.10 – 3 STD	Cereals-Orchard	1.70	1.11	1.38	1.30	1.31	1.37	1.31	1.31	1.70	1.89	0.02	0.58
	Cereals-Maize	1.69	1.28	1.55	1.41	1.47	1.65	1.60	1.52	1.69	1.83	0.20	0.60
	Cereals-Grass	1.04	0.29	0.56	0.77	0.69	0.28	0.32	0.40	1.04	1.09	0.37	0.71
	Cereals-Rape	1.88	1.48	1.64	1.58	1.57	1.81	1.73	1.67	1.88	1.99	0.18	0.72
	Orchard-Maize	1.06	0.12	0.22	0.08	0.17	0.30	0.33	0.24	1.06	1.16	0.21	0.09
	Orchard-Grass	0.75	0.70	0.56	0.63	0.61	0.89	0.84	0.87	0.75	0.71	0.32	0.03
	Orchard-Rape	0.76	0.41	0.25	0.42	0.34	0.44	0.45	0.43	0.76	0.77	0.11	0.08
	Maize-Grass	0.81	0.92	0.88	0.78	0.87	1.29	1.27	1.18	0.81	0.78	0.77	0.08
	Maize-Rape	1.98	0.55	0.48	0.47	0.46	0.88	0.86	0.78	1.98	1.98	0.15	0.02
Grass-Rape	1.46	1.29	1.05	1.22	1.16	1.61	1.55	1.52	1.46	1.45	0.58	0.04	

Table C.2. Separability values according to the backscattering calculation method.

	Class-pair	Separability											
		Mean	STD	H	C	D	Ang	Enr	Ent	GM	GV	GSD	GC
GIM	Cereals-Orchard	1.66	0.50	0.94	0.67	0.73	1.54	1.24	0.17	1.66	1.82	0.53	0.52
	Cereals-Maize	1.89	0.77	1.07	1.31	1.48	1.73	1.51	0.34	1.89	1.99	1.69	0.38
	Cereals-Grass	0.98	0.13	1.01	0.26	0.26	1.42	1.05	0.10	0.98	0.74	0.03	0.52
	Cereals-Rape	1.90	1.23	1.20	1.32	1.36	1.67	1.43	0.23	1.90	1.99	1.31	0.90
	Orchard-Maize	1.38	0.06	0.38	0.45	0.57	0.51	0.42	0.40	1.38	1.43	0.90	0.09
	Orchard-Grass	1.89	0.23	0.15	0.18	0.20	0.11	0.10	0.09	1.89	1.86	0.33	0.02
	Orchard-Rape	1.56	0.47	0.24	0.49	0.40	0.24	0.18	0.14	1.56	1.58	0.46	0.17
	Maize-Grass	2.00	0.47	0.91	0.91	1.07	0.74	0.62	0.54	2.00	2.00	1.50	0.16
	Maize-Rape	0.17	0.26	0.24	0.07	0.10	0.12	0.10	0.11	0.17	0.14	0.16	0.29
	Grass-Rape	2.00	1.04	0.64	0.92	0.89	0.50	0.41	0.32	2.00	2.00	1.09	0.26
DEM	Cereals-Orchard	1.64	0.50	0.96	0.67	0.74	1.56	1.26	0.18	1.64	1.82	0.51	0.55
	Cereals-Maize	1.89	0.75	1.15	1.32	1.48	1.73	1.52	0.34	1.89	1.99	1.67	0.37
	Cereals-Grass	0.97	0.12	0.98	0.32	0.30	1.44	1.08	0.11	0.97	0.75	0.04	0.57
	Cereals-Rape	1.91	1.23	1.18	1.32	1.37	1.67	1.42	0.23	1.91	1.99	1.31	0.76
	Orchard-Maize	1.36	0.05	0.43	0.47	0.57	0.50	0.42	0.38	1.36	1.43	0.88	0.11
	Orchard-Grass	1.80	0.21	0.13	0.16	0.19	0.11	0.10	0.09	1.80	1.77	0.28	0.03
	Orchard-Rape	1.60	0.46	0.26	0.48	0.39	0.19	0.15	0.12	1.60	1.64	0.46	0.07
	Maize-Grass	2.00	0.43	0.91	0.93	1.08	0.72	0.61	0.52	2.00	2.00	1.38	0.20
	Maize-Rape	0.19	0.26	0.10	0.07	0.11	0.14	0.12	0.11	0.19	0.16	0.15	0.17
	Grass-Rape	2.00	0.99	0.68	0.90	0.88	0.44	0.36	0.30	2.00	2.00	0.98	0.16

Table C.3. Separability values for TSX imagery from 31/05/2010 and 17/06/2010.

TSX (31/05/2010)				TSX (17/06/2010)			
image	Texture (angle/distance)		Separability	image	Texture (angle/distance)		Separability
<b>Cereals versus Maize</b>							
TSX_σ°	GM	(90° / 1)	1.93	Local Sigma 3	GC	(45° / 1)	1.69
TSX_σ°	GV	(90° / 1)	1.96	Enhanced Lee 3	Ang	(45° / 1)	1.61
Gamma 3	GM	(90° / 1)	1.97	Gamma 3	Ang	(45° / 1)	1.53
Gamma 3	GV	(90° / 1)	1.93				
Gamma 3	GC	(90° / 1)	1.90				
<b>Cereals versus Grass</b>							
Gamma 3	H	(135° / 3)	1.45	Local Sigma 3	GC	(45° / 1)	1.71
Gamma 3	Ang	(135° / 3)	1.82	Local Sigma 3	Ang	(0° / 1)	1.81
Gamma 3	Enr	(135° / 3)	1.63	Local Sigma 3	Enr	(0° / 1)	1.63
Gamma 3	GM	(135° / 3)	1.38	Gamma 3	GV	(45° / 1)	1.57
<b>Cereals versus Rape</b>							
Gamma 3	Ang	(135° / 1)	1.80	Enhanced Frost 3	GM	(45° / 1)	1.70
Gamma 3	Enr	(135° / 1)	1.65	Enhanced Frost 3	GV	(45° / 1)	1.63
Gamma 3	GM	(135° / 1)	1.99	Local Sigma 3	GC	(45° / 1)	1.46
Gamma 3	GV	(135° / 1)	1.99				
Gamma 3	GSD	(135° / 1)	1.87				
<b>Cereals versus Orchard</b>							
Gamma 3	Ang	(135° / 3)	1.85	Local Sigma 3	Ang	(45° / 1)	1.85
Gamma 3	GM	(135° / 3)	1.93	Enhanced Lee 3	GM	(45° / 1)	1.83
Gamma 3	GV	(135° / 3)	1.84	Enhanced Lee 3	GV	(45° / 1)	1.98
Gamma 3	GSD	(135° / 3)	1.53	Local Sigma 3	GC	(45° / 1)	1.99
Gamma 3	GC	(135° / 3)	1.90	Gamma 3	GV	(45° / 1)	1.99
<b>Maize versus Grass</b>							
Enhanced Lee	GM	(45° / 2)	1.79	Gamma 3	Ent	(45° / 1)	0.78
Enhanced Lee	GV	(45° / 2)	1.65				
<b>Maize versus Rape</b>							
Forest 5	GM	(45° / 1)	1.29	Enhanced Lee 3	Ang	(45° / 1)	1.69
Forest 5	GV	(45° / 1)	1.53	TSX_σ°_ Mean	Enr	(45° / 1)	1.37
				Local Sigma 3	Ent	(45° / 1)	1.22
<b>Maize versus Orchard</b>							
Forest 5	GM	(45° / 1)	1.29	Local Sigma 3	Ang	(45° / 1)	1.07
Forest 5	GV	(45° / 1)	1.53				
<b>Grass versus Rape</b>							
TSX_σ°	GM	(45° / 1)	1.92	Local Sigma 3	Ang	(45° / 1)	1.86
TSX_σ°	GV	(45° / 1)	1.88	TSX_σ°	H	(90° / 3)	1.36
				Local Sigma 3	Enr	(0° / 1)	1.62
<b>Grass versus Orchard</b>							
TSX_σ°	GM	(45° / 1)	1.48	TSX_σ°	Ang	(90° / 1-5)	1.35
Enhanced Lee	GC	(135° / 1)	1.63	TSX_σ°	Ent	(90° / 1-5)	1.30
<b>Rape versus Orchard</b>							
Gamma 3	GM	(45° / 1)	0.56	TSX_σ°	H	(90° / 1-5)	1.51
Gamma 3	GV	(45° / 1)	0.60	TSX_σ°	Ang	(90° / 1-5)	1.88
				Local Sigma 3	Enr	(45° / 1)	1.71
				Local Sigma 3	Ent	(45° / 1)	1.37

Table C.4. Separability values for the PALSAR image from 31/05/2010.

Class-pair	Texture feature (Direction / Distance)		Separability
<b>Cereals versus Maize</b>			
Alos_σ°_B1	ASM	(90° / 1,2 ,3)	1.51
Alos_σ°_B1	Energy	(90° / 1, 2,3)	1.17
Local region 3_B2	ASM	(45° / 1)	1.36
<b>Cereals versus Grass</b>			
-	-	-	-
-	-	-	-
<b>Cereals versus Rape</b>			
Alos_σ°_B2	GM	(45° / 1)	1.40
<b>Cereals versus Orchard</b>			
Alos_σ°_B2	GM	(45° / 1 ,2)	1.65
Alos_σ°_B2	GV	(45° / 1 ,2)	1.47
<b>Maize versus Grass</b>			
Alos_σ°_B2	ASM	(45° / 1,2)	1.34
Local region 3_B2	ASM	(45° / 1)	1.21
<b>Maize versus Rape</b>			
Alos_σ°_B2	GM	(45° / 1,2)	1.94
Local region 3_B2	GC	(90° / 1,2,3,4)	1.96
Local region 3_B2	GM	(90° / 1,2,3,4)	1.94
Alos_σ°_B2	GC	(45° / 1,2)	1.94
Alos_σ°_B1	GC	(90° / 1,2,3)	1.83
Alos_σ°_B1	ASM	(90° / 1,2,3)	1.61
<b>Maize versus Orchard</b>			
Alos_σ°_B2	GM	(45° / 1,2)	1.96
Alos_σ°_B2	GC	( 45° / 1,2)	1.92
Local region 3_B2	GM	(90° / 1,2,3,4)	1.96
Local region 3_B2	GC	(90° / 1,2,3,4)	1.93
Alos_σ°_B1	GC	(90° / 1,2,3)	1.73
Alos_σ°_B1	ASM	(90° / 1,2,3)	1.69
<b>Grass versus Rape</b>			
Alos_σ°_B1	GC	(90° / 1,2,3)	1.54
Alos_σ°_B1	GM	(90° / 1,2,3)	1.45
Alos_σ°_mean3_B1	GM	(45° / 1)	1.4
Alos_σ°_B1	GM	(90° / 1)	1.39
<b>Grass versus Orchard</b>			
Alos_σ°_B1	ASM	(45° / 1)	1.40
Alos_σ°_B1	ASM	(90° / 1,2,3)	1.41
Alos_σ°_B1	GM	(90° / 1,2,3)	1.34
Alos_σ°_B1	GC	(90° / 1,2,3)	1.34
<b>Rape versus Orchard</b>			
-	-	-	-

## Appendix D

Table D.1. Coefficient of determination  $R^2$  values between measured soil moisture and calculated backscatter coefficient using DTM and GIM (31/05/2010) (land cover: maize; used images: filter of sigma-naught).

Filter	Kernel size	GIM		DTM	
		Entire Pixel	Mean 3x3	Entire Pixel	Mean 3x3
Frost	3x3	0.232	0.367	0.251	0.390
	5x5	0.401	0.488	0.411	0.499
	7x7	0.590	<b>0.643</b>	0.579	<b>0.635</b>
Lee	3x3	0.266	0.43	0.289	0.461
	5x5	<b>0.659</b>	<b>0.701</b>	<b>0.677</b>	<b>0.700</b>
	7x7	<b>0.721</b>	<b>0.627</b>	<b>0.667</b>	<b>0.572</b>
Local Region	3x3	0.153	0.387	0.179	0.423
	5x5	<b>0.700</b>	<b>0.665</b>	<b>0.661</b>	<b>0.690</b>
	7x7	0.545	0.235	0.541	0.266
Mean	3x3	0.269	0.437	0.293	0.469
	5x5	<b>0.690</b>	<b>0.727</b>	<b>0.704</b>	<b>0.720</b>
	7x7	0.636	0.546	0.578	0.494
Median	3x3	0.289	0.423	0.289	0.463
	5x5	<b>0.935</b>	<b>0.873</b>	<b>0.935</b>	<b>0.836</b>
	7x7	0.465	<b>0.641</b>	0.466	0.564
Lee Sigma	3x3	0.192	0.367	0.212	0.396
	5x5	0.192	0.367	0.212	0.396
	7x7	0.192	0.367	0.212	0.396
Gamma	3x3	0.437	0.269	0.293	0.469
	5x5	<b>0.727</b>	<b>0.690</b>	<b>0.704</b>	<b>0.720</b>
	7x7	0.437	0.269	0.578	0.494
Enhanced Frost	3x3	0.437	0.269	0.293	0.469
	5x5	<b>0.727</b>	<b>0.690</b>	<b>0.704</b>	<b>0.720</b>
	7x7	0.546	<b>0.636</b>	0.578	0.494
Enhanced Lee	3x3	0.437	0.269	0.293	0.469
	5x5	<b>0.727</b>	<b>0.690</b>	<b>0.704</b>	<b>0.720</b>
	7x7	0.546	<b>0.636</b>	0.578	0.494
Local Sigma	3x3	0.270	0.104	0.117	0.288
	5x5	0.332	0.177	0.195	0.354
	7x7	0.340	0.124	0.142	0.370
Gamma Map	3x3	0.199	0.381	0.220	0.394
	5x5	0.223	0.392	0.236	0.392
	7x7	0.290	0.366	0.291	0.352

Table D.2. SNR and ENL of TerraSAR-X imagery of 31/05/10.

Filter	Kernel size	$\sigma^\circ$ then Filtering		Filtering then $\sigma^\circ$		Filtered TSX	
		SNR	ENL	SNR	ENL	SNR	ENL
Frost	3x3	23.19	44.43	23.83	41.29	23.83	26.77
	5x5	19.59	67.06	20.54	55.23	19.72	36.73
	7x7	17.78	98.61	18.57	75.26	17.57	50.89
Lee	3x3	21.65	51.21	21.53	50.27	21.04	32.16
	5x5	17.40	93.83	17.28	90.05	16.08	58.96
	7x7	15.91	150.64	15.78	141.91	14.49	94.78
Local Region	3x3	18.80	33.24	18.87	33.78	17.51	20.75
	5x5	15.51	47.38	15.61	49.31	13.72	29.98
	7x7	14.38	68.40	14.51	72.98	12.48	44.97
Mean	3x3	21.50	51.90	21.30	51.11	20.78	32.67
	5x5	17.12	96.63	16.90	93.58	15.67	61.23
	7x7	15.60	155.27	15.36	148.15	14.03	98.77
Median	3x3	21.77	45.33	21.77	46.86	20.71	29.37
	5x5	17.19	82.39	17.20	87.47	15.53	54.91
	7x7	15.58	129.30	15.56	142.69	13.79	90.27
Lee Sigma	3x3	23.90	42.35	21.48	50.12	20.89	32.32
	5x5	23.90	42.35	17.66	84.94	16.10	56.70
	7x7	23.90	42.35	16.36	127.80	14.58	87.61
Gamma	3x3	21.50	51.90	21.30	51.11	20.78	32.67
	5x5	17.12	96.63	16.90	93.58	15.67	61.23
	7x7	15.60	155.27	15.36	148.15	14.03	98.77
Enhanced frost	3x3	21.50	51.90	21.38	51.00	20.74	32.43
	5x5	17.12	96.63	16.96	93.27	15.63	60.72
	7x7	15.60	155.27	15.42	147.76	13.99	97.93
Enhanced Lee	3x3	21.50	51.90	21.30	51.11	20.78	32.67
	5x5	17.12	96.63	16.90	93.58	15.67	61.23
	7x7	15.60	155.27	15.36	148.16	14.03	98.77
Local Sigma	3x3	27.12	30.40	26.96	30.85	29.36	19.04
	5x5	25.68	36.90	25.20	37.54	26.88	22.96
	7x7	25.00	41.13	24.31	42.08	25.74	25.44
Gamma Map	3x3	-	-	21.87	50.20	21.11	31.45
	5x5	-	-	17.39	91.13	16.01	58.50
	7x7	-	-	15.83	144.67	14.36	94.79

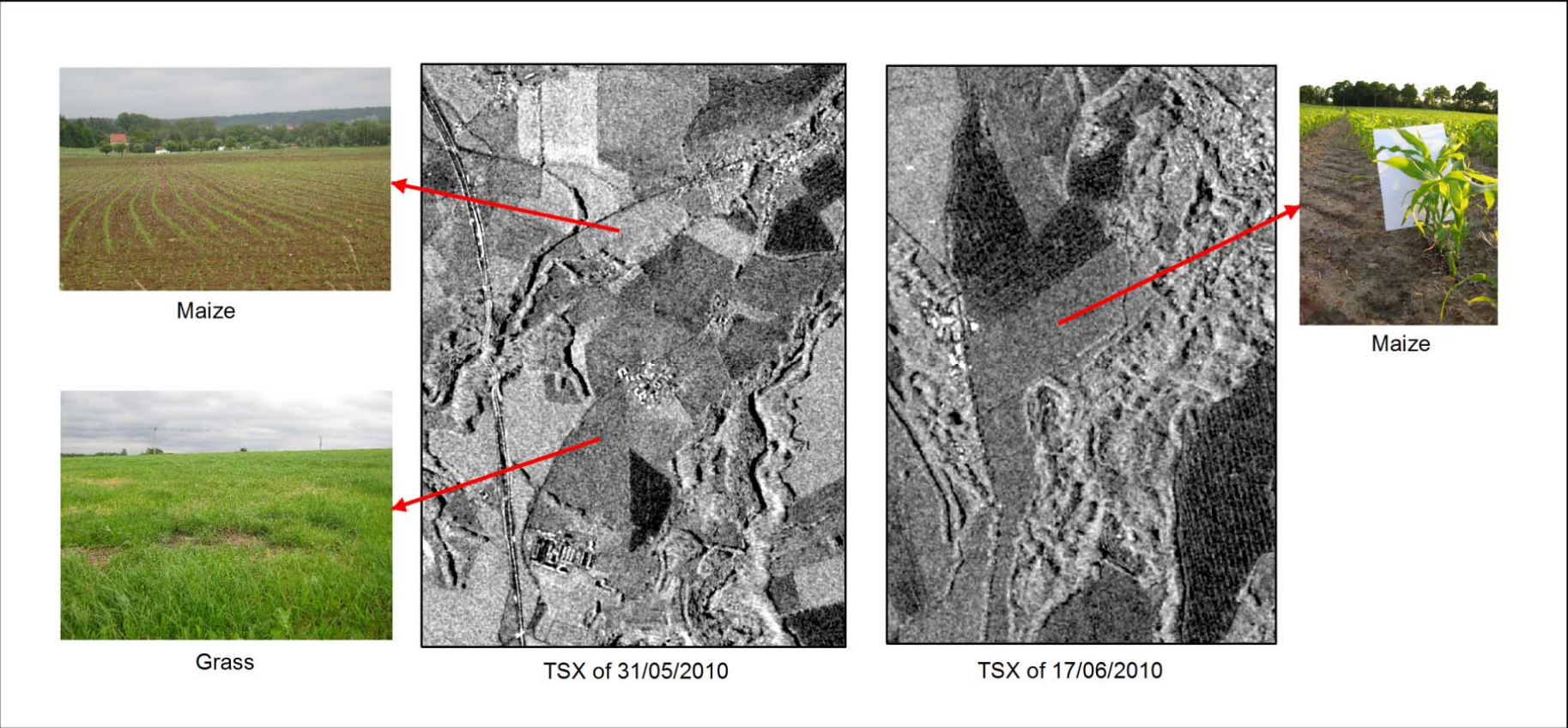
Table D.3. Coefficient of determination  $R^2$  values between measured soil moisture and calculated backscatter coefficient for TSX (17/06/2010) for early growing maize.

Filter	Kernel Size	TSX 17/06/2010	
		$\sigma^\circ$ then Filtering	Convolution 3x3
Lee Sigma	3	0.518	0.700
	5	0.518	0.700
	7	0.518	0.700
Median	3	0.593	0.768
	5	0.879	0.885
	7	0.686	0.827
Frost	3	0.494	0.657
	5	0.554	0.740
	7	0.742	0.842
Local Region	3	0.616	0.823
	5	0.699	0.873
	7	0.803	0.734
Gamma Map	3	0.232	0.415
	5	0.423	0.880
	7	0.343	0.381
Lee	3	0.587	0.749
	5	0.858	0.881
	7	0.870	0.878
Mean	3	0.597	0.758
	5	0.875	0.886
	7	0.830	0.857
TSX		0.372	0.597

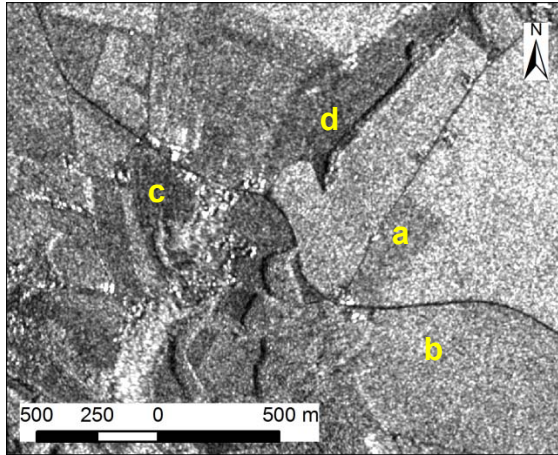
Table D.4. SNR and ENL of TerraSAR-X imagery on 17/06/10.

Filter	Kernel size	$\sigma^\circ$ then Filtering		Filtering then $\sigma^\circ$	
		SNR	ENL	SNR	ENL
Frost	3x3	22.49	27.82	23.98	25.56
	5x5	19.05	38.43	20.80	32.16
	7x7	17.15	53.35	18.66	42.07
Lee	3x3	19.86	34.85	19.76	34.46
	5x5	15.95	61.74	15.76	60.45
	7x7	14.57	94.94	14.40	92.00
Local Region	3x3	17.16	23.12	17.39	23.33
	5x5	13.99	33.83	14.17	34.72
	7x7	13.00	49.66	13.18	50.68
Mean	3x3	19.58	35.55	19.31	35.68
	5x5	15.55	64.10	15.21	64.43
	7x7	14.17	98.59	13.81	98.84
Median	3x3	19.83	31.70	19.89	32.22
	5x5	15.50	57.52	15.51	59.87
	7x7	14.04	88.46	14.04	93.36
Lee Sigma	3x3	22.15	29.05	20.29	32.05
	5x5	22.15	29.05	16.91	50.29
	7x7	22.15	29.05	15.77	69.53
Gamma	3x3	19.58	35.55	19.31	35.68
	5x5	15.55	64.10	15.21	64.43
	7x7	14.17	98.59	13.81	98.84
Enhanced Frost	3x3	19.58	35.55	19.41	35.52
	5x5	15.55	64.10	15.27	64.17
	7x7	14.17	98.59	13.86	98.46
Enhanced Lee	3x3	19.58	35.55	19.34	35.53
	5x5	15.55	64.10	15.22	64.25
	7x7	14.17	98.59	13.81	98.73
Local Sigma	3x3	26.09	20.68	25.72	20.99
	5x5	24.64	24.79	23.83	25.74
	7x7	23.97	27.26	22.86	28.82
Gamma Map	3x3	-	-	19.87	34.70
	5x5	-	-	15.66	62.48
	7x7	-	-	14.19	97.20

Appendix E-1



Appendix E-2



TSX (HH) on 18/04/2011



a) Bare soil



c) Cereal



b) Early growing maize



d) Grass

